Advanced non-precious metal catalyst for oxygen reduction reaction in polymer electrolyte membrane fuel cells

by

Gaopeng Jiang

A thesis

presented to the University of Waterloo

in fulfillment of the

thesis requirement for the degree of

Doctor of Philosophy

in

Chemical Engineering (Nanotechnology)

Waterloo, Ontario, Canada, 2017

Examining Committee Membership

The following served on the Examining Committee for this thesis. The decision of the Examining Committee is by majority vote.

External Examiner	Dr. Viola I. Birss Professor @ University of Calgary
Supervisor(s)	Dr. Zhongwei Chen Associate Professor
Internal Member	Dr. Michael Fowler Professor
Internal Member	Dr. Eric Croiset Professor
Internal-external Member	Dr. Xianguo Li Professor, PEng

Author's Declaration

This thesis consists of material all of which I authored or co-authored: see Statement of Contribution included in the thesis. This is a true copy of the thesis, including any required final revisions, as accepted by my examiners.

I understand that my thesis may be made electronically available to the public.

Statement of Contributions

The body of this thesis is based on a combination of work drafted for submission. Various sections are adapted from the following list.

Chapter 3

G. Jiang, J. Choi, J. Li, X. Fu, P. Zamani, P. Xu, J. Li, G. Lui. D. Banham, S. Ye, Z. Chen[a]*. Boosted Performance of Novel N, S-co-doped non-precious metal Catalyst Towards Oxygen Reduction via Comprehensive Effects of Sulfur on Active Sites. *Journal of Materials Chemistry A.*2017

Prof. Chen and Dr. Ye directed the research. Prof. Chen. and I designed the research and I designed all experiments. Mr. Xu, Miss Jenny Li and I accomplished the catalyst synthesis. Dr. Fu, Mr. Zamani and I conducted all physical characterizations. Dr. Fu, Mr. Xu and I conducted half-cell electrochemical testing and Dr. Choi, Dr. Banham and I conducted MEA fabrication and PEMFC testing. Dr. Jingde Li conducted all DFT calculations. Dr. Choi and I wrote the paper. All authors participated in the analysis of the experimental data and discussions of the results.

Chapter 4

G. Jiang, J. Zhang, H. Zarrin, T. Cumberland, J.H. Ahn, D. Higgins, M. Li, M.A. Hoque, P. Zamani, K. Feng, Z. Chen. Porous Nitrogen-rich Polymer Film Derived Free-standing Metal-free Air Electrode for Oxygen Reduction Reaction. (2017)

Prof. Chen directed the research. Prof. Chen and I designed the research. Dr. Zarrin and I designed all experiments. Dr. Zarrin and I accomplished the polymer synthesis.

Mr. Cumberland, Mr. Ahn and I conducted the porous membrane casting. Mr. Ahn and I completed the free-standing catalyst film synthesis. Dr. Higgins, Mr. Ahn, Mr. Zamani and I conducted the electrochemical tests and associated optimization. Dr. Houque, Mr. Li, Mr. Feng and I conducted all the physicochemical characterizations. Ms. Zhang and I assembled electrodes and completed full cell tests. I wrote the paper and All authors participated in the analysis of the experimental data and discussions of the results.

Chapter 5

G. Jiang,[†] X. Wu,[†] M. Chen, A. Yu, R.M. Berry, Z. Chen, K.C. Tam Mesoporous Nitrogen-doped Carbon Nanorods Derived from Biomass as Metal-free Carbocatalysts,. 2017

X. Wu,[†] G. Jiang,[†] M. Chen, Q. Yao, A. Yu, J.Y. Lee, R.M. Berry, K.C. Tam, Polydopamine-modified N-enriched mesoporous carbon derived from biomass for supporting highly dispersed metal nanocatalysts, *Applied Catalysis B: Environmental*, APCATB-D-17-00970

Dr. Wu and I contribute equally to these two papers. Dr. Wu and I designed the experiment together and we shared the work of catalyst synthesis, characterizations and electrochemical evaluations. Ms. Chen, Mr. Yao and Mr. Lee also helped conduct some physicochemical characterizations. Mr. Berry provided CNC and collected related experimental data. Dr. Wu and I wrote the drafts and all authors reviewed the manuscript

Abstract

To address the global energy and environmental challenges, the polymer electrolyte membrane fuel cell (PEMFC) is proposed and developed as one of the most promising power source candidates for various applications including electric vehicles, stationary power stations and portable devices due to its high efficiency and low emissions. However, the intrinsically sluggish reaction at the cathode, namely the oxygen reduction reaction (ORR), hinders the large-scale commercialization of the PEMFC as expensive and scarce platinum-based catalysts are used to accelerate this reaction. In order to reduce the cost of PEMFC, non-precious metal catalyst (NPMC) towards ORR has been developed and already brought itself from a pure scientific curiosity to a practically viable option for some commercial applications.

In this work, two classes of low-cost NPMCs are investigated. One class is composed of high temperature treated transition metal-nitrogen-carbon M-N-C (M=Fe, Co) complex catalyst, especially iron-nitrogen-carbon complex (Fe-N-C) catalyst. These materials can demonstrate decent ORR activity and durability and provide high power output at moderate operating voltages. The other class with an even lower cost is the metal-free catalyst, which omits the metal content from M-N-C catalysts completely. This type of catalyst demonstrates excellent durability, especially in the presence of species that can cause contamination (e.g. carbon monoxide) or species that can cross-over (e.g. methanol). These two classes of NPMCs are developed and delivered with the ultimate objective of achieving a significant cost reduction in PEMFC while maintaining excellent PEMFC performance and durability.

Herein, the research in this thesis starts with novel N, S-co-doped Fe-N-C catalysts to meet the objective of obtaining a highly economical and efficient NPMC. The catalyst is fabricated via pyrolyzing the composite of *in-situ* polymerized novel N, S-co-containing precursor, polyrhodanine (PRh) onto the acid-treated carbon black via the initiation of $FeCl_3$. The N, S-co-doped Fe-N-C catalyst is obtained after two heat-treatment steps with one acid-leaching step in between. The catalyst demonstrates excellent ORR activity, bearing a half-wave potential of 0.77 V vs RHE in the acidic electrolyte. It also shows an excellent H_2-air PEMFC performance, ranking the obtained peak power density (386 mW cm^{-2} at 0.46 V) among the best reported NMPC catalyst in H_2-air PEMFC in the world. The N, S-co-doped Fe-N-C catalyst tends to catalyze the oxygen reduction via four electron pathway according to its number of transferred electrons (>3.94) and low peroxide yield (< 2.8 %). In addition, it demonstrates decent durability, showing only 32 mV downshift after 5000 potential sweep cycles in the ADT tests.

The role of sulfur in this N, S-co-doped Fe-N-C is examined with the assistance of different characterizations and the comparison with an S-free nitrogen precursor (polypyrrole, PPy). Sulfur can benefit the ORR activity and durability of FePRh-HT2 catalyst with regard to the morphology, active sites density as well as the molecular structure of active sites. In the presence of sulfur, FeS nanoparticles are formed during pyrolysis and they function as the macropore and mesopore agents to enhance the BET surface area as well as the mass diffusion after acid leaching. The formation of FeS during the pyrolysis inhibits the formation of Fe_3C and facilitates the formation of the Fe-Nx active sites, resulting in higher active sites density of FePRh-HT2 as opposed to FePPy-HT2. The sulfur-doped Fe-N_4 active site structure demonstrates a better affinity to O_2 molecule comparing to

Fe-N_4 active site structure in the DFT calculation, corroborating the better ORR stability of the FePRh-HT2 catalyst. Therefore, the multi-functionality of sulfur from the precursor PRh endows this N, S-co-doped NPMC with high ORR activity and durability

This research also presents the feasibility of highly porous free-standing low-cost metal-free catalysts that are successfully prepared via the solution casting methodology followed by annealing the porous PBI-Py membrane at high temperature. The obtained catalyst film is truly metal-free and has adjustable 3D nano-network structure. The surface area of final catalyst can reach as high as 902 m^2 g^{-1} by tuning the amount of pore agent in the casting solution, The optimal catalyst in this series is 95%PBI-Py-1000 which demonstrates comparable activity ($E_{1/2}$ = 0.82 V vs. RHE) to commercial Pt/C catalyst in alkaline electrolyte and superior methanol tolerance to that of commercial Pt/C catalyst in RDE tests. The results suggest not only PBI-Py to be a decent nitrogen precursor for metal-free catalysts, but also the solution casting methodology as a feasible methodology for NPMC fabrication.

To further reduce the cost of ORR catalysts and introduce another level of environmental-benignity, biomass precursor, cellulose nanocrystals (CNC) are applied to develop N-doped mesoporous carbon nanorods as the metal-free catalysts. With a smooth coating of MF on the surface of CNC, the MFCNC derived fibrous-structure of mesoporous nitrogen-doped carbon nanorods, N-CNR were obtained via one-step pyrolysis. The decent catalytic activity towards ORR in the alkaline electrolyte shapes N-CNR as the excellent metal-free catalysts with ultralow cost.

In summary, this thesis focuses on the development of NPMC, including M-N-C catalysts and metal-free catalysts, with high activity and durability towards ORR as well as

achieving a cost reduction for the catalyst. Several recommendations for future work based on this work are also included at the end, offering what we believe are meaningful future research directions for the development of NPMC for ORR.

Acknowledgements

First of all, I would like to express the greatest appreciation to my supervisor, Professor Zhongwei Chen to offer me a great opportunity to pursue my doctoral degree at the prestigious University of Waterloo. His mentorship and guidance lead me into the academic world and enlighten me to start and continue my own academic life.

Here I also would like to thank my colleagues at Applied Nanomaterials and Clean Energy Laboratory (ANCEL), especially those who have worked on fuel cell catalysts and alcohol fuel cell sensors with me. The knowledge and ideas we shared and exchanged at the healthy and encouraging atmosphere give me hints to tackle challenges from the projects.

I would like to show my appreciation to my Ph.D. examining committee, including Professor Xianguo Li, Professor Eric Croiset, Professor Michael Fowler and Professor Viola Birss for their time and contributions as well as Professor Ali Elkamel for his participation in my comprehensive proposal examining committee.

I would also like to thank those outstanding researchers from our industrial collaborators, including Ms. Shanna Knights, Dr. Siyu Ye, Dr. Dustin Banham from Ballard Power Systems Inc. and Mr. Felix JE Comeau, Dr. Maciej Goledzinowski and Dr. Qun Zhou from Alcohol Countermeasure Systems Corp..

I also like to acknowledge the support from Natural Science and Engineering Research Council of Canada (NSERC), the Waterloo Institute for Nanotechnology (WIN), CaRPE-FC network, Ontario Centers of Excellence (OCE) as well as the China Scholarship Council (CSC).

In the end, I'd like to acknowledge the selfless support, understanding and encouragement from my family within these years, especially during the difficult times.

Dedication

Dedicated to my parents

for supporting and encouraging me all the time

with their love and caring

and to my friends

who are beside me when I am at my toughest time.

Table of Contents

List of Figures

List of Tables

List of Abbreviations

ADT	Accelerated Degradation Test
AFC	Alkali Fuel Cells
BET	Brunauer-Emmett-Teller
CCM	Catalyst Coated on Membrane
CL	Catalyst Layer
CNC	Cellulose Nanocrystals
CNT	Carbon Nanotube
CV	Cyclic Voltammetry
DBP	Dibutyl Phthalate
DFT	Density Function Theory
DOE	U.S. Department of Energy
EDX	Energy Dispersive X-Ray Spectroscopy
Fe-N-C	Iron-Nitrogen-Carbon Complex Catalyst
FT-IR	Fourier Transform Infrared
GCE	Glass Carbon Electrode
GDL	Gas Diffusion Layer
HAADF-STEM	High Angle Annular Dark Field Scanning Transmission Electron Microscopy
HOR	Hydrogen Oxidation Reaction
ICP-OES	Inductively Coupled Plasma Optical Emission Spectrometry
LSCV	Linear Staircase Voltammetry

LSV	Linear Sweep Voltammetry
LTFC	Low-Temperature Fuel Cells
MA	Mass Activity
MCFC	Molten Carbonate Fuel Cells
MEA	Membrane Electrode Assembly
MeN_x	Coordinate of Transition Metal Ions and Nitrogen
MF	Melamine Formaldehyde
M-N-C	Transition Metal-Nitrogen-Carbon Complex Catalyst
MOF	Metal Organic Framework
MSD	Mass-Based Active Sites Density
N-CNR	N-Doped Carbon Nanorod
NMR	Nuclear Magnetic Resonance
NPMC	Non-Precious Metal Catalysts
OCV	Open Circuit Voltage
ORR	Oxygen Reduction Reaction
PAFC	Phosphoric Acid Fuel Cell
PBI-Py	Poly ([5,5'-Bi-1H-Benzimidazole]-2,2'-Diyl-2,6-Pyridinediyl)
PEM	Polymer Electrolyte Membrane
PEMFC	Polymer Electrolyte Membrane Fuel Cell
PPy	Polypyrrole
PRh	Polyrhodanine
RDE	Rotating Disk Electrode

RHE	Reversible Hydrogen Electrode
RRDE	Rotating Ring Disk Electrode
SCE	Saturated Calomel Electrode
SEM	Scanning Electron Microscopy
SHE	Standard Hydrogen Electrode
SOFC	Solid Oxide Fuel Cells
TEM	Transmission Electron Microscopy
TOF	Turn-Over Frequency
XPS	X-Ray Photoelectron Spectroscopy
XRD	X-Ray Diffraction

Chapter 1: Introduction

1.1 The Challenges

In the 21st century, the energy crisis has been concerned as one of the most critical and urgent issues that the whole human societies have to face and address. Global energy demands continually soar to new highs, with average growth rates in the consumption of energy soaring by over 50% in a 25 year period (from 1987 to 2012).[1] Fossil fuel resources, the main energy sources, are being consumed at unprecedented rates and generate more than 31 billion tons of greenhouse gases (CO_2) as well as gaseous pollutants such as sulfur dioxide, nitrogen oxides due to the relatively "dirty" combustion process.[2] The related issues including climate change, globel warming, air pollution, resource scarcity and energy security concerns make the whole society realize the necessity and importance of developing alternative sustainable and clean energy technologies.

Electrochemical devices, including fuel cells, batteries and supercapacitors, have been developed to meet the requirements as the clean energy technologies, which operate with only environmentally-benign emissions and boasts excellent operational efficiencies. Some commercial electrochemical devices have been promoted to the general public in transportation applications or utility scale power production, such as electrical vehicles based on fuel cells or lithium-ion batteries technology, telecommunications backup power and materials handling (i.e., forklift) fleets based on fuel cell technology[3]. Specifically, if the fully commercialization of fuel cell electrical vehicles is realized, the most significant

advantage of fuel cell technology, zero emission of greenhouse gas could be capitalized for both the human society and the environment of the earth.[4]

Although the target markets exist and the potential markets will grow larger, practically viable clean energy technologies are still not ready due to remained unaddressed technical challenges, mainly relate to cost and durability. Specifically, polymer electrolyte membrane fuel cells (PEMFCs) is one of the most promising renewable energy technologies due to its high energy conversion efficiency, high power density, and environmental benignity. However, the system costs of existing PEM fuel cells are still very high, mainly due to the required high content of platinum catalysts at both anode and cathode to catalyze the electrochemical reactions, i.e. hydrogen oxidation reaction (HOR) and oxygen reduction reaction (ORR) respectively. The limited nature reserves of precious metal set its price dramatically high. What's worse is that the price would not decrease once the PEMFCs are massively-produced, instead it will increase more owing to its scarcity.[5] In the current technology, the platinum-based electrocatalysts compromise almost 50 % of the total PEMFC stack cost if the mass production reaches 500,000 units per year.[6] Of the two half-reactions occurred in the fuel cell, it is well-known that ORR has inherently six orders of magnitude slower reaction kinetics than that of HOR, which limits the entire PEMFC performance.[7-10] Therefore, the majority of platinum is utilized for the cathode reaction. Additionally, the ORR catalysts at cathode are exposed to harsh (high temperature, high humidity), highly-oxidizing (high oxygen concentration, high potential), corrosive (strong acidity) conditions, which results in physical, chemical and morphological degradation over long periods of operation.[11] The insufficient stability of ORR catalysts severely impedes the

commercialization of PEMFCs. Therefore, the development of low-cost, highly active and stable catalyst towards ORR becomes crucial and essential for PEMFC technology.

Two approaches have been proposed and intensely investigated to develop new ORR catalysts: (i) reducing the usage of platinum via enhancing the utilization of platinum catalysts or alloying platinum with other transition metals; (2) completely replacing platinum-based catalysts with non-precious metal catalysts (NPMC) using transition metals. Although breakthroughs have been reported for first approach in last decade,[12-14] the NPMC approach turns to be a better choice in the long run due to unavoidable issue of limited world supply of platinum. Since the first report of ORR catalytic activity of cobalt phthalocyanine in KOH electrolyte in 1964 by Jasinski,[15] several breakthroughs have boosted the ORR activity of NPMCs significantly hence make NPMCs as a commercially viable option.[16, 17] However, the ORR activity is still much lower than that of commercial platinum catalyst, especially after the breakthroughs from the first approach.[12-14] Therefore, the development of NPMCs with high activity towards ORR still remains the major topic of the field. As to stability and durability, NPMCs demonstrate noticeably poor stability and durability. To date, a real PEMFC performance of a stable NPMC for hundreds of hours is still considered to be a major achievement.[18] Interestingly, a new category of NPMC, metal-free catalyst has been attracted significant attentions in the fuel cell community due to its facile fabrication, low cost and high stability, especially in the presence of carbon monoxide or methanol.[19, 20] However, the relatively low activity in acidic electrolyte and the ambiguity of trace metal contents in the catalyst limits the application of metal-free catalyst.

1.2 Introduction to Fuel Cells

A fuel cell is an electrochemical energy system that directly converts chemical energy between the fuel and oxygen or another oxidizing agent into electricity.[21] High efficiency, quiet operation and zero greenhouse gas emission (if hydrogen is applied) are the main characteristic advantages of fuel cells over traditional internal combustion engines. Moreover, if the hydrogen is gained from renewable or nuclear energy sources, the produced power can be more environmental-friendly as no climate change emissions occur.[22]

Generally, a fuel cell consists of three major components, i.e. the anode, the electrolyte and the cathode in sequence. The anodic and cathodic reactions occur at the interfaces of those three different segments respectively. According to the types of electrolyte employed, fuel cells could be classified as: (i) low temperature fuel cells including Alkali Fuel Cells (AFC), Polymer Electrolyte Membrane fuel cells (PEMFC) and Phosphoric Acid Fuel Cells (PAFC); (ii) high temperature fuel cells including Molten Carbonate Fuel Cells (MCFC) and Solid Oxide Fuel Cells (SOFC). **Table 1-1** summarizes the different categories of fuel cells and their operating conditions.

Table 1-1 Different types of fuel cells based on the type of electrolyte and operating temperature

Temperature range class	Fuel Cell	Electrolyte	Temperature (℃)
Low Temperature (LT)	AFC	Aqueous alkaline solution	≤ 80
	PEMFC	Polymer electrolyte membrane	≤ 80
	PAFC	Phosphoric acid	150 - 200
High Temperature (HT)	MCFC	Molten carbonate salt mix.	600 – 650
	SOFC	O^{2-}-conducting ceramic oxide	850 -1100

The operating temperature plays an important role in selecting the key materials for fuel cell system, such as electrodes, electrolyte, interconnect and bipolar plates. For instance, aqueous electrolytes are only allowed below 200 ℃ due to high water vapor pressure and quick degradation at higher temperatures while SOFC has to operate at the temperature as high as 850^{o}C to ensure enough ionic conductivity of the electrolyte. Additionally, the operating temperature also affects the choices of fuel and oxidants. Pure hydrogen and pure oxygen or clean air are preferred for Low-Temperature Fuel Cells (LTFC) such as PEMFC and AFC as the trace amount of CO in the reformed fuel or polluting gases in the air could deactivate and poison the electrocatalysts. By contrast, reformed hydrogen and even CO are allowed to be fed as the fuel for SOFC due to the inherently fast kinetics, internal reforming and the less dependence on highly-active catalyst at high temperature.[23-25]

Among all the LTFCs, AFCs are first developed and most often used in space and military applications. And another similar clean energy system, using zinc metal as the fuel and concentrated aqueous alkaline solution as electrolyte, is considered as a special AFC, called Zn-air fuel cell or Zn-air battery. PAFCs use phosphoric acid as their electrolyte is commonly used for stationary applications. It is noted that relatively high operation temperature allows certain concentration of carbon monoxide in the fuel, while highly corrosive electrolyte requires high corrosion-tolerance for electrode materials. The rest category, PEMFC uses the polymer electrolyte, including both proton exchange membrane (PEM) and anion exchange membrane (AEM), to conduct either protons or hydroxide ions. Since the ion conduction of in the polymer electrolyte is depended on the dissociation of hydrated ions, PEMFCs have to operate below 100^{o}C. PEMFCs highly attractive among all types of fuel cells due to the high energy density, low operating temperature, quick start-up

time, and rapid response to varying loads as well as a promising candidate for powering of electric vehicles.[23, 26]

1.3 Polymer Electrolyte Membrane Fuel Cell (PEMFC)

In general, as shown in **Figure 1-1**, a PEM fuel cell consists of the key component, a membrane electrode assembly (MEA) and two bipolar plates. An MEA is a full cell combining both anode and cathode aligned together with the solid polymer membrane sandwiched in between. The polymer membrane could conduct either protons or hydroxide ions and insulate electrons. It keeps the anode from the cathode in the MEA, separating the half reactions while allowing ions to travel through electrodes. The anode and cathode normally consist of three layers, catalyst layer (CL), microporous layer (MPL) and the gas diffusion layer (GDL) in sequence. The CL could be coated on either the solid polymer membrane or the GDL. The gas diffusion layer is responsible for providing fuel and oxidant with uniform and direct access to the catalyst layer. Each electrode is in contact with a catalyst layer which in turn is in contact with a GDL.[26]

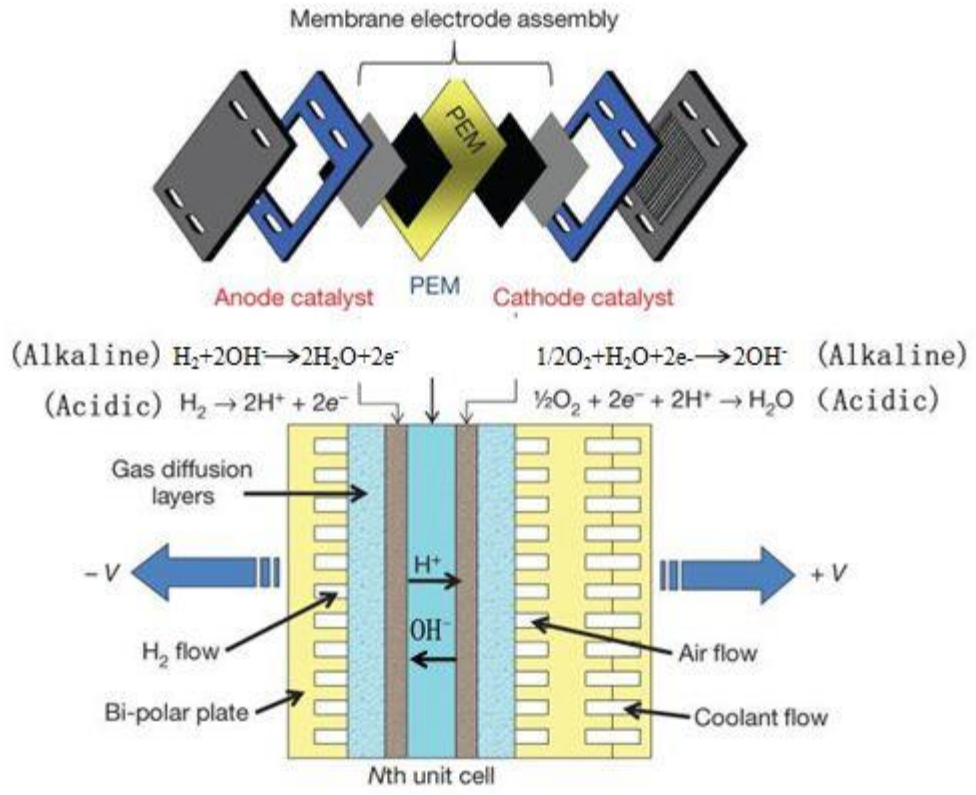

Figure 1- 1 Schematic of an acidic and alkaline PEM fuel cell structures and components, as well as the reactions occurring at both anode and cathode during its operation.[27]

Therefore, when a PEMFC is in operation, the fuel, hydrogen mostly, and oxygen in the air travel through the GDLs to arrive at the interfaces of the CLs on anode and cathode respectively. Then, two hall-cell reactions, namely HOR and ORR strike at the interface of CLs. The former reaction at anode generates electrons, passing through the external circuit, powering a load and then entering the cathode to complete the latter cathodic reaction. The two reactions when combined, results in a general equation where hydrogen and oxygen combine to form water (**Figure 1-1**). The HOR or ORR differs depending on the polymer

electrolyte. When the electrolyte is acidic and proton-conductive, two half reactions and total reaction are as follows.

Acidic

HOR $H_2 \rightarrow 2H^+ + 2e^-$ E^o = 0 V vs SHE (1-1)

ORR $\frac{1}{2}O_2 + 2H^+ + 2e^- \rightarrow H_2O$ E^o = 1.229 V vs SHE (1-2)

Overall $H_2 + \frac{1}{2}O_2 \rightarrow H_2O$ E^o = 1.229 V vs SHE (1-3)

And when the electrolyte is alkaline solution and anion-conducting polymer electrolyte, the three reactions are listed as follows.

Alkaline

HOR $H_2 + 2OH^- \rightarrow 2H_2O + 2e^-$ E^o= -0.828V vs SHE (1-4)

ORR $\frac{1}{2}O_2 + H_2O + 2e^- \rightarrow 2OH^-$ E^o = 0.401 V vs SHE (1-5)

Overall $H_2 + \frac{1}{2}O_2 \rightarrow H_2O$ E^o = 1.229 V vs SHE (1-6)

It is clear that no matter which kinds of polymer electrolyte membranes are used, the total theoretical cell potential still maintains same, equal to 1.229 V. However, there are still several differences. First, the protons migrate from anode to cathode while OH- ions travel from cathode to anode. Second, the final product, water is generated and collected at cathode and anode for PEM and AEM fuel cell respectively. Third, the ORR potential in the acidic electrolyte is much higher than that in the alkaline medium, which has a dramatic influence on the selection of catalyst materials.

In general, a polarization curve could reflect the performance and some characteristic properties of PEMFC. As depicted in a typical polarization curve for PEMFC in **Figure 1-2**,

voltage drops along with the increase of generated current density. Despite a theoretical potential of 1.229 V at both acidic and alkaline condition, the observed open circuit voltages (OCV) are always significantly lower than this value in an actual cell. This is due to fuel crossover to each side, non-standard condition, and platinum catalyst oxidation to some extent.[23]

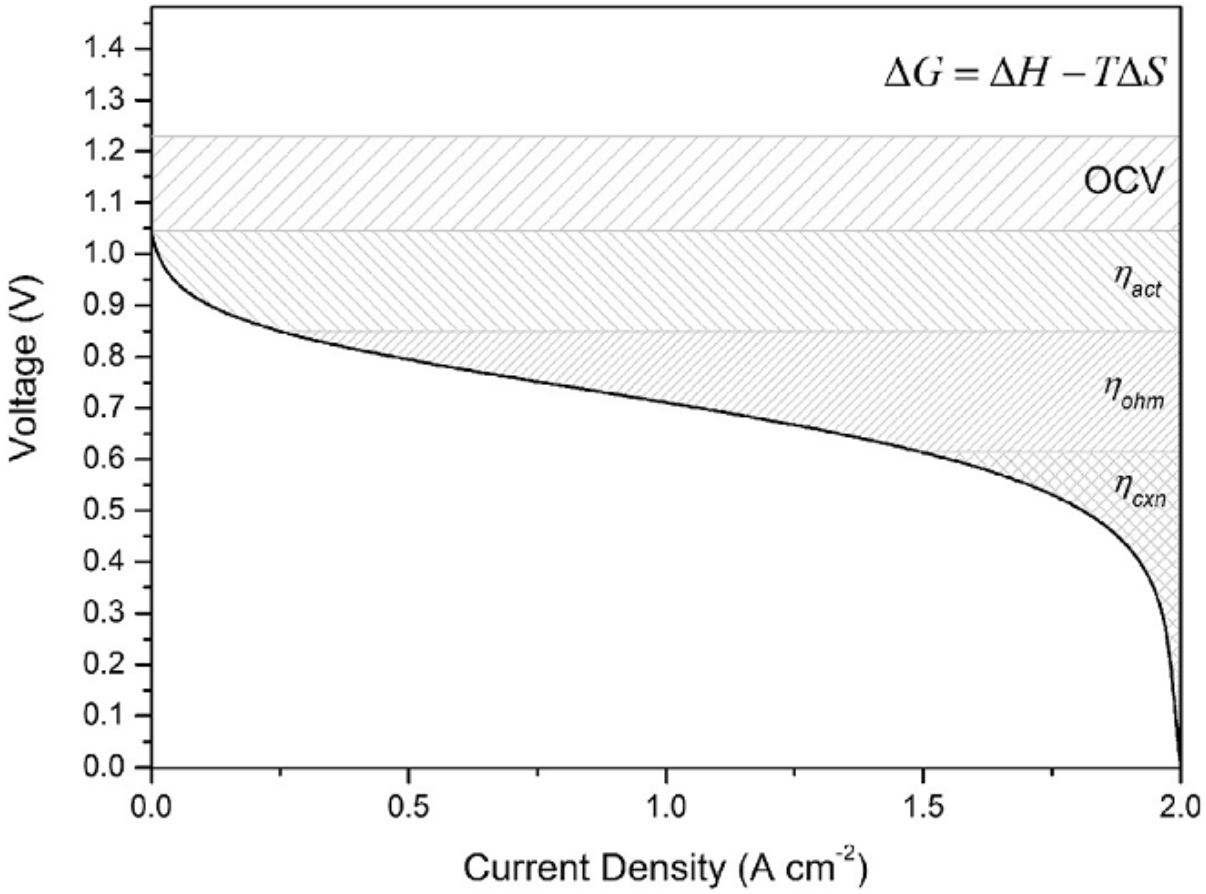

Figure 1- 2 Typical polarization curve for PEMFC[28]

When current is actually generated from the cell, the dramatic voltage drop is observed and it is mainly attributed to the activation of catalysts for both HOR and ORR. Thus, it is called activation overpotential (η_{act}) and this high voltage region is called activation loss region. Overpotential here is mainly contributed by the slow kinetic of ORR at the cathode

while the contribution from HOR is basically negligible. Therefore, it is also a characteristic region for ORR catalysts as the more active the catalyst is, the smaller the activation loss is. In other words, this large overpotential is the major challenge and drive for those scientists and engineers in this field to continue the investigation on ORR catalysts.

The following pseudo-linear region at intermediate current densities in the polarization curve in **Figure 1-2** results from the ohmic losses, where comes from resistances of PEM or AEM electrolyte, connections between different components. The resulted overpotential is called ohmic overpotential (η_{ohm}) and it is highly related to the properties of the polymer electrolyte.

Finally, the region of the dramatic voltage drop at the high current densities in **Figure 1-2** is called mass transfer limited (η_{con}) region, meaning a concentration polarization region. This is due to the phenomenon that the reactants delivered to the catalyst surface could not match up with the consumption rate via the electrocatalytic reactions at electrodes. Thus, mechanically increasing the pressure and the flow rate of gases as well as using pure reactants could be helpful for reducing the concentration polarization. Besides, well-designed nanostructure and morphology of ORR catalysts and advanced catalyst layer architectures conducive could result in decent mass transport and enhance the accessibility of active sites, hence increase obtained current densities as well as the power density in a PEMFC system.

1.4 Non-precious metal catalyst

1.4.1 History and material synthesis

All the NPMC researches begin with Jasinksi's work in 1965, firstly reporting ORR catalytic activity of cobalt phthalocyanine as ORR catalyst in aqueous KOH solution.[29] Then, NPMCs have been intensely investigated and been diversified into several different classes of materials, such as transition metal oxides, nitrides and/or carbides,[30-32] transition metal chalcogenides[33-35], conductive polymers[36, 37], high-temperature treated transitional metal-nitrogen-carbon (M-N-C) composites[16, 17, 38-42] and metal-free catalysts[19, 20]. Among them, M-N-C catalysts are considered as the most promising NPMC in terms of activity and stability.

M-N-C catalysts have evolved greatly from heat-treated metal-nitrogen-coordinated macrocycles[43] and firstly-reported non-macrocyclic precursors by Yeager[44] to highly active and stable M-N-C catalysts derived from novel precursors showing comparable ORR activity to Pt/C catalyst.[16, 17, 38] The great progresses attained on M-N-C catalysts in the last decade show the enhancement of ORR activity and durability of M-N-C catalysts by tuning following factors.

Firstly, metal precursors, could form the coordinate structure of MeN_x together with nitrogen precursors at the edge and/or basal plane of carbon structure during the pyrolysis at high temperature, functioning as the active sites towards ORR in the acidic electrolyte.[17, 45-48] [16] Several transition metals have been studied to construct ORR active catalysts, including Fe [16, 49-55], Co [16, 44, 52-54, 56-59], Ni [52, 56, 59-61] and Mn[62-64]. Among them, Fe and Co based M-N-C catalysts tend to be highly active, especially in the acidic electrolyte. The metal content in

the final catalyst is usually very low and the optimal activity is normally obtained at the metal concentration ranging from 0.2 to 2 wt.%.[10] Moreover, iron and/or cobalt precursors could also play a role of catalyst to enhance the graphitization of carbon precursors,[65-67] improving ORR activity further.

Secondly, nitrogen precursors, not only could combine with metal precursor to form the MeN_x active sites, but also could assist the introduction of MeN_x active sites onto carbon structure.[46] Due to the different chemical properties of various nitrogen precursors under pyrolysis,[17, 38, 47, 68-74] the composition of different doped nitrogen species, the structure and the amount of MeN_x active sites could vary dramatically, leading to various ORR activities in acidic media.[47, 62, 74-76] Besides, the nitrogen doping could alter the electron cloud structure of carbon layers, which could also affect the ORR activity.[77] Intensive researches are reported for different nitrogen precursors, such as ethylenediamine [78-83], acetonitrile [61, 84, 85], and ammonia [86-92]. 1,10-phenanthroline,[17] polyacrylonitrile [44, 52, 84, 93, 94], polyaniline,[16, 62, 95, 96] polypyrrole (PPy),[69] poly(phenylenediamine,[71, 72, 97] ionic liquid,[68] metal-organic framework (MOF)[38, 47, 74] and the combination of different precursors.[38, 47, 74, 98]

Thirdly, carbon support, with high surface area and electron conductivity, could also contribute to ORR activity and durability enhancement.[42, 99] Many types of carbon supports have also been utilized as support material for the fuel cell catalysts including carbon black,[16, 17] graphene,[47, 100] mesoporous carbon,[86, 101-104] carbon nanotube,[20, 105-109] and carbon nanofibres.[51, 110-112] Besides, with the introduction of extra heteroatoms (S, P, B) to the carbon support could further enhance the ORR activity of M-N-C catalyst.[71, 113-116]

Lastly, heat-treatment conditions, including pyrolysis temperature and atmosphere, alter the amount, composition, and type of active sites and affect the morphology of carbon structure in M-N-C catalyst.[17, 74-76]

In general, by tuning those factors and introducing different morphologies, high ORR activity could be achieved. More detailed information is provided in each chapter in the main section.

1.4.2 ORR performance of M-N-C catalyst

Although several important kinds of non-precious metal catalysts for ORR have been reported, the activity of the most catalyst in the acidic medium is not acceptable, except pyrolyzed M–N-C materials, who have demonstrated decent ORR activity and stability close to those of commercially available Pt/C catalysts even in an acidic electrolyte. Therefore, M-N-C catalysts are considered the most promising ORR catalysts. The breakthrough of M-N-C catalyst started at 2009 when Dodelet's group firstly reported highly active Fe-N-C catalyst via ball-milling the pore filling agents (iron acetate and 1,10-phenanthroline) into the slit pores of carbon support following by two-step pyrolysis under Ar and NH_3 respectively.[17] This catalyst generates a volumetric activity of 99 A cm^{-3} at 0.8 V and provides the open circuit voltage as high as 1.03 V in the real H_2-O_2 PEMFC. The concept of using small molecular weight nitrogen precursor and pore-filling agents becomes a promising route for the development of M-N-C catalyst.[117] Later, at Los Alamos National Laboratory, Zelenay's group reported their M-N-C catalysts derived from the composite of *in-situ* polymerized polyaniline on carbon black in the presence of iron and cobalt after sequential steps of the first pyrolysis, acid leaching, and the second pyrolysis.[16] The

obtained M-N-C catalyst not only demonstrates excellent ORR activity, providing a half-wave potential of 0.80 V vs reversible hydrogen electrode (RHE) and peak power density of 0.55 W cm^{-2} at 0.38V in the real H_2-O_2 PEMFC, but also remarkable stability, showing nearly unchanged current density at 0.4 V after 700 hours' test. Then, another promising route of the development of M-N-C catalyst, using high molecular weight polymer especially conductive polymer as the nitrogen precursor is well-established. Later, the combination of this two routes were also reported and demonstrated improved PEMFC performance, reaching to the peak power density of 1.06 W cm^{-2}.[41] With the rising of utilizing MOF, the activity and performance of M-N-C catalyst were further enhanced, reaching to peak power density of 0.90 W cm^{-2} and volumetric activity at 0.8V of 450 A cm^{-3} in H_2-O_2 PEMFC[38] as well as peak power density of 0.38 W cm^{-2} in H_2-air PEMFC.[74]

When the electrolyte is switched to alkaline, M-N-C catalysts demonstrate much higher ORR activity as opposed to that in the acidic electrolyte. For example, in the **Figure 1-3a**, the half-wave potential of the same catalyst tested in the alkaline electrolyte is 141 mV more positive than that obtained in the acidic electrolyte.[118] Furthermore, Fe-N-C catalyst derived from cyanamide and iron acetate (N-Fe-CNT/CNP) outperformed the commercial Pt/C catalyst at a loading of 1.0 mg cm^{-2} in terms of ORR activity in the half-cell test **(Figure 1-3b)**.[95] The reasons behind this ORR behavior lie in following perspectives. First, according to equation 1-2 and 1-5, the standard potential of ORR shifts from 1.229 V vs SHE in acidic medium to 0.401 V vs SHE in alkaline medium. Such potential shift could dramatically affect the local double-layer structure and electric field at the electrode-electrolyte interface, which can significantly decrease the strength of anion adsorption on the surface of the catalyst. Thus, the electrocatalytic processes, including ORR, will be more favorable in the

alkaline medium than that in acidic medium.[119] Specifically for M-N-C catalyst as well as N-doped metal-free catalyst, the protonation of pyridinic nitrogen in both catalysts will be prohibited in alkaline electrolyte, which means the charge density and basicity of adjacent carbon atoms will recover, hence increase their affinity to O_2 and ORR activity.[118]

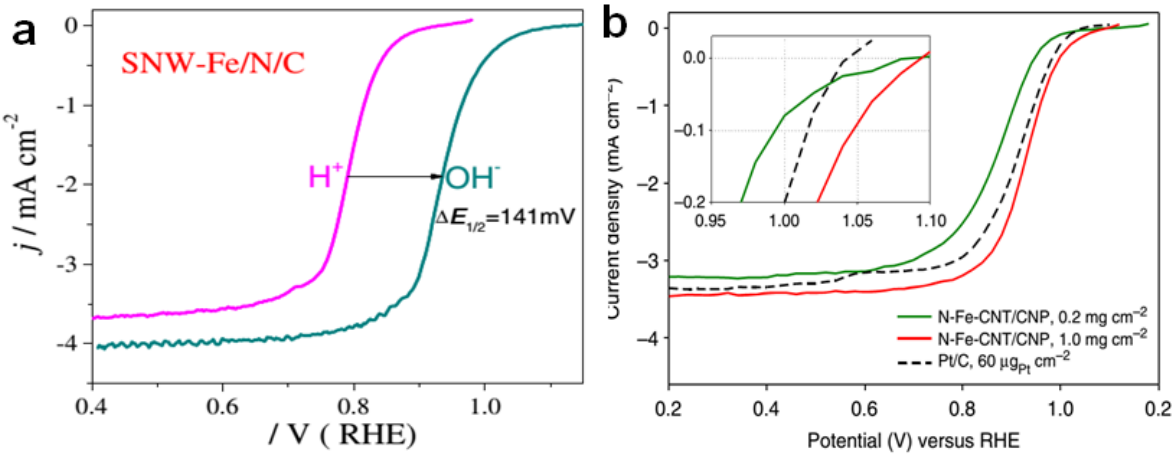

Figure 1- 3 (a) ORR polarization curves of Schiff base networks derived Fe-N-C catalyst (SNW-Fe/N/C) obtained in 0.1M H_2SO_4 and 0.1M NaOH with respect to RHE scale.[118] (b) ORR polarization curves of N-Fe-CNT/CNP at different loadings and commercial Pt/C catalyst obtained in 0.1 M NaOH, inset is zoomed low overpotential region.[95]

1.4.3 Active sites of M-N-C catalyst and associated mechanism

Although the activity and PEMFC performance of M-N-C catalysts have been greatly improved in the last decade, the understanding of the active sites still remains relatively unclear and incomprehensive. In return, this also limits further reasonable design and development of highly-active M-N-C catalysts. The heterogeneous nature, as well as the low density and uneven distribution of active sites challenge the identification and understanding

of the chemical nature of active sites and the quantification of the amount of active site. Recently, with the application of X-ray absorption spectroscopy, Mössbauer spectroscopy, specific gas adsorption analysis, XPS as well as electrochemical probing, different kinds of active sites were proposed and even identified. According to **Figure 1-4**, those reported active sites include metal-nitrogen complex (MeN_x),[47, 120] nitrogen-doped carbon (CN_x) with or without the introduction of transition metal during the synthesis[120, 121] and metallic nanoparticles encapsulated with a few layers of graphitic carbon (MeC_x).[74, 96, 120, 122]

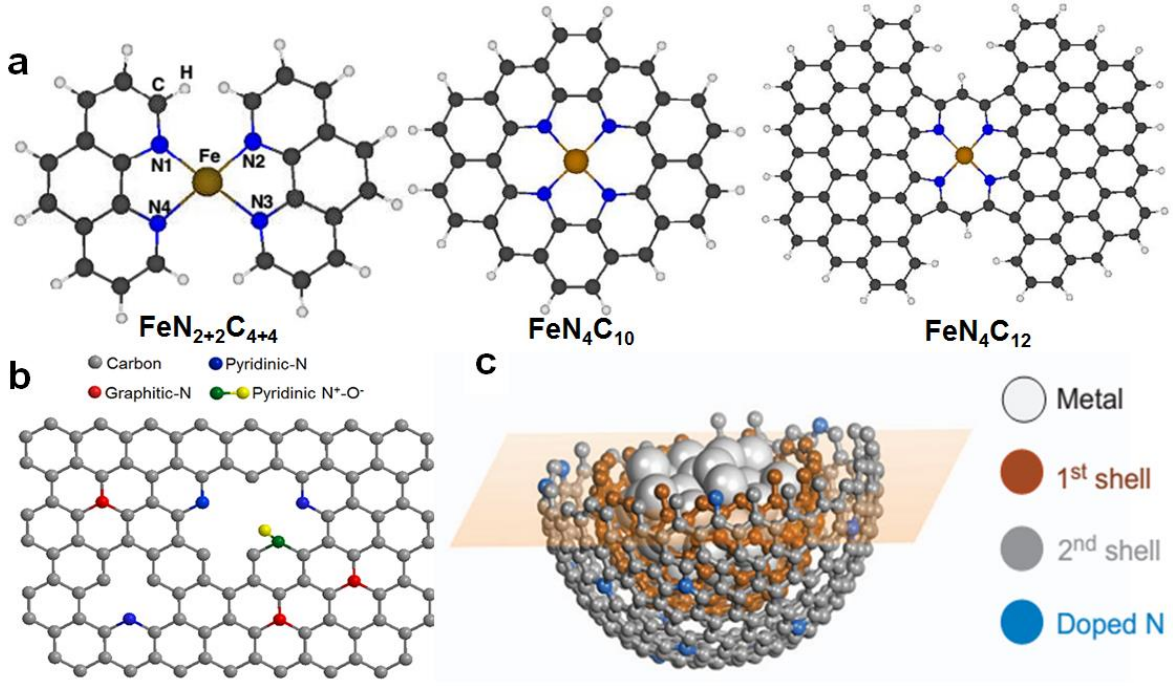

Figure 1- 4 Active sites for M-N-C catalysts. (a) Typical proposed chemical structures of MeN_x active sites;[47] (b) Typical chemical structure of CN_x active sites;[121] (c) Typical proposed structure of MeC_x active sites.[122]

Now that different researchers proposed and claimed different active sites as the catalytically active center for ORR under their own experimental conditions and preset assumptions, the nature of ORR active sites in M-N-C catalyst still remain controversial and

debatable. However, according to Shao's review at 2016[120], the authors, including Jean-Pol Dodelet, summarized reported M-N-C catalysts with different active sites in the literature and ranked them with respect to the initial peak power density (**Figure 1-5**), which provides researchers with insightful opinions of active sites. Firstly, MeN_x active sites exist in most M-N-C catalysts, especially in high performance catalysts (> 0.6 W cm^{-2}). Secondly, pure CN_x sites dominated catalysts fabricated in the absence of metal (dark blue box) do not perform as high as their analogue prepared with metal (light blue box), indicating the necessity of metal for high ORR activity. Thirdly, the encapsulated metal (MeC_x) sites dominated M-N-C catalysts perform the worst among all the catalysts (yellow box). Additionally, the introduction of MOF benefits the performances of MeN_x sites dominated catalysts in PEMFC. As a result, if an M-N-C catalyst contains all the active sites above, MeN_x sites must contribute the most to the total PEMFC performance of the catalyst.

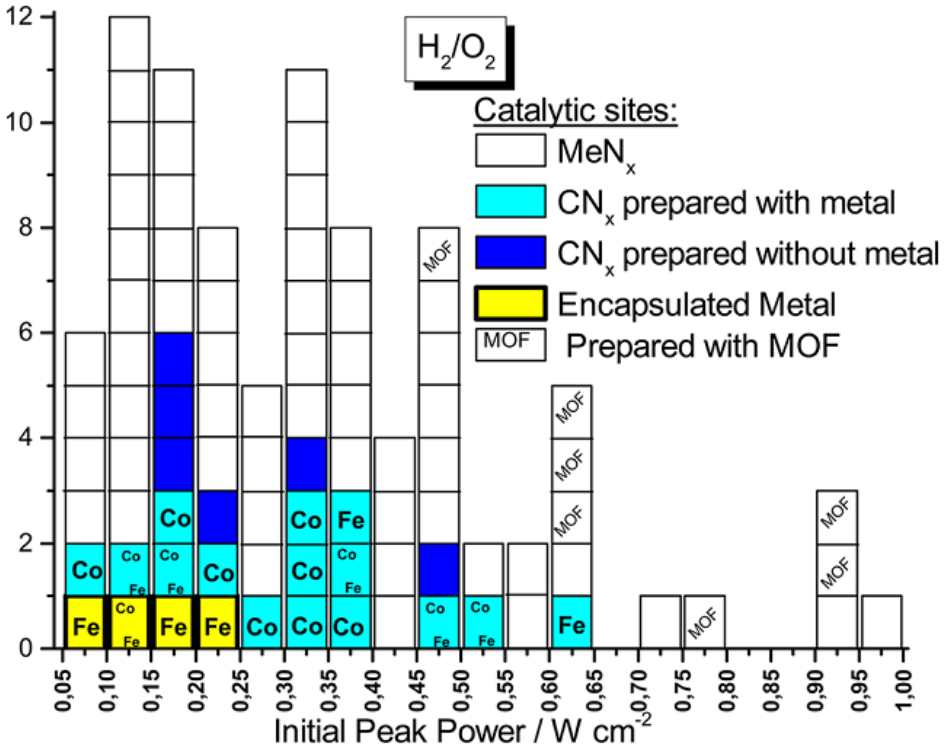

Figure 1- 5 The count of reported M-N-C catalysts as a function of the initial peak power tested in H_2/O_2 PEMFC. The nature of the main active site at work in these catalysts has been proposed by their authors.[120]

Among all the MeN_x sites, such as those in **Figure 1-4a**, the FeN_4 site is not only the most commonly reported one, but also is the first one that was directly visualized via aberration-corrected scanning transmission electron microscopy (AC-TEM).[123] Therefore, the ORR reaction mechanism occurred at an FeN_4 site could be representative for high ORR performance M-N-C catalysts. As shown in the **Figure 1-6**, ORR is a complicated reaction which could lead to multiple products and intermediates under different chemical and electrochemical condition. In the acidic condition of a PEMFC, ORR could undergo either a four electron pathway at the standard redox potential of 1.229 V vs. SHE or a two electron pathway, occurring at a low standard redox potential of 0.70 V vs. SHE (**Equation 1-7**) and generating hydrogen peroxide as the by-product.

Four electron pathway: $O_2+4H^++4e^-\rightarrow 2H_2O$, 1.229 V vs SHE (1-2)

Two electron pathway: $O_2+2H^++2e^-\rightarrow H_2O_2$, 0.70 V vs SHE (1-7)

In the typical reaction pathway, the reaction initiates from the chemical absorption of a gas state oxygen molecule on the FeN_4 site. As suggested by the computational results in the literature,[124] the oxygen molecule absorbed on the iron in the end-on configuration (superoxo form, **Figure 1-6**) instead of the side-on configuration (peroxo form). The adsorption is the coordination process of the oxygen molecule to the FeN_4 site.[125-127] The process includes the charge transfer from the FeN_4 site to O_2 molecules, which would occupy the half-filled π^*-anti-bonding orbitals of O_2 during the hybridization between the

O_2-2p orbitals and Fe-3d orbitals, leading to the elongation of the O–O bond and subsequently the activation of O_2.[124]

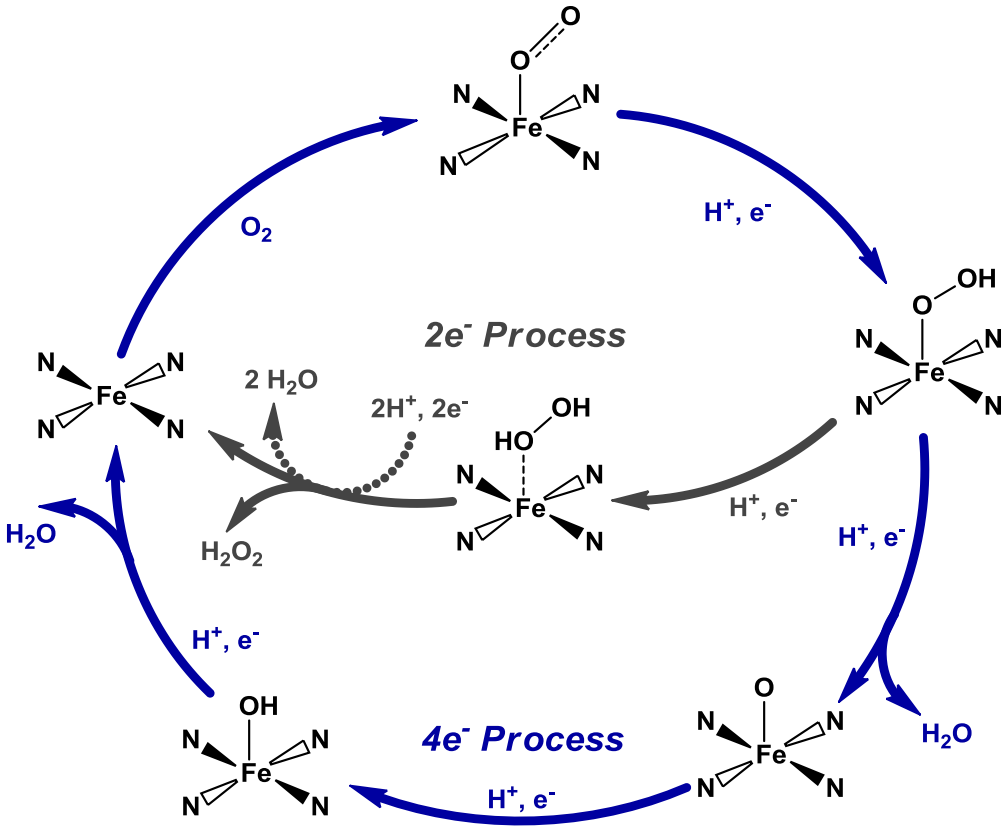

Figure 1- 6 Schematic pathway of ORR on FeN_4 active site.

Then, the activated oxygen molecule is hydrogenated and reduced into –OOH via one proton and an electron. The hydrogen atom bonds at the upper oxygen atom and O-O bond is elongated further. Then, the second proton comes close to –OOH and reacts with either oxygen site, resulting in four-electron pathway via the combination with –OH and the formation of a molecule of water and two-electron pathway via absorbing on the pre-unhydrogenated oxygen and forming a molecule of H_2O_2. For four-electron pathway, the left oxygen bound to iron in the FeN_4 site could further react with one proton and one electron to *in-situ* form –OH group on iron. Finally, the fourth pair of proton and electron reacts with

the –OH group and generates the second water molecule. When the water molecules leave the hydrophobic surface of the catalyst, FeN_4 site remains unchanged.[124] For two-electron pathway, the H_2O_2 molecule will leave the FeN_4 site and either diffues to the bulk or reacts with two pairs of proton and electron and generates two water molecules at another active site, completing "2e + 2e process".[48, 124] Two electron pathway, not only does it works less efficient, but also undesirable peroxide species could cause significant degradation to the polymer membrane electrolyte hence affects the performance and stability of PEMFC.[128-131] Therefore, it is imperative to employ the use of ORR active electrocatalysts towards a four-electron pathway to accelerate the sluggish reaction.

1.5 Metal-free catalyst

1.5.1 History and material synthesis

With the help of the investigation of carbon supported platinum or platinum alloy catalysts, researchers gradually realize the important roles of the carbon support playing. Later, researchers reported the comparable ORR activity of NPMCs to Pt/C, especially transition metal-nitrogen-carbon complex (M-N-C). Carbon supports with either advanced nanostructure (mesoporous sphere, nanotubes, graphene sheets, etc.) or other dopants (nitrogen, sulfur, etc.) were developed to improve the ORR activity and stability of M-N-C catalysts. With the further investigation on the mechanism of ORR and the important role of carbon support working in M-N-C catalysts, researchers realized metal could be leached out at the harsh corrosive environment leading to the decrease of activity and the idea that the carbon support itself with advanced nanostructure and dopants might work as the a group of novel metal-free catalysts was brought up. After Gong et al. firstly reported the superior

ORR activity of vertical aligned nitrogen-doped carbon nanotube (VA-NCNT) to the commercial Pt/C in alkaline condition on science,[20] researches on metal-free catalysts boomed. Hundreds of papers have been published related to metal-free catalysts and it is viewed as the next generation of ORR catalyst in terms of its low costs and high stability.[132] One of the significant advantages for metal-free catalysts in comparison to Pt-based catalysts is their enhanced durability against fuels like CH_3OH and CO, especially in an alkaline medium.[132]

All the metal-free catalysts reported were focused on three directions. Firstly, different nitrogen precursors as well as how to introduce nitrogen into carbon structure were investigated. Phthalocyanine, ammonia, ethylenediamine, melamine et al. could be used to generate N-doped CNT, N-doped graphene or graphite carbon nitride by chemical vapor deposition or the reduction of graphite oxide or oxidized CNT at high temperature.[20, 133-137] Direct pyrolysis of the nitrogen-contained polymer or other organic molecules into the nitrogen-doped carbon material is a common method [138-145] and post NH_3 treatment for porous carbon materials is another easy straightforward method. [86, 138, 139, 146, 147] Secondly, other heteroatoms besides N, such as B, P, O, S, Se, I, doped graphene or CNT were reported as well as the theoretical calculation of its structure by DFT. [148-155] Those heteroatom-doped graphene catalysts demonstrated high ORR activity in alkaline condition and more affinitive to enhancing the production of peroxide instead of OH^- directly.[156] Then, co-doping of different heteroatoms with nitrogen onto the carbon material like was reported, for example N, B co-doping [153, 157, 158], N, S co-doping [159-161], N,O co-doping, [140, 142] N, P co-doping [157], N,O,S tri-doping [141], N,B,P tri-doping [162] et al. The addition of B, O, S, or P to the N-modified nanocarbons often induces notable improvements to the ORR activity, by

either reducing the onset overpotential (although not significantly) or increasing the limiting current (sometimes quite obvious).[156] Lastly, different advanced nanostructures were designed for N-doped carbon to enhance the ORR activity, especially the porous structure. Well-ordered mesoporous carbon derived from hard templates like silica [140, 141] or polystyrene nanobeads [163], porous carbon nanofibre (CNF) [138, 139], nanocage,[158] 3D hierarchically porous structure [164] are the typical porous nanostructure reported to enlarge the surface area and improve the ORR activity in further. Recently, some biomass materials with the natural porous structure such as the pomelo peel [165] and egg shell [166] were applied to be either directly pyrolyzed into N-doped porous carbon in NH_3 or used as templates to prepare the porous carbon. [155, 167] Thus, a nitrogen-doped or heteroatoms co-doped carbon material (bulk carbon, graphene, CNT, or CNF) possessing highly porous nanostructure could be developed and applied as the metal-free ORR catalyst in alkaline electrolyte.

1.5.2 ORR performance of metal-free catalyst

The aforementioned metal-free catalysts are heteroatom-doped carbon nanomaterials in chemical nature. They are reported to be moderately active towards ORR in the acidic electrolyte.[19, 133, 168-170] As shown in the **Figure 1-7a**, a composite of N-doped graphene and N-doped CNT (N-G-CNT) demonstrates an on-set potential close to 0.80 V vs. RHE and a half-wave potential of 0.52 V vs. RHE in the 0.1 M $HClO_4$. When it is mixed with carbon black (KB) in a ratio of 1:4 (w/w), the composite generates a peak power density of 300 W g^{-1} in the H_2-O_2 PEMFC (**Figure 1-7b**). When the electrolyte is switched to 0.1 M KOH, the metal-free catalyst demonstrates excellent ORR activity and even outperforms commercial Pt/C catalyst (**Figure 1-7c**). Additionally, metal-free catalysts are reported to be tolerant to

the poisonous fuel or intermediate molecules such as CO and methanol. For instance, as depicted in **Figure 1-7d**, the responsive current of N-G-CNT keeps nearly unchanged after the addition of CO while that of commercial Pt/C catalyst decreases dramatically.[168]

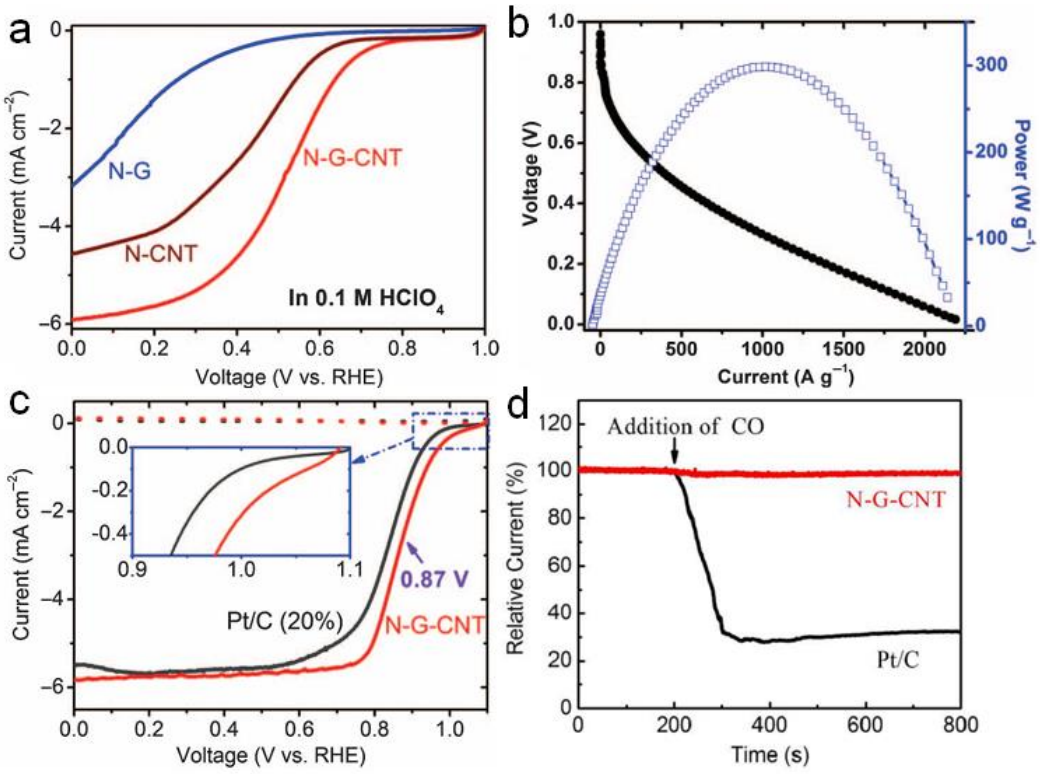

Figure 1- 7 ORR behavior of metal-free catalysts. (a) Polarization curves of N-doped graphene (N-G), N-doped carbon nanotube (N-CNT) and N-doped composite of graphene and carbon nanotube (N-G-CNT) in O_2-saturated 0.1 M $HClO_4$ at a scan rate of 10 mV s^{-1} and a rotation speed of 1600 rpm. (b) Cell polarization and power density as the function of gravimetric current for the N-G-CNT/KB (0.5/2 mg cm^{-2}) with the weight ratio of (N-G-CNT/KB)/Nafion = 1/1; (c) Polarization curves of N-G-CNT) and commercial Pt/C (20%) in O_2-saturated 0.1 M KOH at a scan rate of 10 mV s^{-1} and a rotation speed of 1600 rpm; (d) The relative ORR cathodic current for the N-G-CNT and 20%Pt/C before and after adding CO into the O_2-saturated 0.1 M KOH.[168]

However, in most N-doped carbons materials, it is very challenging to completely remove the transition-metal residuals by acid washing when they are initially introduced at early stages of the preparation. The contribution of trace metal impurities to ORR activity has been investigated.[171-173] As shown in the **Figure 1-8a**, the ORR activity shows a significant dependence on the amount of iron residue in the nitrogen-doped carbon. The ORR activity could be greatly enhanced even with 50 ppm of iron in the catalyst.[173] Thus, the intentional introduction of transition metal should be avoided during the synthesis. As to those commercial carbon sources, such as carbon black, CNT, graphite and reduced graphene oxide (rGO), they contain a significant amount of metal impurities. For example, raw graphite contains more than 4000 ppm of Fe, and rGO prepared by Hummers method and Staudenmaier method could contain about 8000 ppm of Mn and 1600 ppm of Fe respectively.[171] According to **Figure 1-8b**, it is clear that the Mn residues in rGO sample contribute to the ORR activity greatly.[171] Therefore, it is recommended to avoid the using of commercial carbon sources during the synthesis of metal-free catalysts. Then, the ORR activity could be fully attributed to the active sites of metal-free catalysts.

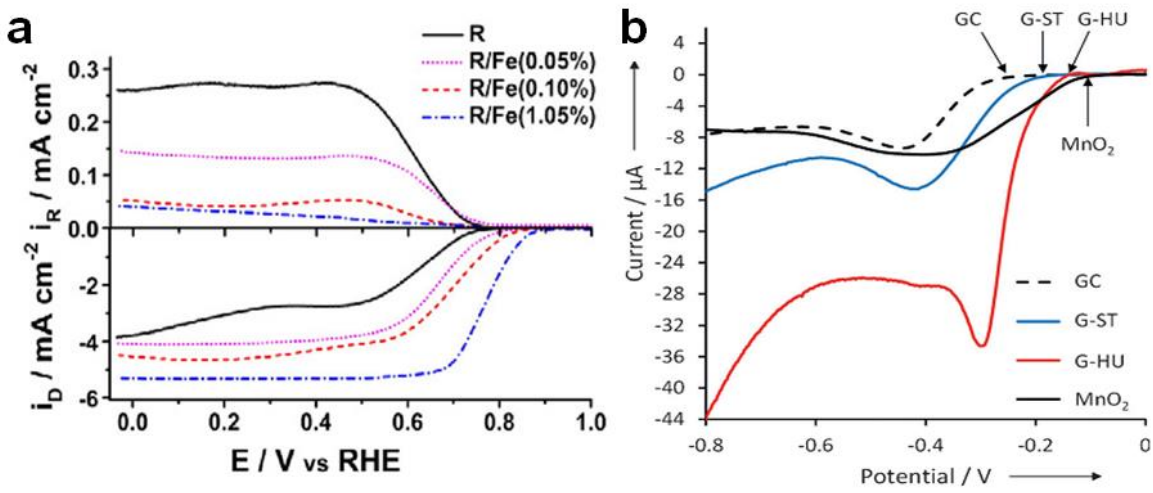

Figure 1- 8 Transition metal impurities. (a) LSV-RRDE profiles of the pyrolyzed carbons at different Fe content in an O_2-saturated 0.1M KOH electrolyte, rotated at 1600 rpm;[173] (b) LSV curves of a bare glassy carbon electrode (GC) and coated GC electrodes with rGO prepared by Hummers method (G-HU) and Staudenmaier method (G-ST) in O_2-saturated 0.1M KOH solution.[171]

1.5.3 Active sites of metal-free catalyst and associated mechanism

Similar to M-N-C catalyst, one reason why the metal-free catalyst performs well in the alkaline electrolyte is due to the decrease of the strength of anion adsorption on the surface of the catalyst in the alkaline medium.[119] On the other hand, it is related to the active site and ORR mechanism on the site. In the alkaline electrolyte, there are also two pathways for oxygen to be reduced, i.e. four electron pathway into hydroxyl ions at 0.401 V vs SHE and two electron pathway into peroxide species at -0.065 V vs SHE (**Equation 1-8**) respectively.

Four electron pathway: $O_2+2H_2O+4e^-\rightarrow 4OH^-$, 0.401 V vs SHE (1-5)

Two electron pathway: $O_2+H_2O+2e^- \rightarrow HO_2^- + OH^-$, -0.065 V vs SHE (1-8)

As to pure carbon materials, the naturally-existed oxygenated defects at the edges alter the electron cloud distribution and make the adjacent carbon atoms relatively nucleophilic in the alkaline media, leading to the side-on absorption of electrophilic O_2 molecule and the following reduction into peroxide species with two electrons and one water molecule (**Figure 1-9a**).[174] When the carbon is doped with heteroatoms, especially nitrogen, the ORR reduction pathway alters. The asymmetric polarization of C-N moieties resulted from the strong electronegativity of N atom gives arise to the favorable end-on mode of O_2 molecule adsorption.[175] Among all different nitrogen species (pyrollic, pyridinic, graphitic), pyridinic nitrogen makes the adjacent carbon atoms become Lewis base sites, which are identified as the active sites for metal-free catalysts.[19] As shown in the **Figure 1-9b**, the oxygen molecule is first adsorbed at the Lewis base site followed by protonation of the adsorbed O_2 into OOH group. Then, two possible pathways will occur: the four electron pathway that takes places at a single site and the 2+2 electron pathway which does not always take place at a single site. In the four-electron pathway, two protons attach to the two oxygen atoms in OOH group while two electrons participate in the breakage of the O-OH bond and formation of OH species. The adsorbed OH reacts with the last pair of proton and electron and generates another molecule of water. In the 2+2 electron pathway, the intermediate H_2O_2 formed via the hydrogenation and reduction of adsorbed OOH species would either leave the site or be re-adsorbed and further reduced by two protons into H_2O. No matter which ORR mechanism proceeds on the N-doped carbon, the initial adsorption oxygen molecules at the Lewis basic carbon atoms next to pyridinic N is essential and necessary for the reaction.[19]

Therefore, in the acidic electrolyte, pyridinic nitrogen tends to be protonated, leading to the decrease of basicity of adjacent carbon atoms (active sites) and hence the decrease of their affinity to O_2 and ORR activity. In other words, the ORR activity prohibited by the protonation of pyridinic nitrogen could recover in alkaline electrolyte.[118]

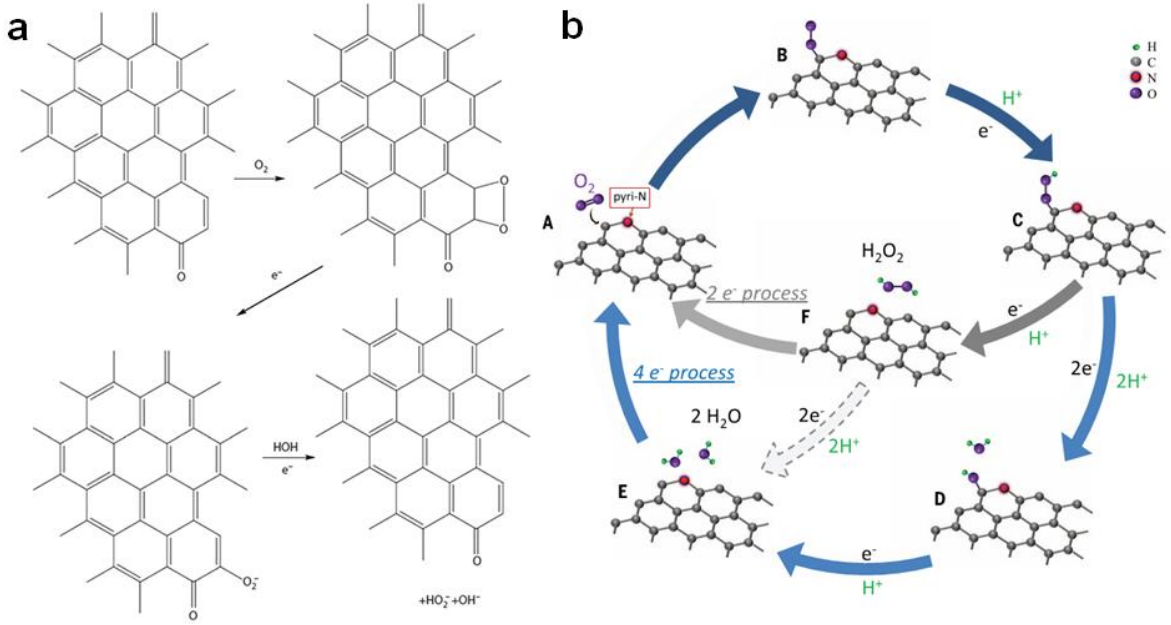

Figure 1- 9 ORR pathways on (a) natural carbon surface and (b) nitrogen doped graphene surface.

1.6 Organization of Thesis

The ultimate objective of this thesis is to develop and deliver low-cost NPMCs towards ORR that demonstrate high enough activity, durability, and PEMFC performance to replace the commercial platinum catalysts. To accomplish this, two approaches are explored in this thesis, namely Fe-N-C catalysts and metal-free catalysts. Initially, novel low-cost N, S-co-contained precursor, PRh is used together with cheap iron precursor ($FeCl_3$) and acid-treated carbon support (Ketjenblack EC 300) to synthesize the novel N,S-co-doped Fe-N-C

catalyst via multi-steps of high-temperature treatment and acid-leaching. The extra sulfur in PRh is designed to enhance ORR activity and PEMFC performance in the acidic environment. Then, to further reduce the cost, both metal precursor and carbon supports are omitted to synthesize low-cost metal-free catalysts. Additionally, the necessary purification steps of acid-leaching and the second heat-treatment due to the existence of extra metal species could also be omitted for the fabrication of metal-free catalysts, saving the potential labor cost. Thus, N-rich polymer precursor is selected to be directly converted into free-standing metal-free catalyst film via porous membrane casting and one-step heat-treatment. The novel fabrication methodology is designed to not only tune the porosity of catalyst, but also simplify the following fabrication of MEA, which could further reduce the cost of cell. Considering the resource of the polymer precursor and the concept of green chemistry, the earth-abundant biomass material, cellulose nanocrystal is applied to fabricate metal-free catalysts to further lower the cost and endow the procedure with extra environmental-benignity.

This project branches several important areas of electrocatalyst research and development. **Figure 1-10** displays the breakdown of the project tasks in this thesis. There are six chapters in this thesis. Chapter one is the introduction of the thesis, discussing the challenges and objectives as well as the background information for fuel cell and non-precious catalysts towards ORR. Chapter two lists the principle and the analysis methods for the most characterization techniques that are utilized in the discussed projects in this thesis. Chapter three focuses on the M-N-C catalyst synthesis, discussing a novel N, S-co-doped Fe-N-C catalyst derived from a novel nitrogen precursor as well as the sulfur effects on the active sites of M-N-C catalysts. The next two chapters mainly discuss metal-free catalysts

for ORR. In chapter four, a novel free-standing nitrogen-doped carbon film is developed and investigated, then it is proved to be a real metal-free catalyst. Chapter five includes a nitrogen-doped carbocatalyst derived from low-cost biomass materials (cellulose) as the metal-free catalyst towards ORR. The last chapter contains the summary of the important results and some discussion on the future work that may be taken.

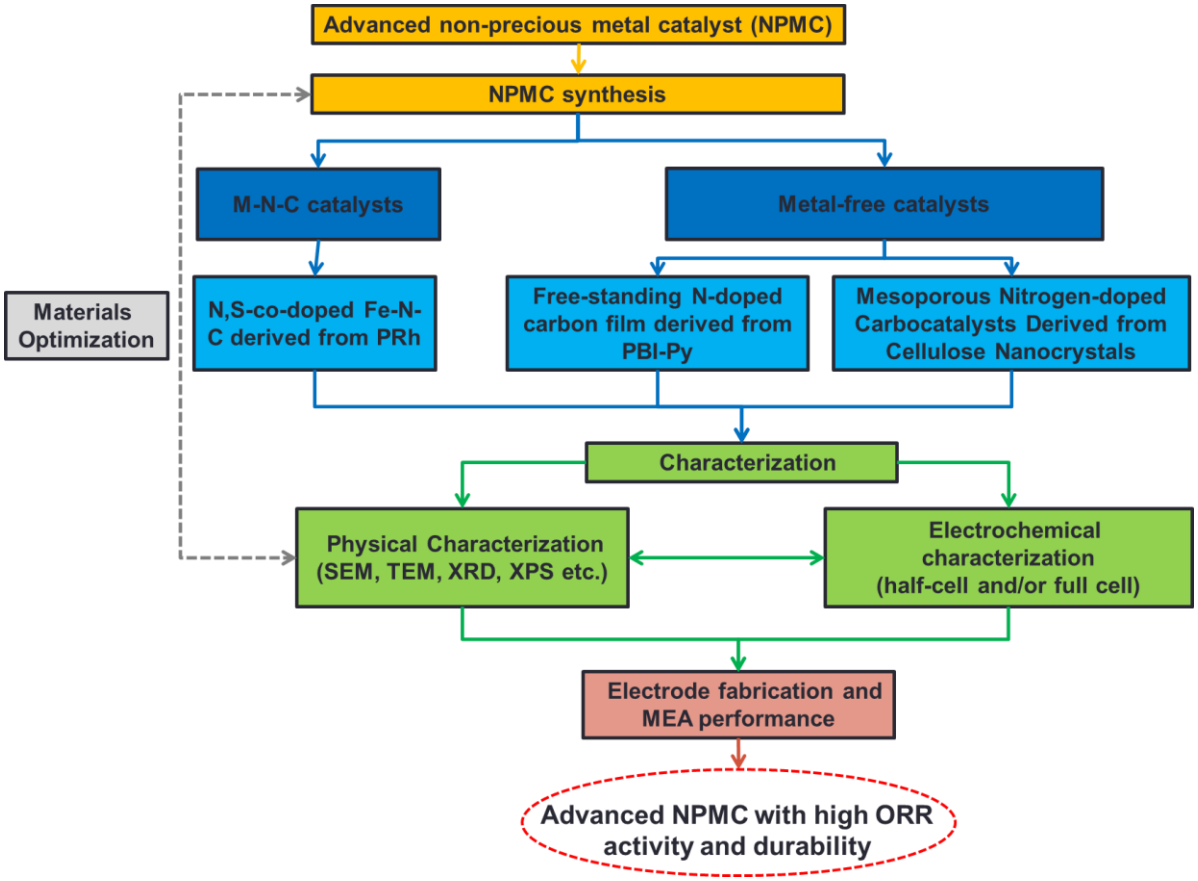

Figure 1- 10 Schematic of the project work flow.

Chapter 2: Characterization Techniques

A variety of physicochemical and electrochemical techniques are applied to extensively characterize the final electrocatalysts as well as the intermediates at each step to obtain information of chemical structure and composition, morphologies and crystal structure as well as electrocatalytic activity and durability. This not only could be applied to access ORR activity and optimize the synthesis of the catalysts, but also could provide the fundamental scientific knowledge about the catalyst itself and its possible behavior during oxygen reduction. Details of several physicochemical and electrochemical characterization techniques are illustrated in this section.

2.1 Physicochemical Techniques

Physicochemical techniques applied in the projects discussed in this thesis includes Fourier transform infrared (FTIR) spectroscopy, nuclear magnetic resonance (NMR) spectroscopy, inductively coupled plasma optical emission spectrometry (ICP-OES), X-ray photoelectron spectroscopy (XPS), scanning electron microscopy (SEM), transmission electron microscopy (TEM), energy-dispersive X-ray spectroscopy (EDX), gas (nitrogen) sorption analysis, X-ray powder diffraction (XRD), Raman spectroscopy,

2.1.1 Fourier Transform Infrared (FT-IR) Spectroscopy

FT-IR is a technique that is used to obtain an infrared spectrum of absorption or emission of testing sample and it is commonly used to identify the molecular structures of organic compounds. It could simultaneously collect high-resolution data over a wide range of spectrum in an easy and short test. The commonly used infrared spectrum range is mid-

infrared, with a wavenumber of 4000 - 400 cm^{-1} and wavelength of 2.5 - 25 μm. The related photon energies are so low that they could only excite the vibrational structure including covalently-bonded atoms and some chemical groups. Different organic groups could characteristically absorb the IR radiation and be excited to go through various vibrational motions. As a result, the loss of transmittance or the increase of absorbance at the specific wavenumbers or wavelengths indicates the existence of the functional group. Then the identification of different peaks on the spectrum for series of functional groups could be used to confirm the chemical structure of small molecules or polymers,[176] which are used as precursors for the catalyst. The more detailed feature of precursors could also be characterized by NMR as well as XPS.

2.1.2 Nuclear Magnetic Resonance (NMR) Spectroscopy

NMR spectroscopy relies on the NMR phenomenon of certain nuclei that have a nonzero spin in the applied strong constant magnetic field. Those isotopes contain an odd number of protons and/or neutrons are NMR-active, such as ^{1}H, ^{13}C, ^{15}N, ^{31}P and so on. To a certain nucleus, the chemical environment around could alter its local intramolecular magnetic field, hence change its resonance frequency, thus details of molecule structure could be distinguished. In order to characterize the different resonance frequency in the NMR spectroscopy, the concept of chemical shift is introduced and defined as the resonant frequency of a nucleus relative to a standard in a magnetic field. The most commonly-used standard reference is tetramethylsilane, $Si(CH_3)_4$, for both ^{1}H and ^{13}C NMR. Other than the characteristic chemical shift peak, the ratio of peak intensity and coupling could also provide the information of relative quantities of a nucleus in the same chemical environment in the

molecule. [176] Here, ^{1}H NMR is mainly used to identify the chemical structure of the synthesized polymer or small molecule precursor for NPMC catalysts in the discussed researches.

2.1.3 Inductively Coupled Plasma Optical Emission Spectrometry (ICP-OES)

ICP-OES is a powerful instrument to quantitatively detect trace amount of multiple elements in a sample. An argon plasma is ignited at the quartz torch through a spark of from Telsa coil and maintains the ionization via the radio-frequency induction coil.[177] The high temperature of the argon plasma could achieve as high as 10 000 K, which could get aerosol samples atomized and ionized.[178] Then, ions are excited and returned back to lower energy level, resulting in the emission of light with a characteristic wavelength for each element.[173] The characteristic light is captured by the photodetectors such as charge coupled devices qualitatively and quantitatively.[179] The ICP-OES is one of the most sensitive techniques for the detection of metal content in the samples. In the discussed researches, ICP-OES is applied to determine the iron content in the Fe-N-C catalysts and the trace amount of transition metals in metal-free catalyst to confirm its nature as metal-free catalyst.[173, 180] NPMC and metal-free catalyst were ashed and digested by mixed acid prior to the ICP-OES test. In order to guarantee the accuracy of the metal content in the catalyst, three replicas are conducted during the test and the results are expressed as mean value $\pm$ standard deviation. Specifically, due to the trace amount of transition metal in the metal-free catalysts, 200-500 mg of catalyst sample was applied to enrich the metal content for the test and minimize the systematic error.

2.1.4 X-Ray Photoelectron Spectroscopy (XPS)

XPS is a surface-sensitive technique that qualitatively and quantitatively measures elemental composition, chemical states, and electronic states existing in the sample material. The basic principle of XPS is to measure the kinetic energy and the number of electrons escaped from sample surface (0 - 10nm) when the sample is under the irradiation of a beam of X-rays.[181] When a highly focused beam of monochromatic Al K_α X-rays irradiate on the sample, the inner shell electrons and/or outer valence electrons are exited and escape from the surface of sample as the photoelectrons. Then the binding energies ($E_{binding}$) of electrons from different elements at different chemical environments and oxidation states could be identified according to the following equation from the work of Ernest Rutherford (1914),

$$E_{binding}=E_{photo}-(E_{kinetic}+\phi) \quad (2\text{-}1)$$

where E_{photon} is the energy of Al K_α X-rays photons (1486.7 eV), $E_{kinetic}$ is the measured kinetic energy of the photoelectron, ϕ is the work function that nearly is a constant for a particular the spectrometer.[182, 183] Moreover, XPS could also be applied to quantitatively analyze the surface chemical composition based on the following equations,

$$\boldsymbol{I = nS} \quad (2\text{-}2)$$

$$\boldsymbol{C_x = \frac{n_x}{\sum n_i} = \frac{I_x/S_x}{\sum(I_i/S_i)}} \quad (2\text{-}3)$$

where $\boldsymbol{I}$ is area of photoemission peak (counts s^{-1}), $\boldsymbol{S}$ is element sensitivity factor based on empirical data (cm^3 s^{-1}), $\boldsymbol{C_x}$ is the relative concentration of element or component x in the sample.[184] XPS is such a powerful technique for chemical analysis that it is also been called Electron Spectroscopy for Chemical Analysis (ESCA). In this work, XPS was applied to analyze the chemical composition of a variety of elements, such as carbon, nitrogen, iron,

sulfur, oxygen in the final NPMC as well as some intermediates. The composition is obtained as the mean value of the element from two or three spots of same sample. Additionally, different species or oxidation states of those elements, especially nitrogen, would be identified and quantified, hence it could be linked to the structure of active sites of NPMC towards to ORR.

2.1.5 Scanning Electron Microscopy (SEM)

SEM is one of the most commonly-used techniques to investigate the morphology of nanomaterials. It is a type of electron microscopy that captures different signals from emitted from the surface of the sample when it is irradiated by high-energy electron beam, including secondary electrons (SE), back-scattered electrons (BSE), characteristic X-rays, cathodoluminescence (CL) and so on. Among them, imaging based on SE is the most commonly used due to the shallowest and smallest interaction volume with sample and associated high-resolution and magnification.[185] Other than sample's morphology and the surface topography, SEM could also be used to analyze the chemical composition via detecting the characteristic X-rays through the equipped EDX apparatus. In the discussed projects in this thesis, SEM is utilized to illustrate the nanostructure of NPMC and metal-free catalysts as well as those intermediates.

2.1.6 Transmission Electron Microscopy (TEM)

TEM is a microscopy technique that an ultra-thin specimen is placed in the pathway of a beam of electrons from electron gun to the detector. An image is formed from the interaction of the electrons with the sample as the beam is transmitted through the specimen and it will be magnified and focused by an objective lens.[186] As the de Broglie wavelength

of electrons is much lower than that of visible light, thus the resolution of TEM is much higher that of optical microscopy. Moreover, since the applied accelerating voltage of TEM is higher than that of SEM (30-100 kV *vs.* 5-30 kV) and the principle that de Broglie wavelength is inversely proportional to the square root of accelerating voltage,[187] the resolution TEM is higher than that of SEM too. Thus, TEM is widely applied to study the underlying inner structures of sample as well as its ultra-fine nanostructure, while SEM is mainly used to investigate the surface topography and morphology.

Additionally, high angle annular dark field scanning transmission electron microscopy (HAADF-STEM) could also be applied to a STEM detector and a HAADF detector. As HAADF image intensity is approximately proportional to the square of atomic number,[188] HAADF-STEM is the ideal TEM imaging technique for heterogeneous sample to distinguish the distribution and composition of high atomic number component. In this study, TEM is utilized to image the advanced nanostructures of both NPMC and metal-free catalyst and detect the metal-contained nanoparticles in both final catalysts and intermediates.

2.1.7 Energy-dispersive X-ray (EDX) spectroscopy

EDX apparatus is commonly integrated with SEM and TEM and the EDX spectrum and associated line scan and mapping techniques could be carried out concurrently with those imaging techniques. Basically, EDX detects the characteristic X-rays emitted from the surface of sample when it interacts with the electron beam in either SEM or TEM. The characteristic X-rays is originated from the phenomenon that an electron at the outer higher-energy shell fills the electron hole at the inner lower energy shell after the pristine electron is ejected by the electron beam. The measured X-ray intensities also indicate relative atomic

percentages of elements in the sample. Therefore, EDX could be used to identify and quantify the elements in the sample.[189] In the combination with image techniques, elemental mapping and line scan could be utilized to not only illustrate the element distribution, but also distinguish the specific nanostructure like core-shell and alloy nature.[190] In this thesis, EDX is applied to provide the information of chemical composition for electrocatalysts and the elemental distribution along with the nanostructure of both final catalysts and intermediates.

2.1.8 Gas Adsorption Analysis

The gas adsorption analysis is using physical adsorption of gases, normally nitrogen or argon, onto solid materials to measure the specific surface area and pore-size distribution of solid materials. The solid sample is degassed and cooled to 77 K in the liquid nitrogen prior to the test. Then, the inert gases start to physically adsorb on the surface of the sample, forming a monolayer of gas molecules first and then liquid-like multi layers gas until the pressure saturated.[191] An adsorption-desorption isotherm is usually obtained, constructing the volume of gas adsorbed *vs.* the relative pressure. According to the Brunauer-Emmett-Teller (BET) theory, the specific surface area of sample could be calculated as the monolayer of gas molecules formed based on the adsorption-desorption isotherm at relative pressure of 0.05 – 0.35.[191] On the basis of the shape of adsorption-desorption isotherm, the pore structure could be classified and identified, such as the characteristic high gas adsorption at low relative pressure (< 0.05) for micropores (< 2 nm) and the hysteresis loops for mesopores (2 - 50 nm).[192] The exact pore-size distribution could be conducted through different methods, commonly t-plot method for external surface area and micropore surface

area and Barrett-Joyner-Halenda (BJH) for macro- and meso-pore size distribution. Recently, a new method of density functional theory (DFT) is developed for pore-size distribution, especially suitable for micro- and meso-porous sample.[193] In this research, gas (nitrogen) adsorption analysis is utilized to obtain the information of surface area including BET surface area, external surface area, and micropore surface area as well as the pore size distribution for both M-N-C catalysts and metal-free catalysts. For further investigation on the effect of surface area on ORR activity, the values of BET surface area, external surface area, and micropore surface area are the averages of the data obtained from three nitrogen adsorption tests for duplicate samples.

2.1.9 X-ray Powder Diffraction (XRD)

X-ray Powder Diffraction (XRD) is a versatile characterization technique for the identification of crystal structure of materials and provide the crystallographic information as well as associated chemical composition.[194] The obtained XRD pattern results from constructive interference of monochromatic X-rays and a crystalline sample. When the interplanar spacing in the powder and interference condition satisfies the Bragg's Law (Equation 2-4), a peak will be observed in the XRD pattern,

$$n\lambda = 2d\ sin\theta \tag{2-4}$$

where n is any integer, λ is wavelength of incident X-rays, d is the spacing between diffracting planes and θ is the diffraction angle. By the comparison of obtained XRD pattern with the standard diffraction pattern in the database, the different chemical components in the sample could be identified. The average crystallite size (Lc) could also be calculated using the Scherrer–Debye equation:[195, 196]

$$Lc = K\lambda/(\beta cos\theta) \quad (2\text{-}5)$$

where K is shape factor, λ is the wavelength of X-ray, β denotes full width at half maximum of diffracting peak in radians, θ denotes the Bragg's angle. In the research projects discussed in the thesis, XRD is used to identify the iron species in the Fe-N-C catalysts and associated intermediates and investigate the crystalline structure of carbon in both Fe-N-C catalysts and metal-free catalysts.

2.1.10 Raman spectroscopy

Raman spectroscopy is a spectroscopic technique based on Raman effects that the wavelength of scattered light shifts as compared to that of the incident visible or near-infrared beam due to the interaction of photons with the chemical structure of sample. Although there is a striking similarity between Raman spectra and IR spectra, the advantages of negligible influences of water and glass and special activity to certain bonding for certain materials, especially for inorganic materials make Raman spectroscopy a routine tool for materials science. In this study, Raman spectroscopy is mainly used to characterize the crystal structure of carbon in either M-N-C catalyst or metal-free catalyst. For example, in the **Figure 2-1**, two typical peaks of carbon materials, the G-band at 1600 cm^{-1} and D-band at 1340 cm^{-1} are observed in the Raman spectra for sp^2 carbon domain and structural defect sites within the graphene plane, respectively.[195, 196] The intensity ratio of D and G band, I_D/I_G, is considered as an indicator of the degree of disorder and defects in carbon-based materials. Besides, the in-plane crystallite size La (nm) could also be estimated via Tuinstra–Koenig relationship:[195, 196]

$$L_a = (2.4 \times 10^{-10})\lambda^4 (I_D/I_G)^{-1} \quad (2\text{-}6)$$

where λ is the wavelength of Raman excitation.

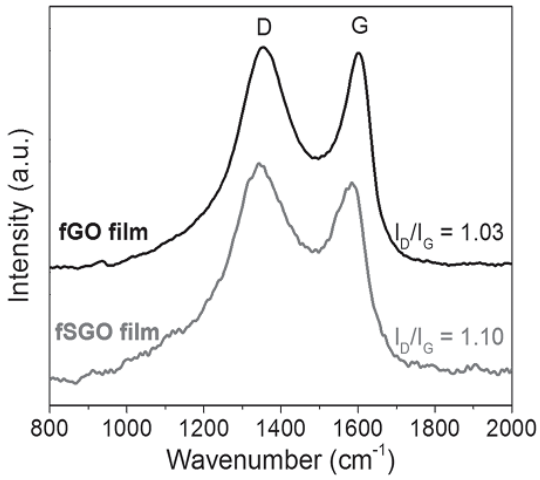

Figure 2- 1 Raman spectra for fGO and fSGO films [195]

2.2 Electrochemical and performance characterization

To investigate the activity and durability of synthesized catalysts towards ORR, electrochemical measurements are required. Both half-cell measurements and full cell tests are explained here.

2.2.1 Half-cell Measurements

2.2.1.1 Rotating disk electrode (RDE)

The RDE test is a well-established electrochemical technique to investigate the electrochemical activity of various electrocatalysts towards different electrocatalytic reactions, especially for ORR. RDE is an efficient and effective tool to screen electrocatalysts towards ORR and to study the mechanism of ORR on the catalyst. Half-cell RDE test is commonly conducted in an electrochemical cell with typical three electrodes system shown in the **Figure 2-2**. The electrolytes applied in the discussed projects are 0.1 M KOH as alkaline medium and 0.5 M H_2SO_4 as acidic medium for both M-N-C catalysts and

metal-free catalysts. As comparison, the benchmark commercial Pt/C catalyst will be tested in 0.1 M KOH as alkaline medium and 0.1 M $HClO_4$ as acidic medium. The working electrode (WE), i.e. RDE is a catalyst-coated glassy carbon disc. The preparation of WE includes two steps: (1) preparing the catalyst ink via ultrasonically dispersing catalyst in a solvent, normally water, ethanol, isopropanol, 1-propanol or the mixture of them; (2) drop-casting certain volume of catalyst ink onto RDE to reach designed catalyst loading on the electrode. Then one drop of dilute Nafion solution is deposited onto the surface of catalyst layer. Alternatively, it could be mixed with the ink previously. The ink composition, choice of solvent, ratio of Nafion to catalyst and its deposition method are all material specific. The counter electrode (CE) applied in this research is a graphite rod for both M-N-C catalysts and metal-free catalysts. As to reference electrode (RE), silver chloride electrode (Ag/AgCl) or reversible hydrogen electrode (RHE) is used for acidic electrolyte while RHE or saturated calomel electrode (SCE) is applied for alkaline electrolyte.

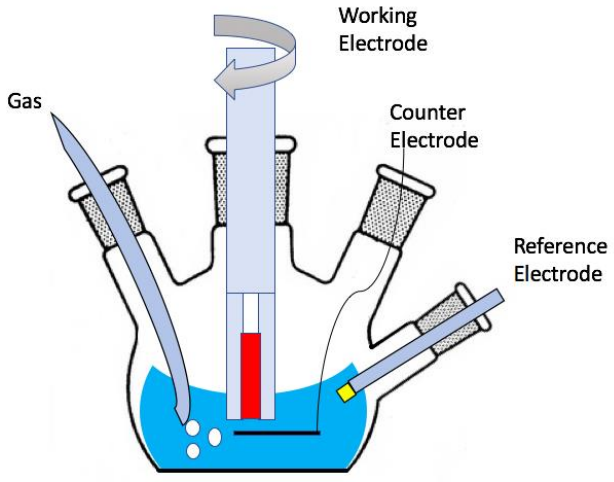

Figure 2- 2 Standard three electrode cell used for RDE measurements, reprinted in adapted form[197]

In a typical measurement of ORR activity, cyclic voltammetry (CV) is firstly applied for catalyst in the N_2-saturated electrolyte to remove the surface air bubble and clean the surface until the CV curves stabilize and overlap with each other. The potential range is 0 to 1.05 V vs. RHE in both acidic and alkaline medium and potential scan rate is 50 mV s^{-1}. Then, linear sweep voltammetry (LSV) is performed with a scan rate of 5 or 10 mV s^{-1} to obtain the background (capacitive) current density. After the saturation of oxygen in the electrolyte, several other CV cycles are performed to confirm the catalytic capability of catalyst towards oxygen reduction. Then, the typical ORR polarization curve (**Figure 2-3**) could be obtained via the LSV curve after the deduction of the background current density.

Apparently, there are three different regions, representing three different ways that ORR is controlled. In the kinetic-controlled area, the reaction rate is so slow that the increase of current density along with the decrease of potential is hard to be observed. Then as the potential decreases, the current density dramatically increases in this mixed kinetic- and diffusion-controlled zone, indicating the significant increase of ORR reaction rate. When the potential continues to decrease, the process of reactants diffusing from bulk solution to the surface of electrode limits the reaction rate, resulting in a plateau region, labeled diffusion-controlled zone in **Figure 2-3**.[198] Then ORR activity could be evaluated and compared on the basis of the following three parameters: (1) On-set potential ($E_{on\text{-}set}$), the potential where the LSV curve starts to drop; (2) Mass transport limiting current density (i_L), the plateau current density in the LSV curve; (3) Half-wave potential ($E_{1/2}$), the potential where the current density reaches exactly half the value of i_L. Since ORR in the RDE system is controlled by the sluggish kinetic of reaction itself as well as the mass transport or diffusion process of reactants, the parameter that locates at mixed kinetic- and

diffusion-controlled zone, $E_{1/2}$ is considered as the major indicator to assess ORR activity. Besides, by definition, the measure of $E_{1/2}$ also includes the reading of i_L. Therefore, the higher $E_{1/2}$ is, the more ORR-active is the catalyst.

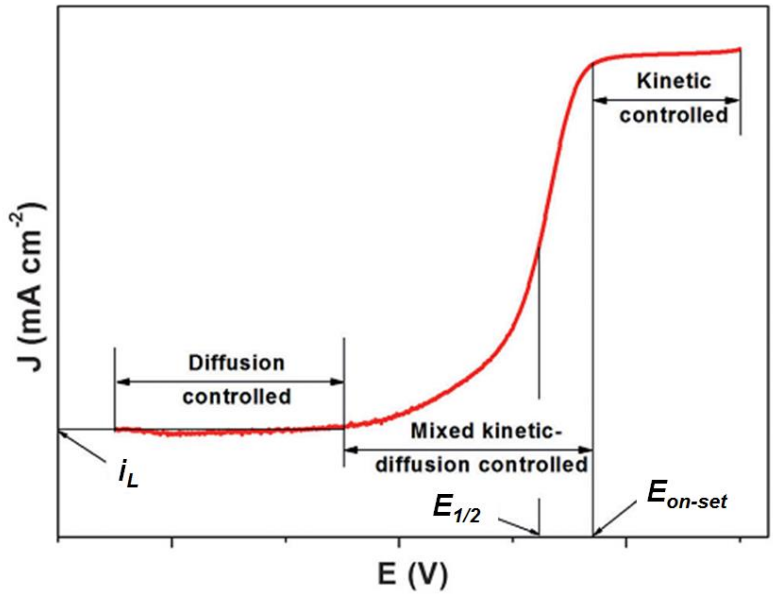

Figure 2- 3 Typical ORR polarization curve.[198]

When the working electrode is rotated at different speed, associated polarization curves could be plotted together in a similar way to **Figure 2-4a**. Clearly, the limiting current density increases along with the rotation speed. Based on the following Levich equation (Equation 2-7), i_L is proportional to the square root of rotation rate.

$$i_L = 0.62nFD_o^{2/3}\upsilon^{-1/6}C_o\omega^{1/2} \quad (2\text{-}7)$$

where n is the number of transferred electrons, F is the Faraday constant (96 485 C mol^{-1}), D_o is the diffusion coefficient of O_2 (1.90×10^{-5} cm^2 s^{-1} in 0.1 M KOH and 1.40×10^{-5} cm^2 s^{-1} in 0.5 M H_2SO_4), υ is the kinetic viscosity of electrolyte (0.01 cm^2 s^{-1} in both 0.1 M KOH and 0.5 M H_2SO_4), C_o is the concentration of O_2 in the electrolyte (1.20×10^{-6} mol cm^{-3} in

0.1 M KOH and 1.10 x 10^{-6} mol cm^{-3} in 0.5 M H_2SO_4) and ω is the angular frequency of the rotation (rad s^{-1}) and the constant *0.62* is adopted when rotation speed is expressed in rad s^{-1}.

As discussed above, ORR has sluggish kinetics which controls the reaction behavior on the surface of electrode together with diffusion or mass transport. Therefore, the polarization curves are slightly distorted from the standard shape of the sigmoidal wave. In this case, to distinguish kinetic current density from measured current density (*i*), Koutecky-Levich equation (Equation 2-8) is applied.[199]

$$i^{-1} = i_k{}^{-1} + i_L{}^{-1} \quad (2\text{-}8)$$

where i_k and i_L are the kinetic current and mass transport limiting current density respectively. Then, by combining equation 2-7 and 2-8 together, the linear relationship between i^{-1} and $\omega^{-1/2}$ could be derived in equation 2-9.

$$i^{-1} = i_k{}^{-1} + B^{-1}\omega^{-1/2} \quad (2\text{-}9)$$

where B is the Levich constant and equal to $B = 0.62nFD_o^{2/3}\upsilon^{-1/6}C_o$. Therefore, a set of polarization curves at different rotation rate could be used to plot i^{-1} against $\omega^{-1/2}$at different potential (overpotential), leading to the Koutecky-Levich plot in **Figure 2-4b**. The obtained slope could be used to calculate the number of transferred electrons (*n*) in ORR, which is related to the reaction mechanism, i.e. four-electron pathway and/or two-electron pathway, and selectivity of catalyst. As to platinum catalyst, the ORR reaction on its surface is nearly four electron pathway, i.e. $n \approx 4$. As to NPMC, the mechanism is the mixture of those two pathways according to the description in section **1.4.3** and **1.5.3**, i.e. $n \in [2, 4]$. Apparently, the four electron pathway is efficient and desirable as only water is product. As to two electron pathway, not only does it works less efficient, but also undesirable peroxide species

could cause deactivation of catalyst and significant degradation of polymer electrolyte membrane hence affect the performance and stability of PEMFC.[128-131] Therefore, the higher the selectivity of NPMC towards four electron reduction of oxygen to water is, i.e. $n \rightarrow 4$, the more active and desirable the NPMC is.

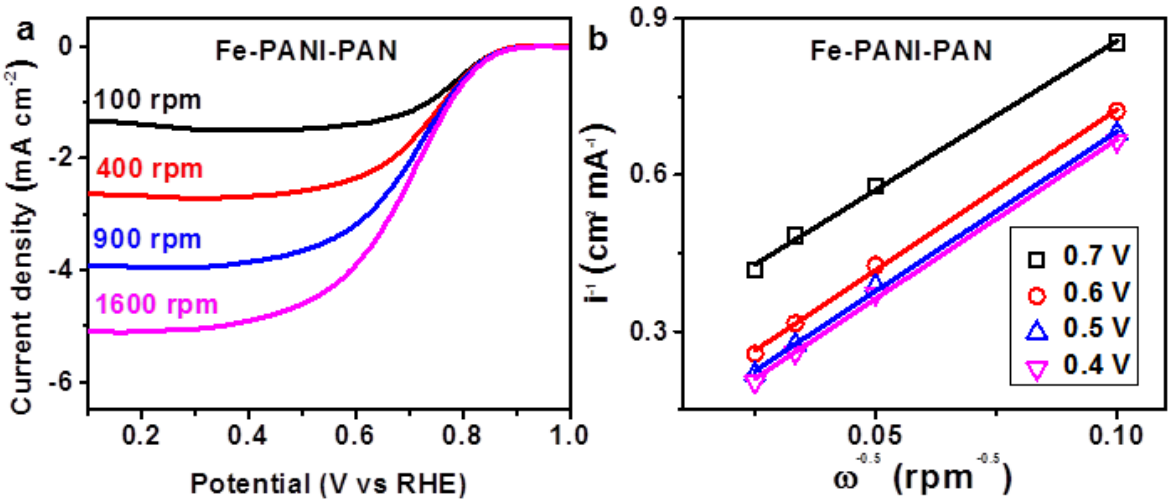

Figure 2- 4 (a) Polarization curves of Fe-PANI-PAN performed in O_2 saturated 0.1 M $HClO_4$ at different rotational speed, and (b) the associated Koutecky–Levich plots.[200]

In order to investigate the kinetic behavior of ORR on catalyst, Tafel equation (equation 2-10) is introduced as follows:

$$\eta = A \log\left(\frac{i_k}{i_0}\right) \tag{2-10}$$

where η is the overpotential, i_k is kinetic current density, i_0 is the exchange current density and A is the Tafel slope obtained from the Tafel plot, for instance **Figure 2-5**. Tafel slope indicates the ability of catalyst-coated electrode to increase the kinetic current density via increasing overpotential. The slope is an important and characteristic kinetic parameter for ORR catalyst. It is also determined by

$$A = \frac{2.303\,RT}{\alpha n_o F} \tag{2-11}$$

where R is the universal gas constant, T is absolute temperature, F is Faraday constant, and α is charge transfer coefficient, n_o is the electron transfer number in rate determining step.[201] Both α and n_o are related to the catalyst itself. The charge transfer coefficient signifies the fraction of the interfacial potential at an electrode-electrolyte interface that helps in lowering the free energy barrier for the electrochemical reaction. Typically, for ORR at Pt surface, α is around 0.5. However, according to **Figure 2-5**, there are two regions with different Tafel slope, namely 60 mV dec^{-1} at low current density region and 120 mV dec^{-1} at high current density region.[202] This is attributed to two different values of n_o for two different reaction mechanisms. At low current density region, ORR occurs on a Pt/PtO surface and the rate determining step is a pseudo 2-electron procedure ($n_o = 2$), while at high current density region, ORR occurs on a pure Pt surface, the first electron transfer is the rate determining step ($n_o = 1$). [201] As to NPMC, its Tafel slope is normally higher than that of Pt-based catalyst at the low current density region, ie. 60 mV dec^{-1}, which is due to ohmic or diffusional losses.[203]

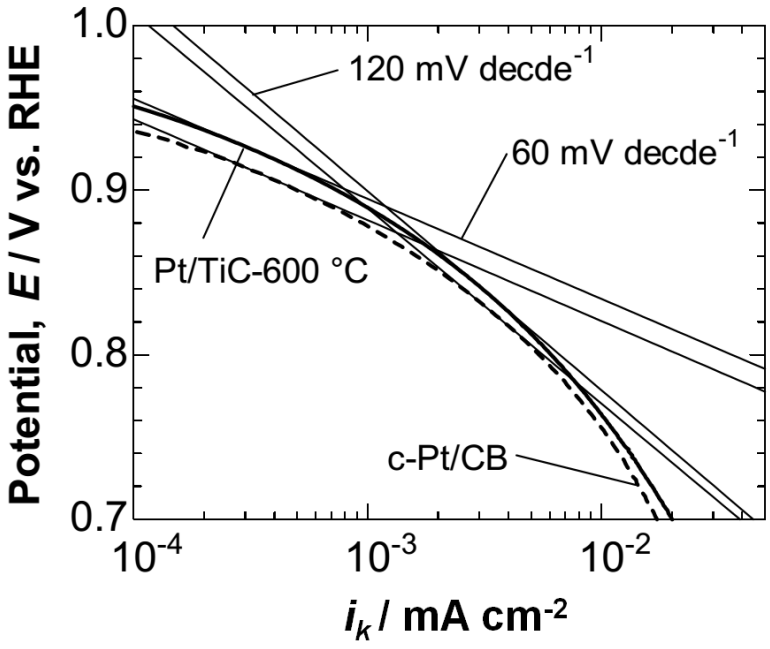

Figure 2- 5 Tafel plots for the ORR at Pt/TiC-600 ℃ and commercial Pt catalyst on carbon black (c-Pt/CB) in O_2-saturated 0.1 M $HClO_4$ solution at 25 ℃ with the rotating rate of 1500 rpm and the potential sweep rate of 5 mV s^{-1}.[202]

2.2.1.2 Rotating ring disk electrode (RRDE)

RRDE test is another technique for the investigation of ORR kinetic. As shown in the **Figure 2-6**, there is platinum ring electrode outside the glassy carbon disk electrode with a Teflon insulating spacing in between. The dominant reaction occurred at the central disk electrode is the direct reduction of oxygen into water via the four electron pathway. The intermediate peroxide species like H_2O_2 through the two electron pathway could be detected at the ring electrode when it is oxidized at a set potential.[129] Therefore, the recorded disk current density (I_D) is the sum of oxygen reduction current to water (I_{H_2O}) and to intermediates ($I_{H_2O_2}$).Then, there are following equations:

$$I_D = I_{H_2O} + I_{H_2O_2} \quad (2\text{-}12)$$

$$I_{H_2O_2} = I_R/N \quad (2\text{-}13)$$

where I_R is the ring current density and N is the collection efficiency of RRDE which it is measured using a well-behaved ferrocyanide/ferricyanide redox couple.[204] Typically, RRDE is placed in 1.0 M KNO_3 solution containing 10 mM of $K_3Fe(CN)_6$ and rotated at different rates. The potential is scanned negatively on disk electrode while the ring electrode is set at a positive (oxidizing) potential. Then, parts of ferricyanide generated from the reduction of ferrocyanide at disk electrode are diffused to ring electrode and reduced back to ferricyanide on site. Then, obtained limiting current on disk ($i_{L,\,Disk}$) and ring electrode ($i_{L,\,Ring}$) could be used to calculate the collection efficiency (N) on the basis of the following equation:

$$N = -i_{L,\,Ring}/i_{L,\,Disk} \quad (2\text{-}14)$$

Then, the number of transferred electrons (n) and the yield of peroxide ($H_2O_2\%$) could be derived as follows:

$$n = \frac{4\,I_D}{I_D + I_R/N} \quad (2\text{-}15)$$

$$H_2O_2\% = \frac{200\,I_R/N}{I_D + I_R/N} \quad (2\text{-}16)$$

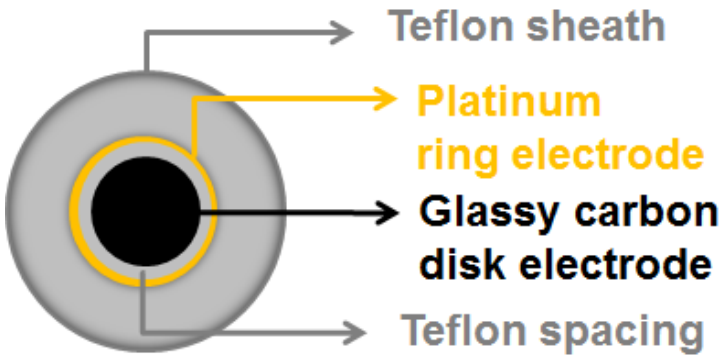

Figure 2- 6 A schematic of RRDE.

2.2.1.3 Accelerated degradation testing (ADT)

ADT is a well-recognized protocol to investigate the durability of the catalyst in a shortened period via the RDE technique in the half-cell measurement. Usually, it is conducted through repeated CV cycles (typically several thousand at least) with certain potential range, such as 0.6 – 1.0 V as recommended by DOE, in a N_2-saturated electrolyte. By the comparison of polarization curves before and after ADT, the durability of the catalyst is visualized and quantified.[205]

2.2.2 Membrane Electrode Assembly and Full-cell Measurements

Although the results from half-cell measurements could be utilized to assess and investigate the ORR activity of NPMC, they could not directly reflect and foresee the actual performance in the real PEMFC due to the differences in testing conditions and many other factors. After a highly active NPMC is screened via the RDE tests, a full-cell measurement is conducted via a single cell test employed a NPMC-based membrane electrode assemblies (MEA). Generally, an NPMC-based MEA consists of a NPMC-based cathode and a commercial Pt/C anode sandwiched with a polymer electrolyte membrane (PEM) in the middle. There are two major techniques for cathode fabrication, namely catalyst coated on gas diffusion layer (CCG) and catalyst coated on membrane (CCM). Various catalyst coating techniques are available, including spraying, painting, filtering, screen-printing and so on.[206] Those techniques are chosen for different projects according to its objective. The most common technique in the discussed projects is the combination of CCM and painting technique. No matter what technique is selected to fabricate the cathode, the following step of hot-press is the same and necessary, ensuring uniform contact and adhesion. Then, the obtained MEA is assembled into the fuel cell testing station and ready to be assessed.

After all the condition parameters reach the DOE-recommended values, including cell temperature, humidity, back pressure and fuel flow rate, a few cycles of voltage scan will be run to ensure adequate hydration of PEM and activation of the catalyst prior to the test. Then, a typical polarization curve, cell voltage against current density, along with the power density plot versus current density could be obtained with steady voltage scan. Alternatively, in order to simulate the real operational condition, air could be used at cathode.

2.2.3 Error analysis

To obtain the accurate and trustworthy electrochemical data for all the NMPCs, repeatable tests are conducted. Initially, to screen samples and to optimize the parameters for catalyst synthesis including the ratio of precursors, pyrolyzing condition, catalyst loading and so on, each catalyst ink is coated on the GCE and tested in RDE system twice to confirm the ORR activity. Once the preparation parameters are selected, the same catalyst needs to be reproduced for another two times. The associated polarization curves from different batches are compared to show the repeatability among batches and to minimize systematic error during the synthesis. For H_2-Air PEMFC performance, three identical MEAs are fabricated and tested at the same experimental condition.

The main sources of error are systematic errors and come from the following factors:

(i) Imperfect calibration of measurement instruments

For half-cell tests, the potential drift of reference electrode and oxidized surface of counter electrode could affect the accuracy of measurement. To avoid this, each reference electrode is calibrated bi-weekly and counter electrode is polished prior to every RDE test.

(ii) Methodic error

There are quite a few experimental conditions that could contribute to the error for electrochemical data, such as the variation of electrolyte concentration, purity of the gases and electrolyte, oxidized layer of GCE and so on. To avoid those errors, the specific procedures need to be followed. The electrolytes are prepared with high purity reagents and DDI water (resistivity > 18 MΩ cm) via volumetric flask. Ultrapure gases are used for catalyst synthesis, half-cell and single cell tests, such as 99.999% Ar, 99.999% H_2, 99.998% N_2 and 99.995% O_2. The GCE surface is polished with 0.05-micron alumina paste (Buehler, Lake Bluff, IL) and then sonicated in distilled water and isopropyl alcohol prior to coating of catalyst.

(iii) Environmental errors

As temperature could affect the oxygen solubility in the electrolyte in the half-cell test, the special design of the electrochemical cell with a water bath preset at 25^{o}C is applied to avoid the variation of temperature during the test.

(iv) Personal errors or operational errors

Those complicate experimental procedures that require technical experience, for instance the catalyst coating on GCE, MEA fabrication and PEMFC testing could bring errors to the final electrochemical data if not performed properly. To avoid this error, two precautions are taken. One is to standardize the procedure and the other is to ensure the operators are well-trained.

Chapter 3: Boosted Performance of Novel N, S-co-doped non-precious metal Catalyst Towards Oxygen Reduction via Comprehensive Effects of Sulfur on Active Sites

This chapter is reprinted from the manuscript submitting to *Journal of Materials Chemistry A.*

G. Jiang, J. Choi, J. Li, X. Fu, P. Zamani, P. Xu, J. Li, G. Lui. D. Banham, S. Ye, Z. Chen[a]*. Boosted Performance of Novel N, S-co-doped non-precious metal Catalyst Towards Oxygen Reduction via Comprehensive Effects of Sulfur on Active Sites. *Journal of Materials Chemistry A.*2017

3.1 Introduction

To address the global energy and environmental challenges, renewable electrochemical energy systems emerge as the promising solutions.[207, 208] Oxygen reduction reaction (ORR) is one key reaction in a variety of electrochemical energy systems, including metal-air batteries and proton exchange membrane fuel cell (PEMFC).[2, 5, 209-212] However, ORR is a rather slow reaction and requires transition metal catalysts and/or heteroatoms-doped carbon catalysts to accelerate the reaction in the alkaline/organic electrolyte for metal-air batteries.[210-213] As to PEMFC, ORR becomes more sluggish in its highly-oxidative acidic operational environment, which requires expensive platinum-based catalysts to accelerate the reaction so that PEMFCs can meet the commercial requirements.[5] Although extensive efforts have been made to lower the loading of platinum, increase the utilization of platinum and enhance the durability of the catalyst in the last decade,[214-216] platinum-based catalysts

cannot be the long-term solution as any progress will be offset by the increasing price of platinum due to high demand.[5, 217] As a result, catalysts made from earth-abundant materials, called non-precious metal catalysts (NPMCs) quickly come under the spotlight as the promising alternative.[2, 217]

NMPCs have evolved greatly from cobalt phthalocyanine, whose ORR activity in basic media was firstly reported in 1965,[218] to more recent high-temperature treated transitional metal-nitrogen-carbon (M-N-C) composites, showing comparable ORR activity to Pt/C catalyst even in harsh acidic electrolyte.[16, 17] Excellent progress has been made with regard to M-N-C catalysts in the last decade, especially in acidic electrolyte, demonstrating the enhancement of ORR activity and durability by using novel high performance nitrogen precursors, including 1,10-phenanthroline,[17] polyaniline,[16, 62, 95, 96] polypyrrole (PPy),[69] poly(phenylenediamine),[71, 72, 97] ionic liquid,[68] metal-organic framework (MOF)[38, 47, 74] and the combination of different precursors.[38, 47, 74, 98] However, progress on the understanding of active sites in M-N-C catalysts is surprisingly slow due to the nature of heterogeneity of M-N-C catalyst and lack of proper quantification methodologies. In order to further enhance the activity and durability of M-N-C towards ORR through rational designs, a better understanding of active sites towards ORR is required. The most commonly recognized structure of the active sites in M-N-C is the coordinate of transition metal ions and nitrogen (MeN_x), especially FeN_x sites. Several different structures of FeN_x sites were identified and prove to be highly active towards ORR.[47, 74] Meanwhile, iron nanoparticles encapsulated in a few layers of carbon were also proposed as the ORR active sites that can catalyze the cascade reactions of $2e^-$ reduction steps via peroxide intermediate.[48, 96] Besides, N-doped carbon structure, especially pyridinic nitrogen is also recognized as the active site in the

basic electrolyte.[208] Although it was also reported to be active in the acidic electrolyte,[19] its relatively weak activity in acid and trace metal residue make this active site debatable.[171]

Recently, the enhancement in ORR activity brought by co-doping of heteroatoms (S, P, B) in N-doped graphene [160, 219, 220] provides insight and a clue to further improve the activity and durability of Fe-N-C catalysts. For instance, the Fe-P bond was reported as an active site towards ORR,[115, 116] S-doped iron precursor was found to further enhance the ORR activity[71] and the functional groups of 2',6'-diphenylphenthioether on iron phthalocyanine (FePc) were shown to enhance the durability of FePc catalyst.[221] Among all the heteroatoms, it seems that sulfur is likely to have more pronounced positive effects on Fe-N-C catalysts. Thus, if the effects of sulfur on the active sites of Fe-N-C catalyst can be comprehensively understood, then a more rational design of Fe-N-C catalysts can be derived accordingly.

Herein, we synthesize an N, S-co-doped Fe-N-C catalyst from a novel N, S-contained precursor called polyrhodanine (PRh) and compared it with a Fe-N-C catalyst derived from PPy. Using advanced physical characterization, we found that the introduction of sulfur in the nitrogen precursor has comprehensive effects on the active sites of Fe-N-C catalysts. First, sulfur can tune the synthetic chemistry to benefit the formation of Fe-N_x active sites through (i) altering the main intermediates from iron/iron carbide (Fe/Fe_3C) to iron sulfide (FeS) during the first pyrolysis, (ii) increasing the solubility of intermediates (Fe/Fe_3C or FeS) during the acid-leaching and (iii) reducing the destruction of active sites during the Fe/Fe_3C catalyzed graphitization of carbon during pyrolysis. Second, sulfur can enhance the accessibility of active sites by forming a porous, high surface area structure. Moreover, according to the density functional theory (DFT) calculation, the introduction of

S-doping in the typical Fe-N_4 active sites can not only enhance the electron transfer at 0.8V vs RHE, but also increase the cohesive energy of active sites in the presence of oxygen. These changes result in excellent ORR activity, selectivity, and durability of N, S-co-doped Fe-N-C catalyst in the half-cell test as well as one of the best-reported performances in a H_2-air PEMFC.

3.2 Experimental

3.2.1 Catalyst Synthesis

As shown in **Figure 3-1,** for PRh-derived Fe-N-C catalyst, the typical synthesis method is as follows: 1.1 g (8.25 mmol) of rhodanine was first dissolved in 100 mL hot water (70^{o}C) on a hotplate. Then 20 mL of a sonicated, homogeneous, aqueous mixture of 100 mg acid-treated carbon black (Ketjenblack EC 300) and 2.5 g $FeCl_3$ was added into the monomer solution dropwise under vigorous stirring. The in-situ polymerization of polyrhodanine (PRh) was performed at 70-80 ^{o}C for 12 h and quenched by cooling down to room temperature. Another 36 h of stirring at room temperature is needed for the suspension before it was evaporated overnight at 80^{o}C. The obtained gray-purple powder (FePRh) was ground and charged in a tube furnace followed by pyrolysis at 950^{o}C for 1h under Ar atmosphere. The resulting powder (FePRh-HT1) was subsequently leached in 0.5 M H_2SO_4 for 8 hours followed by filtration and drying in a vacuum oven overnight, named after FePRh-AL. The second pyrolysis at 950 ^{o}C for 3 hours was performed to obtain final N, S-co-doped Fe-N-C catalyst (FePRh-HT2). For comparison, PPy-derived Fe-N-C catalysts were synthesized similar to PRh except for one difference during the polymerization. PPy was synthesized via the in-situ polymerization of pyrrole (0.572 mL, 8.25 mmol) onto 100

mg acid-treated carbon black (Ketjenblack EC 300) with 2.5 g $FeCl_3$ in 100mL cold DDI water in the ice bath for 12h. The rest of the steps were the same in order to obtain the normal Fe-N-C catalyst (FePPy-HT2). The associated precursors and intermediates after first pyrolysis and acid-leaching are named after FePPy, FePPy-HT1, FePPy-AL respectively.

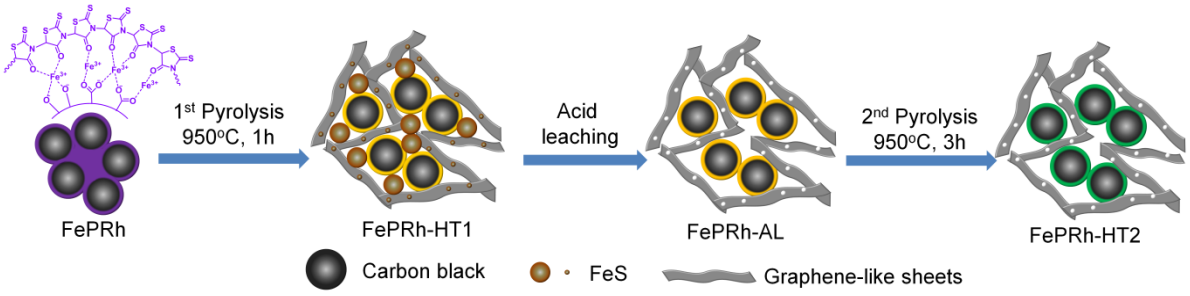

Figure 3- 1 Schematic of the synthesis procedure of PRh-derived Fe-N-C catalyst

3.2.2 Electrochemical characterizations

The electrochemical measurements were conducted with the conventional three-electrode system - catalyst coated glassy carbon electrode (GCE), Ag/AgCl and graphite rod functioned as working, reference and counter electrodes, respectively. The typical catalyst ink consisted of 10 mg Fe-N-C catalyst, 750 µL 1-propanol (1-PA) and 250 µL 0.25% Nafion ethanol solution. After being sonicated for 1 hour, 16 µL of the homogeneous ink was deposited on the GCE to reach a catalyst loading of 0.8 mg cm^{-2}. All the electrochemical experiments were performed on a computer-controlled bipotentiostat (Model AFCBP-1, Pine Instrument Company, USA) at room temperature and potentials were afterward converted to RHE scale for the sake of comparison. ORR activities of Fe-N-C catalysts were investigated via steady-state polarization curves that were obtained by linear staircase voltammetry (LSCV) with potential steps of 30 mV and wait-periods of 30 s

in the O_2 saturated 0.5 M H_2SO_4. The selectivity of water over peroxide for Fe-N-C catalysts can be accessed according to the equations 2-11 and 2-12 on the basis of disk and ring current density recorded in the rotating ring-disk electrode (RRDE) tests: Accelerated degradation tests (ADTs) were applied to evaluate the stability of Fe-N-C catalysts, which involves recording ORR polarization curves (LSCV) after cycling electrode at a rate of 50 mV s^{-1} from 0.6 to 1.0 V *vs* RHE in the N_2 saturated electrolyte for 5000 cycles.

3.2.3 MEA fabrication and fuel cell test

According to the flow chart in Figure 3-2, the MEA (ca. 5 cm^2) fabrication here is a hybrid of CCM and CCG methods. First, Fe-N-C catalysts were mixed with 2-propanol, DDI water, and 5% Nafion ionomer solution in a ratio of 1:12:12:11. Then, after being sonicated for 1 hour, the homogeneous inks were brushed onto one side of the Nafion 211 membrane in order to reach a catalyst loading of ca. 4 mg cm^{-2}. Lastly, commercial carbon paper with microporous layer was used as the gas diffusion layer (GDL, 29 BC, Ion Power) for the cathode. The anode of the MEA, a commercial gas diffusion electrode (GDE), was 20% Pt/C deposited carbon cloth with a Pt loading of 0.2 mg cm^{-2} (Fuel Cell Etc). The GDL, Fe-N-C catalyst coated Nafion 211, and anode GDE were aligned in sequence and placed in a hot-press, undergoing 600 lb load at 120 ℃ for 5 min, to assemble the final MEA. A condition-controlled fuel cell test station (Scribner 850e) was used for the single cell test. The fully humidified H_2 and air flowed into the single cell at a flux of 400 sccm. The polarization curves and power density plots were obtained at 80^{o}C with a back pressure of 20 psig (p_{H_2}= 1.92 bar, p_{O_2}=0.40 bar).

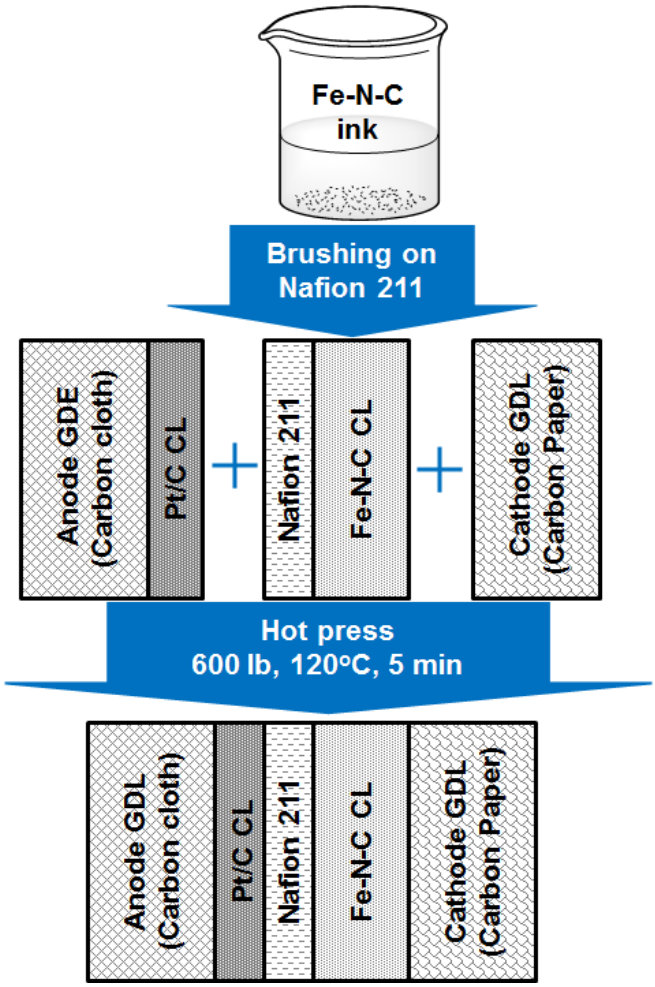

Figure 3- 2 Flow chart of MEA fabrication.

3.2.4 Physical and chemical characterizations

The morphology and microstructure of Fe-N-C catalysts were investigated using field-emission scanning electron microscopy (FESEM, Zeiss ULTRA Plus), transmission electron microscopy (TEM, JEOL 2010F). High-resolution transmission electron microscopy (HR-TEM), scanning transmission electron microscopy (STEM) and energy-dispersive X-ray spectroscopy (EDX) mapping were conducted together with TEM to further identify the elemental distribution and graphitic structure of carbon. X-ray diffraction (XRD) patterns

were acquired using a Rigaku Miniflex 600 (40 kV, 25 mA, Cu Kα radiation λ=1.5406 Å) with a 2θ value ranging from 5 to 80° to analyze the change of iron species and carbon structure after pyrolysis and post-treatment. An Inductively coupled plasma atomic emission spectroscopy (ICP-OES, Leeman, Prodigy) was employed to detect the metallic contents in the final catalyst. A Micromeritics ASAP 2020 analyzer was used to analyze surface area and pore size distribution of the catalysts. The total surface area was estimated according to the Brunauer–Emmett–Teller (BET) equation and the micropore (< 2nm) surface area and external surface area (2~120 nm) were estimated using the t-plot method. X-ray photoelectron spectroscopy (XPS) spectra were recorded on a Thermo Scientific K-Alpha XPS spectrometer equipped with an Al Kα source (1486.6 eV) to analyze the elemental and chemical composition of the surface of Fe-N-C catalysts.

3.2.5 DFT calculation

DFT calculations were carried out using the program BAND. The triple polarization (TZP) basis of Slater-type orbitals (STO) was used. Calculations were performed using PBE-D3 generalized gradient approximation (GGA) for the exchange and correlation energy terms. This functional was chosen because it reliably predicts energetics on graphene systems. In the present study, the doped graphene was modeled using a 6×6 supercell, in which all the atoms were set free to relax. The calculations performed in this study were spin-unrestricted.

In order to evaluate the electrochemical stability of the FeN_4C_{10} active site on S-free and S-doped graphene structure, the cohesive energies (E_{coh}) of Fe in the active site in S-free and S-doped graphene (G) was calculated by the following equation:

$$E_{coh} = -(E_{Fe-G} - E_{Fe} - E_G)$$

where E_{Fe-G} is the total energy of the Fe-bound to the doped graphene structure, E_{Fe} is the energy of an isolated Fe atom and E_G is represent the energy of the optimized doped graphene before Fe insertion. On the basis of fully relaxed structures, the free energy of each intermediate oxygen reaction (ΔG) was calculated to evaluate ORR performance of FeN_4C_{10} active site on S-free and S-doped graphene.

3.3 Results and discussion

3.3.1 Electrochemical performance

In a typical experiment **(Figure 3-1)**, the monomer, rhodanine (Rh) was first initiated by adsorbed Fe^{3+} on the acid-treated carbon black (CB) nanoparticles and then *in-situ* polymerized on the CB nanoparticles.[222-225] The grayish purple powder of PRh-wrapped carbon black composite (FePRh) was obtained after solvent evaporation and grinding. The powder was then heat-treated at 950^{o}C under Ar atmosphere. The obtained sample (FePRh-HT1) underwent a post-treatment of acid-leaching and a second heat-treatment at the same pyrolysis temperature to acquire the final catalyst, FePRh-HT2. For comparison, a Fe-N-C catalyst derived from polypyrrole (PPy) was prepared using the similar method. [226] PPy was used because it is a polymer with a similar repeating unit of one nitrogen atom in a five-membered ring structure serving as a sulfur-free nitrogen precursor. The PPy-derived catalyst after the first heat-treatment and the second heat-treatment are labeled as FePPy-HT1 and FePPy-HT2, respectively.

ORR activities of Fe-N-C catalysts derived from FePRh or FePPy after the second pyrolysis were tested and their polarization curves are depicted in the **Figure 3-3a**. FePRh-

HT2 demonstrates decent ORR activity, with an onset potential (E_{onset}), a half-wave potential ($E_{1/2}$) and limiting current density (i_L) of 0.94V *vs* RHE, 0.77V *vs* RHE, and 4.36 mA cm^{-2}, respectively. In contrast, as summarized in **Table 3-1**, FePPy-HT2 shows much lower activity, giving $E_{on\text{-}set}$, $E_{1/2,}$ and i_L values of 0.88V *vs* RHE, 0.68V *vs* RHE and 3.99 mA cm^{-2}, respectively. The approximately 60 mV higher onset potential of FePRh-HT2 over FePPy-HT2 reveals the faster kinetics for ORR of FePRh-HT2. The approximate 90 mV anodic shift of the half-wave potential for FePRh-HT2 indicates an improved mass transport of reactants, products, and intermediates in FePRh-HT2. The corresponding Tafel plots are displayed in **Figure 3-4** where a lower Tafel slope was observed in FePRh-HT2 (70 mV dec^{-1}) than for FePPy-HT2 (79 mV dec^{-1}). The difference in the Tafel slopes of these two catalysts indicates the different chemical nature of ORR active sites with and without S-doping.

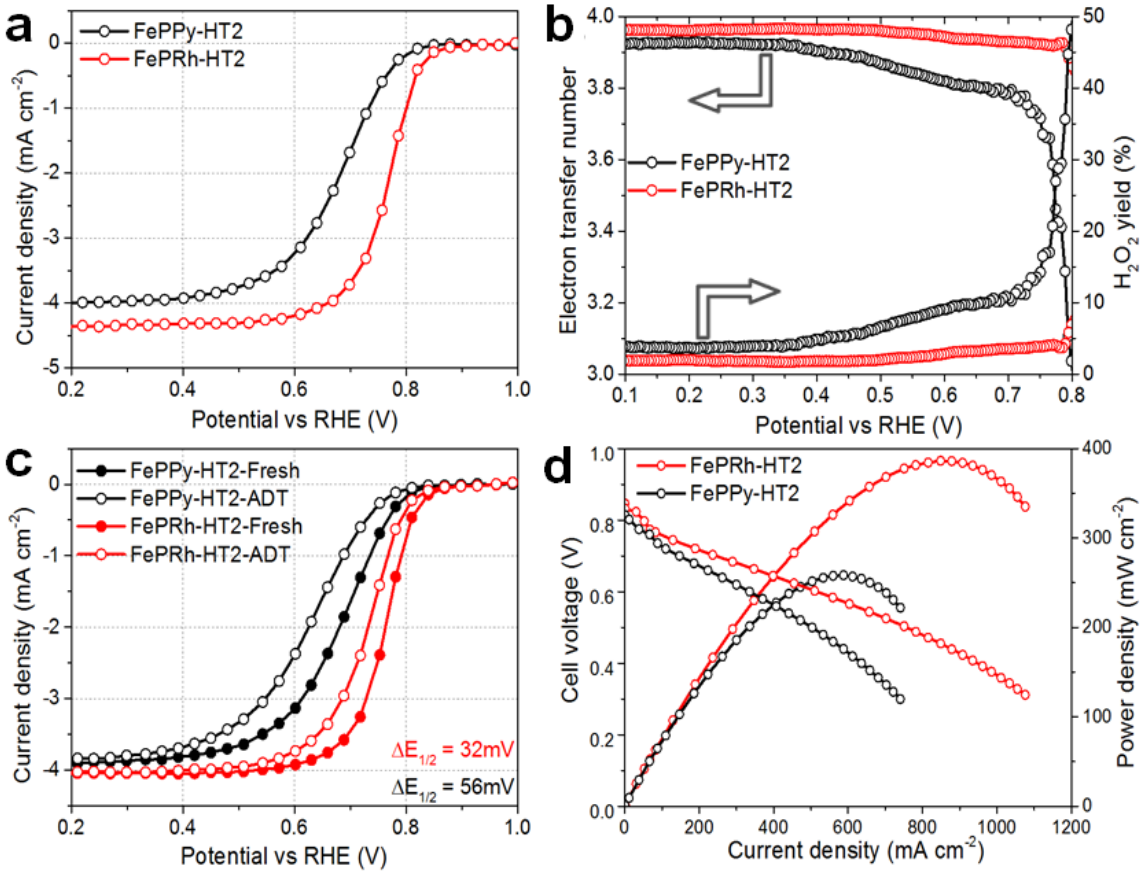

Figure 3- 3 (a) LSV curves and (b) plots of H_2O_2 yield and number of transferred electrons of FePRh-HT2 and FePPy-HT2 coated on a GCE at the rotation of 900 rpm in O_2 saturated 0.5M H_2SO_4 aqueous solution. (c) LSV curves obtained before and after 5000 cycles ranging from 0.6 to 1.0 V vs. RHE in N_2 saturated 0.5M H_2SO_4 aqueous solution. (d) H_2/air PEMFC polarization curves and corresponding power density plots obtained from the MEAs employing FePRh-HT2 or FePPy-HT2 as the cathode catalyst (4 mg cm^{-2}), Pt/C (20 wt.%, JM) as the anode catalyst (0.2 mg_{Pt} cm^{-2}) and Nafion 211 as the solid electrolyte tested at 80°C under 100% relative humidity and back pressure of 20 psig (0.40 bar O_2) with 400 sccm of both hydrogen and air.

Table 3- 1 Comparison of ORR activity of FePRh-HT2 and FePPy-HT2

Sample	$E_{on\text{-}set}$/V	$E_{1/2}$/V	i_L/ mA cm^{-2}	Tafel slope/ mV dec^{-1}	MSD/10^{19} sites g^{-1}	MA (0.8V)/ A g^{-1}	TOF(0.8V)/ e s^{-1} site $^{-1}$
FePRh-HT2	0.94	0.77	4.36	70	4.203	1.660	0.246
FePPy-HT2	0.88	0.68	3.99	79	3.329	0.228	0.043

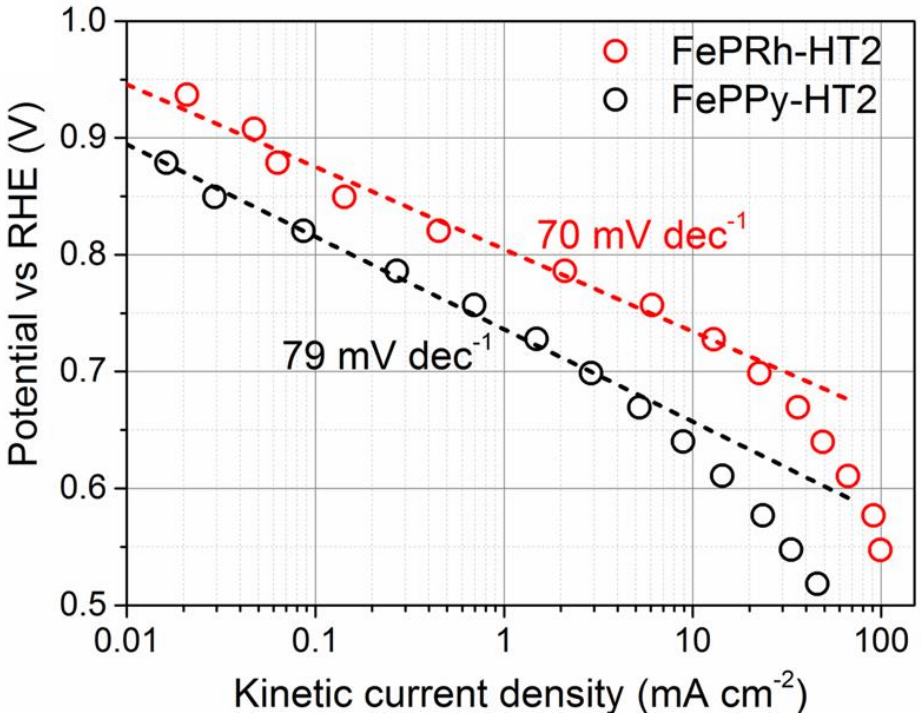

Figure 3- 4 Tafel plots of FePRh-HT2 and FePPy-HT2.

For the H_2O_2 yield measured for S-doped Fe-N-C catalysts, FePRh-HT2 shows below 2.8% yield over the potential range of 0.1 - 0.6 V *vs* RHE, which is consistent with the quasi-four-electron reduction (n>3.94) of oxygen into water over this potential range (**Figure 3-3b**). By comparison, FePPy-HT2 generates large amounts of intermediates during the ORR, yielding more than 3.7% H_2O_2 over the range of 0.1 – 0.6 V *vs* RHE, which implies the two-electron reduction of oxygen into peroxide becomes dominant for FePPy-

HT2. Thus, the RRDE results suggest that the introduction of S-doping from the precursor greatly enhances the selectivity of the catalyst for ORR through the four-electron pathway.

The durability of both FePRh-HT2 and FePPy-HT2 was evaluated by an ADT, i.e. cycling the potential between 0.6 - 1.0 V *vs* RHE for 5000 cycles. The obtained LSV curves after ADTs were analyzed and compared in the **Figure 3-3c**. Clearly, degradation occurs in both Fe-N-C catalysts in terms of down-shift of $E_{1/2}$. The S-doped catalyst (FePRh-HT2) displays less degradation after 5000 cycles (32 mV) as opposed to that of FePPy-HT2 (56 mV). The improved durability of FePRh-HT2 could be benefitted from the high selectivity towards four-electron pathway as the active sites are subjected to fewer attacks from peroxide intermediates. Besides, the potential comprehensive effects of sulfur on the active sites can contribute to the enhancement of durability too. H_2-air PEMFC tests were also carried out to further evaluate the performance of FePRh-HT2 and FePPy-HT2 under real operating conditions. As illustrated in **Figure 3-3d**, when FePRh-HT2 is applied as the cathode catalyst in the H_2-air PEMFC, the cell generates 52 mA cm^{-2} at 0.8 V and 1076 mA cm^{-2} at 0.3 V. Its maximum power density (P_{max}) reaches 386 mW cm^{-2} at 0.46 V, which is one of the highest P_{max} reported for Fe-N-C catalysts in a H_2-air PEMFC. The MEA prepared with the FePPy-HT2 coated cathode could only provide 11 mA cm^{-2} at 0.8 V, 740 mA cm^{-2} at 0.3 V and a P_{max} of 258 mW cm^{-2} at 0.34 V. The superior performances of FePRh-HT2 to that of FePPy-HT2 in the H_2-air PEMFCs strongly confirms the improved ORR activity of the Fe-N-C catalyst by the introduction of sulfur in the precursors.

3.3.2 Effects of sulfur on the formation of active sites

To understand the effects of sulfur on the active sites of NPMCs, it is necessary to investigate the formation of the active sites during synthesis. XRD patterns of FePRh and FePPy at the different steps of the synthesis were obtained to discover the synthesis chemistry of the catalysts (**Figure 3-5**). Ferrous chloride dihydrate ($FeCl_2$•$2H_2O$), the reduction product of the initiator for polymerization ($FeCl_3$), was found to be the main iron species in the composites of both FePRh and FePPy before the pyrolysis (**Figure 3-5a**). However, the products after the first pyrolysis (FePRh-HT1 & FePPy-HT1) differ from each other. The amount of iron precursor is designed to complete the polymerization of the monomer and is present in excess quantities for active sites in the Fe-N-C catalyst.[227] Consequently, most iron from the precursor tends to aggregate together, forming nanoparticles of different iron species during pyrolysis, which serve as sacrificial templates for Fe-N-C catalysts after post-treatment and the second pyrolysis.[16, 70, 73] The XRD pattern in **Figure 3-5b** and HDDAF-STEM image with EDX mapping in **Figure 3-6** reveal more information regarding the nature of the iron species. For PRh, $FeCl_2$•$2H_2O$ is mainly converted into thermodynamically stable iron species, ferrous sulfide (FeS), while $FeCl_2$•$2H_2O$ tends to be reduced into elemental iron (Fe) or iron carbide (Fe_3C) for FePPy-HT1 which is identified clearly in the XRD pattern (**Figure 3-5b**) and HDDAF-STEM image with EDX mapping (**Figure 3-7**). The difference lies in the reducing atmosphere created by the decomposition of polymer precursors. In other words, PRh generates S-contained reducing atmosphere (eg. H_2, C_xH_y, NH_3, H_2S, S) while PPy produces S-free reducing atmosphere (eg. H_2, C_xH_y, NH_3.) during the first pyrolysis. Then, on the basis of

literature,[67] it is possible that $FeCl_2 \cdot 2H_2O$ could undergo following different reactions those two different atmospheres.

$$FeCl_2 \cdot 2H_2O\ (s) \rightarrow FeCl_2\ (s) + 2\ H_2O\ (g) \quad (3\text{-}1)$$

$$FeCl_2\ (s) + H_2(g) \rightarrow Fe\ (s) + 2\ HCl\ (g) \quad (3\text{-}2)$$

$$y\ FeCl_2\ (s) + 2\ C_xH_y(g) \rightarrow y\ Fe\ (s) + 2x\ C\ (s) + 2y\ HCl\ (g) \quad (3\text{-}3)$$

$$3\ FeCl_2\ (s) + 2\ NH_3\ (g) \rightarrow 3Fe\ (s) + N_2\ (g) + 6\ HCl\ (g) \quad (3\text{-}4)$$

$$3\ Fe\ (s) + C\ (s) \rightarrow Fe_3C\ (s) \quad (3\text{-}5)$$

$$Fe\ (s) + H_2S\ (g) \rightarrow FeS\ (s) + H_2\ (g) \quad (3\text{-}6)$$

$$Fe\ (s) + S\ (g) \rightarrow FeS\ (s) \quad (3\text{-}7)$$

$$FeCl_2\ (s) + H_2S\ (g) \rightarrow FeS\ (s) + 2\ HCl\ (g) \quad (3\text{-}8)$$

Firstly, the hydrated water was released and the anhydrous $FeCl_2$ formed (Equation 3-1), which was further reduced into metallic iron by the gases such as H_2, C_xH_y, NH_3 (Equation 3-(2-4)).[73] Then the metallic iron tends to react with carbon to form Fe_3C when the temperature was higher than 650^{o}C in the absence of sulfur in the atmosphere (Equation 3-5) for FePPy.[67, 228] However, for the pyrolysis of PRh, H_2S and sulfur in the atmosphere would react with metallic iron to form FeS (Equation 3-6 & 7). Also, $FeCl_2$ could directly react with H_2S to generate FeS (Equation 3-8). Then, thermodynamically stable FeS prohibited the reaction of metallic iron and carbon to form Fe_3C (Equation 3-9) at high pyrolysis temperature.[67]

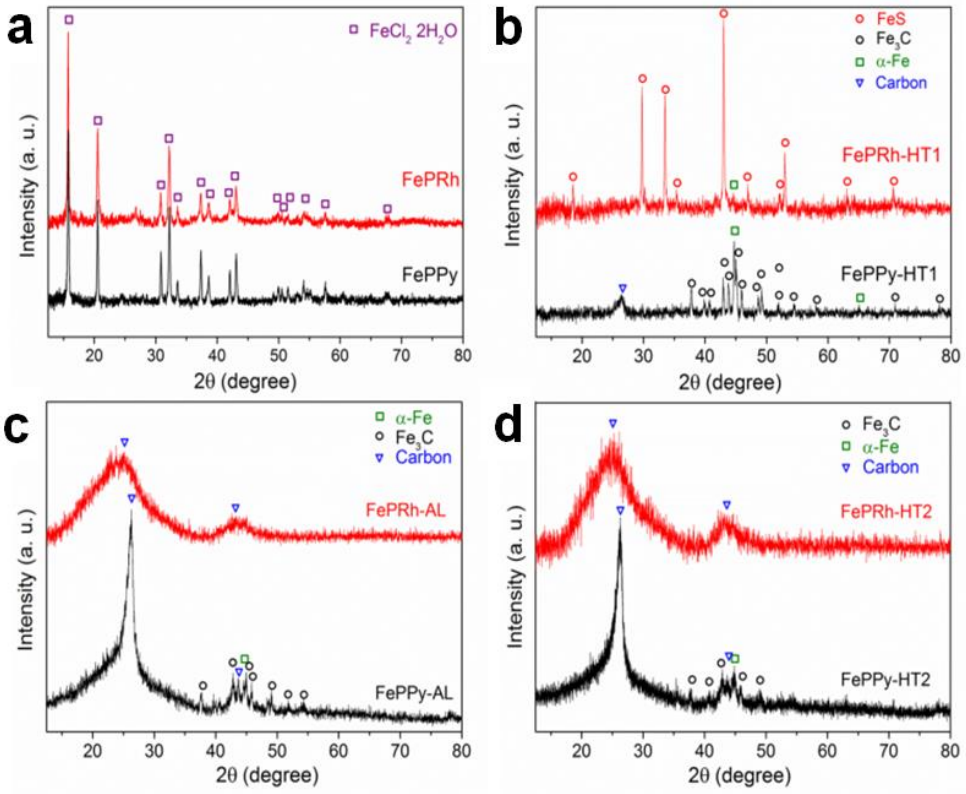

Figure 3- 5 XRD patterns for both FePRh and FePPy (a) before pyrolysis, (b) after the first pyrolysis (HT1), (c) after acid-leaching (AL) and (d) the second pyrolysis (HT2).

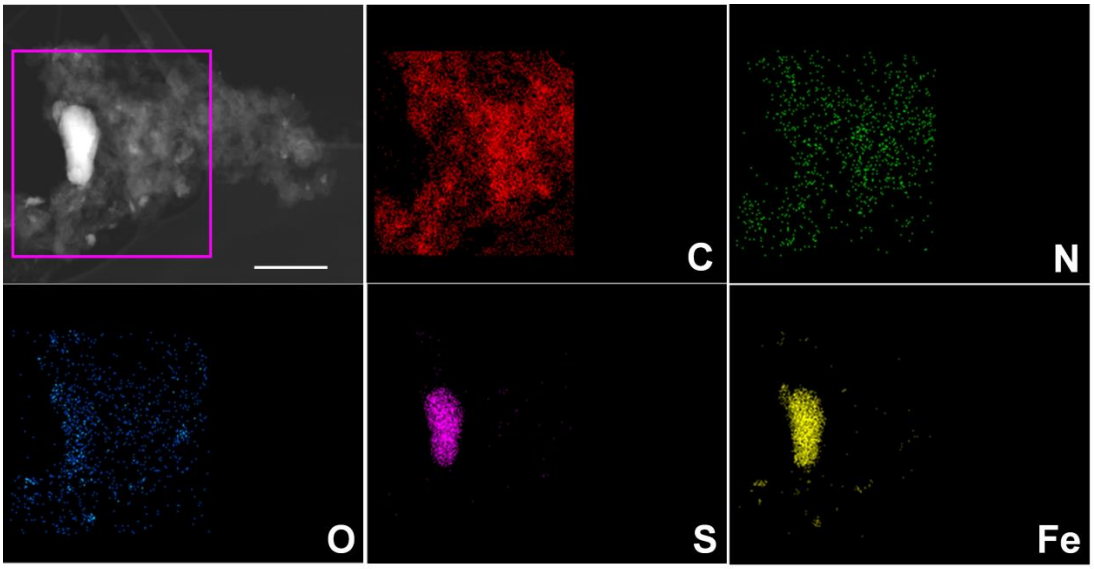

Figure 3- 6 HAADF-STEM and EDX mapping of FePRh-HT1, Scale bars: 500 nm.

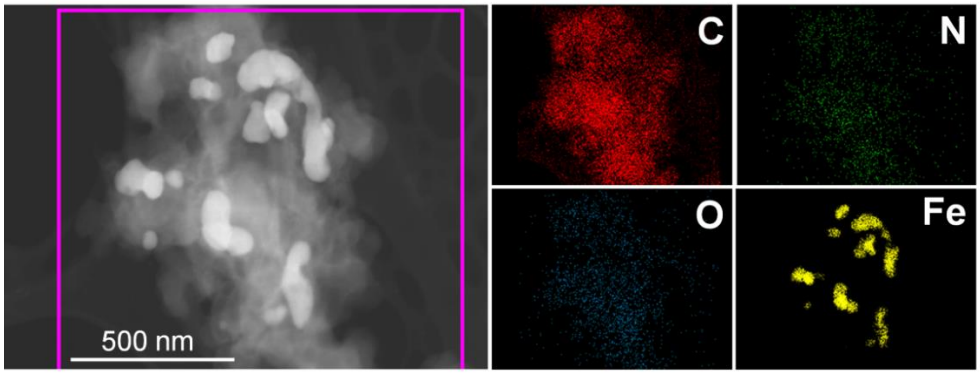

Figure 3- 7 HAADF-STEM and EDX mapping of FePPy-HT1, Scale bars: 500 nm.

According to the XRD patterns of FePRh-AL and FePPy-AL in **Figure 3-5c**, FeS nanoparticles are near-completely removed while some Fe/Fe_3C nanoparticles still remain after acid-leaching, indicating the higher solubility of FeS in the acid as opposed to that of Fe/Fe_3C. According to the XRD patterns in **Figure 3-5d**, the undissolved Fe/Fe_3C nanoparticles remain in the final catalyst (FePPy-HT2) after the second pyrolysis. HAADF-STEM images with EDX provide the visual evidence of the absence of iron species agglomeration in FePRh-HT2 (**Figure 3-8**) and quite a few Fe/Fe_3C nanoparticles (50 – 100) nm in size embedded in the carbon structure (**Figure 3-9**).

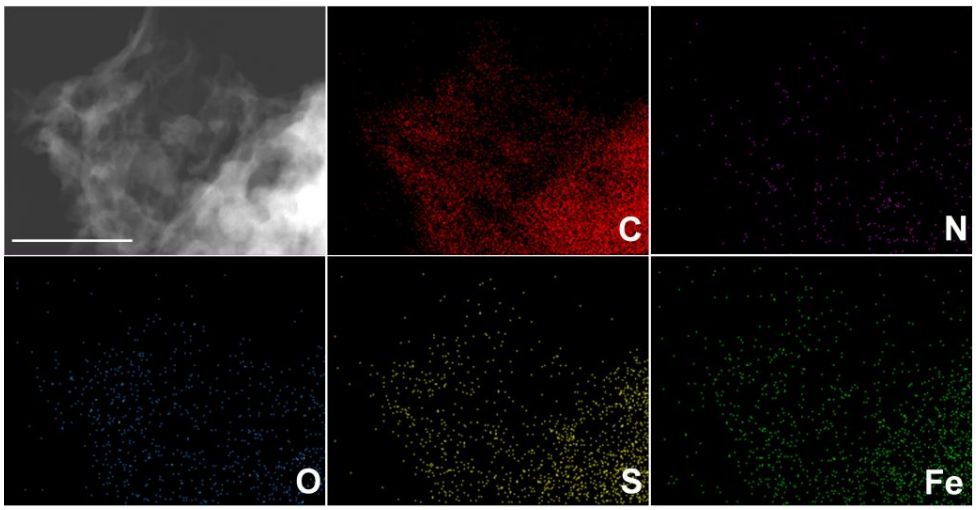

Figure 3- 8 HAADF-STEM and EDX mapping of FePRh-HT2, Scale bars: 200 nm.

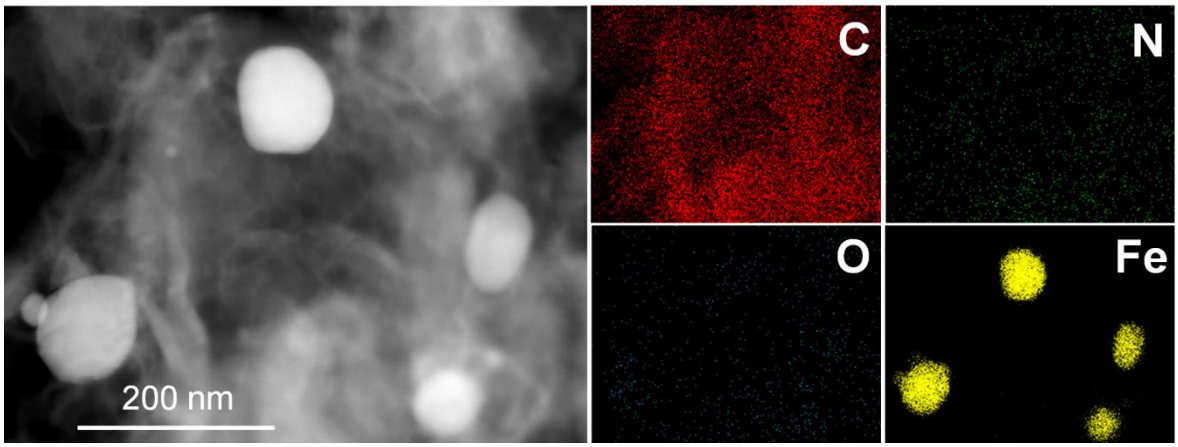

Figure 3- 9HAADF-STEM and EDX mapping of FePRh-HT2, Scale bars: 200 nm.

The residual of Fe/Fe_3C leads to more iron existed in FePPy-HT2 than that in FePRh-HT2 (2.40 wt.% vs. 1.47 wt.%) as obtained from inductively coupled plasma optical emission spectrometry (ICP-OES) in **Table 3-2.** The surface chemical composition based on XPS analysis discloses that almost all the iron is exposed at the surface in FePRh-HT2 whilst only about half amount of the iron is exposed at the surface of FePPy-HT2 (**Table 3-2**). In the high-resolution Fe 2p XPS spectra (**Figure 3-10a**), the appearance of characteristic peaks for iron carbide at 708.1 eV ($2p_{3/2}$) and 721.7 eV ($2p_{1/2}$) in the spectrum of FePPy-HT2 implies the existence of Fe_3C at the surface of FePPy-HT2 too. This can further lower the relative amount of other iron species, including Fe-N_x active sites in FePPy-HT2.

Table 3- 2 Iron contents in FePRh-HT2 and FePPy-HT2

Sample	ICP-OES	XPS Survey	
	Weight percentage	Atomic percentage	Weight percentage
FePRh-HT2	1.47	0.34	1.49
FePPy-HT2	2.40	0.28	1.27

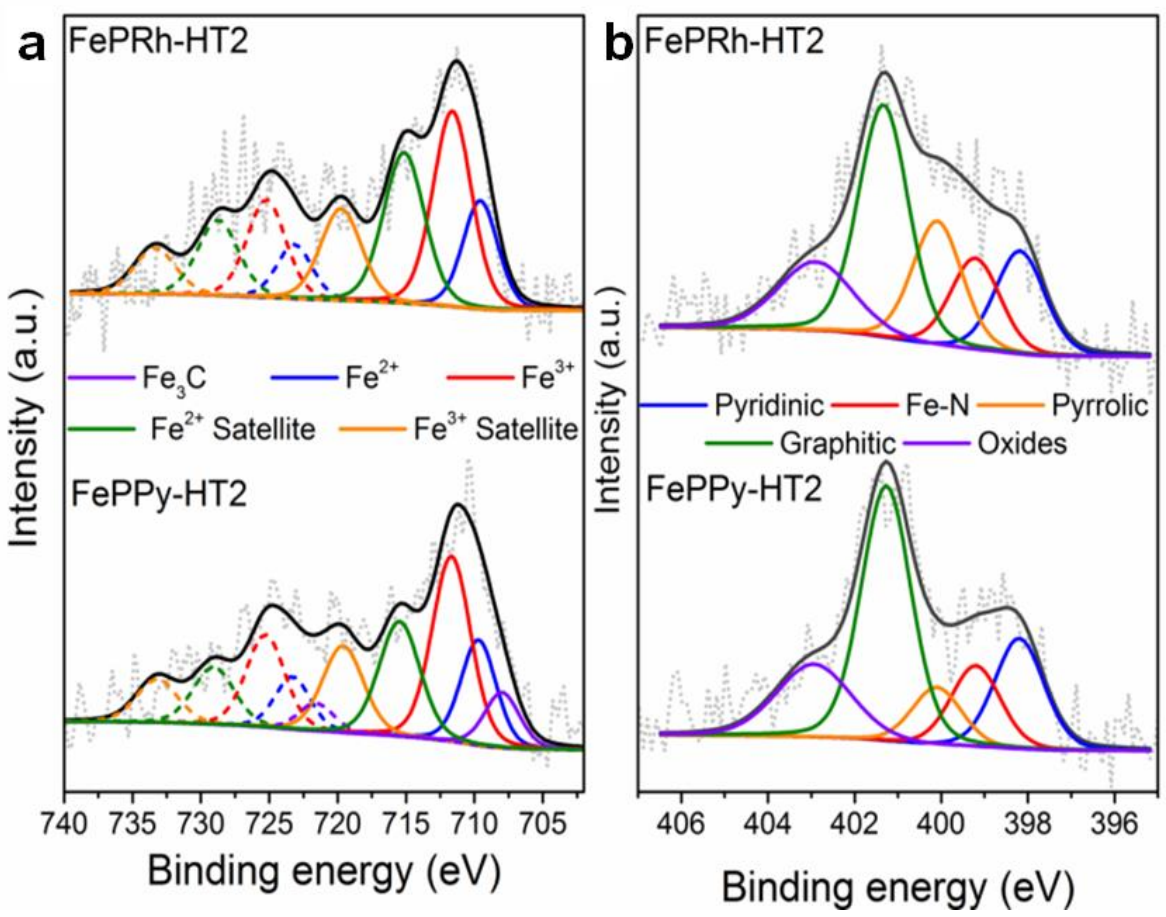

Figure 3- 10 High-resolution XPS spectra of (a) Fe 2p and (b) N 1s for FePRh-HT2 and FePPy-HT2.

Another function of the intermediate iron species, especially the Fe_3C/Fe nanoparticles, is to catalyze the graphitization reaction of carbon.[67] Although the graphitic carbon can enhance the electron conductivity and chemical resistivity of the catalyst and hence increase its activity and stability, excessive amounts of Fe_3C/Fe nanoparticles can damage the Fe-N_x active sites during the graphitization at high temperature.[67] In comparison with the sharp carbon peak at 26.24^o appeared in the XRD pattern of FePPy-AL in **Figure 3-5c,** the broad carbon peak at 25.02^o in the XRD pattern of FePRh-AL shows the insignificant catalytic activity towards graphitization reaction of the excessive FeS nanoparticles formed in FePRh-

HT1. Therefore, the introduction of sulfur can potentially prevent the unexpected loss of Fe-N_x active sites mainly at the first pyrolysis due to excess Fe_3C/Fe nanoparticles and indirectly increase active sites density.

In order to compare the active site density of these two catalysts, high-resolution N 1s XPS spectra were acquired to distinguish Fe-N bonding (~399 eV) from other N species, namely pyridinic (~398 eV), pyrrolic (~400 eV), graphitic (~401 eV) and oxides (> 402 eV).[72] As depicted in the **Figure 3-10b**, the atomic ratios of Fe-N to total nitrogen for both samples are similar to each other, giving 14.9% and 13.2% for FePRh-HT2 and FePPy-HT2 respectively. Since the total nitrogen content in FePRh-HT2 is higher than that in FePPy-HT2 (2.38 vs 2.07 at.%) in **Figure 3-11**, the nitrogen assigned for the Fe-N bond in FePRh-HT2 is slightly higher than that in FePPy-HT2 (0.35 *vs.* 0.27 at.%). This indicates that more active sites may exist in FePRh-HT2 than in FePPy-HT2.

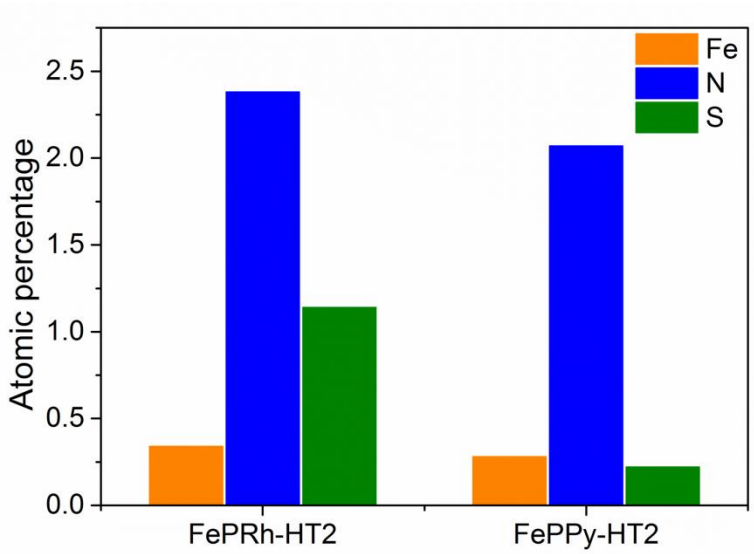

Figure 3- 11 Atomic percentage of different elements, Fe, N, S of FePRh-HT2 and FePPy-HT2 obtained from XPS surveys.

The Fe-N_x active sites of Fe-N-C catalysts in acidic media can be (i) located at the defects on the basal plane of the graphene sheet bearing the typical FeN_4C_{10} moiety[48] or (ii) in the bridge between two graphene sheets at the armchair edges showing the structure of $FeN_{2+2}C_{4+4}$[17] or (iii) held at either disordered graphene sheets or zigzag graphene edges with the typical porphyrinic moiety FeN_4C_{12}.[47] No matter which kinds of active sites exist in Fe-N-C catalysts, four nitrogen atoms coordinated with one iron ion (Fe-N_4) is still the dominant stoichiometry in the active sites. Thus, we assume all the nitrogen atoms assigned to Fe-N are used to form Fe-N_4 active sites, giving the atomic percentages of Fe-N_4 active sites, 0.089 at.% and 0.068 at.% for FePRh-HT2 and FePPy-HT2 respectively. On the basis of the elemental analysis from the XPS survey, the mass-based active sites density (MSD, site g^{-1}) can be calculated. As presented in **Table 3-2**, the MSD for FePRh-HT2 and FePPy-HT2 are 4.203×10^{19} site g^{-1} and 3.329×10^{19} site g^{-1}, respectively.

3.3.3 Effects of sulfur on the accessibility of active sites

Although the total MSD of FePRh-HT2 and FePPy-HT2 are similar, the accessible active site density can be different due to the difference in morphology and surface area. Highly-porous structures and high surface areas can facilitate the mass transport of oxygen, intermediates, and products on to or away from the active sites and hence increase ORR activity. The difference of morphology due to the introduction of sulfur becomes clear after the first pyrolysis. Instead of having a morphology similar to that of FePPy-HT1 – having a large amount of Fe/Fe_3C particles agglomerate with carbon black and closely-wrapped in graphitic carbon layers (**Figure 3-12 a-c**) – FePRh-HT1 already forms typical sheet-like structures together with agglomerated carbon black and metallic nanoparticles (**Figure 3-12**

d,e).[16, 70, 72] The carbon sheets were found to be strip-like, highly porous and non-graphitic **(Figure 3-12f**), which is in agreement with its XRD pattern.

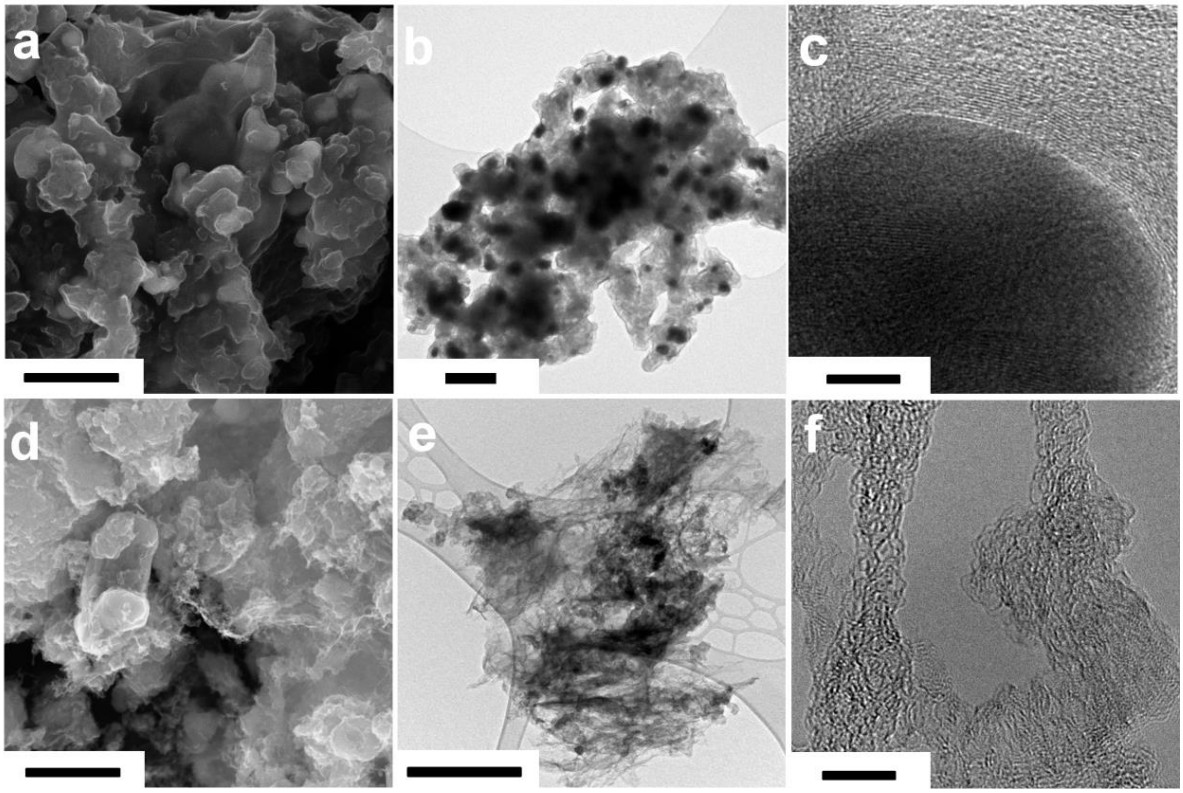

Figure 3- 12 Morphology of samples after the first pyrolysis. Scanning electron microscopy (SEM), transmission electron microscopy (TEM) and high-resolution-TEM (HR-TEM) images of (a, b, c) FePPy-HT1 and (d, e, f) FePRh-HT1, respectively. Scale bars: (a, d) 1 μm, (b, e) 500 nm and (c, f) 5 nm.

After the acid-leaching and second pyrolysis, FePRh-HT2 consists of the typical sheet-wrapped carbon black structure as seen in both SEM and TEM (**Figure 3-13 a-c**).[70, 72] Specifically, it can be seen from the SEM images that strips of carbon sheets cross with each other and are loosely-packed and wrapped on the surface of carbon black agglomerates. The micrometer-scale porous structure may originate from outgassing during the decomposition

of the precursor as well as during the removal of large FeS particles by acid-leaching. At the same time, mesopores (20 - 50 nm) that are formed from the leaching out of small FeS nanoparticles can also be observed in the **Figure 3-13b**. As for FePPy-HT2, the graphene-like nanosheets were still closely wrapped on carbon black agglomerates (**Figure 3-13d**) and the sheet-like structures are found to be continuous and non-porous in the typical onion ring or wrinkle structure (**Figure 3-13e**).[16, 74, 95] Therefore, the existence of sulfur facilitates the formation of porous carbon structures during the synthesis of the Fe-N-C catalyst through the significant outgassing and template effect of FeS, which can enhance the mass transport towards active sites.

Moreover, it is clear that the carbon nanosheets in FePRh-HT2 are much less stacked than in FePPy-HT2 which clearly has a stacking of about 20 layers of graphene in the HR-TEM (**Figure 3-13 c,f**). According to the XRD results in **Table 3-3**, the interlayer spacing *(d_{002})* of graphene layers in the FePRh-HT2 is larger than that of FePPy-HT2 (0.35 nm *vs.* 0.34 nm) while stacking crystal size in the *c*-direction (*Lc*) of FePRh-HT2 is much smaller than that of FePPy-HT2 (1.02 nm *vs.* 7.99 nm), resulting in fewer number of stacked graphene layers in the FePRh-HT2 (2.9 *vs.* 23.6). Therefore, the extra S-doping is likely to hinder the stacking of graphene layers and generate few-layer graphene structures in FePRh-HT2, which enhances the surface area and exposes more active sites to reactants, intermediates, and products of ORR.

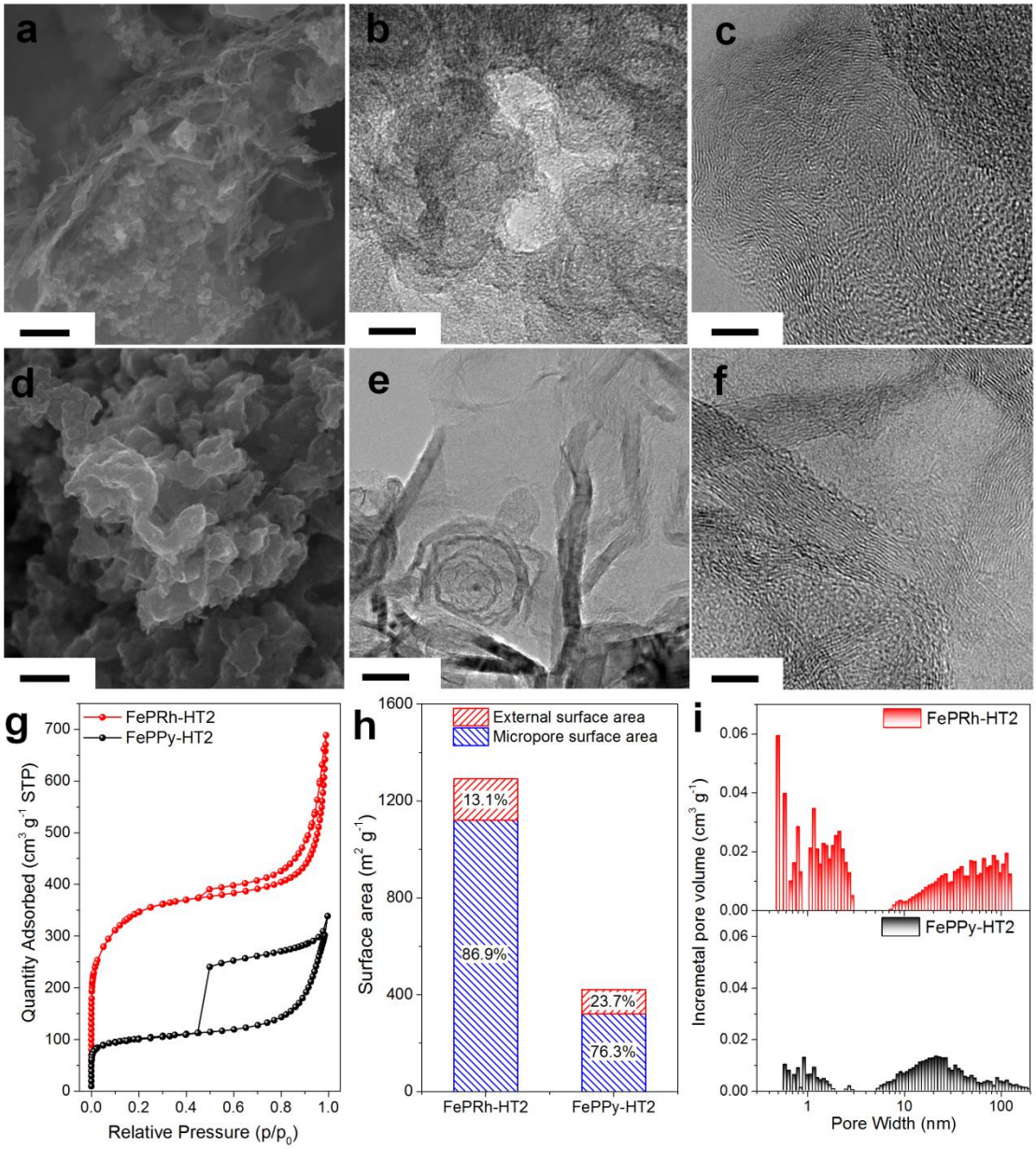

Figure 3- 13 Morphology of catalysts. Scanning electron microscopy (SEM), transmission electron microscopy (TEM) and high-resolution-TEM (HR-TEM) images of (a, b, c) FePRh-HT2 and (d, e, f) FePPy-HT2, respectively, (g) N_2 adsorption-desorption isotherms of FePRh-HT2 and FePPy-HT2 and corresponding (h) BET surface area and (i) pore size distribution. Scale bars: (a, d) 500 nm, (b, e) 20 nm and (c, f) 5 nm.

Table 3- 3 Summary of parameters deduced from XRD data for FePRh-HT2 and FePPy-HT2

Sample	$2\theta/^{o}$	FWHM/cm^{-1}	d spacing/nm	*Lc*/nm	No. of layers
FePRh-HT2	25.16	7.879	0.35	1.02	2.9
FePPy-HT2	26.33	1.010	0.34	7.99	23.6

To further confirm the effects of S on the morphology, nitrogen adsorption-desorption experiments were conducted on both FePRh-HT2 and FePPy-HT2. From the N_2 adsorption-desorption isotherms (**Figure 3-13g**), FePRh–HT2 shows the characteristic adsorption under low relative pressure for micropores while FePPy-HT2 shows typical hysteresis loop for mesopores. The corresponding BET surface area of FePRh-HT2 is 1291 m^2 g^{-1}, which is three times higher than that of FePPy-HT2 **(Figure 3-13h).** Micropore surface area of FePRh-HT2 is not only three times higher than that of FePPy-HT2 (1121 m^2 g^{-1} *vs.* 321 m^2 g^{-1}), but also it accounts for more in the total measured surface area as opposed to that of FePPy-HT2 (86.9% vs 76.3%). Furthermore, the pore size distribution in **Figure 3-13i** also confirms the larger portion of micropores in FePRh-HT2 than that in FePPy-HT2, indicating the introduction of sulfur benefits the formation of micropores. As micropores are generally considered as the platform for holding the active sites,[47, 229] high accessible active site density can contribute to the high ORR activity of FePRh-HT2. Besides, in comparison with FePPy-HT2, there are more and larger mesopores and macropores in FePRh-HT2, which matches with its high external surface area (169 m^2 g^{-1} *vs.* 100 m^2 g^{-1}) and the loosely-packed carbon structure (**Figure 3-13a**). The meso/macro-porous structure of FePRh-HT2

could enhance the mass transport of reactants, intermediates, and products, further improving the ORR activity of FePRh-HT2.

3.3.4 Doping effect of sulfur on active sites

It was reported that sulfur mainly demonstrates a positive effect on ORR activity of NPMC indirectly. Here, the indirect effects of sulfur on MSD and BET surface area (representing the accessibility of active sites) could be quantified via Tafel equation and cross-checked with obtained experimental overpotential.

Tafel Equation is as follows:

$$\eta = A \log \left(\frac{i_k}{i_0}\right) \quad (3\text{-}10)$$

where η is the overpotential, i_k is kinetic current density, i_0 is the exchange current density and A is the Tafel slope obtained from the Tafel plot, which is also determined by

$$A = \frac{2.303\ RT}{\alpha n_o F} \quad (3\text{-}11)$$

where R is the universal gas constant, T is absolute temperature, F is Faraday constant, and α is charge transfer coefficient, n_o is the electron transfer number in the rate-determining step.[201]

According to the Tafel plots in **Figure 3-4**, the Tafel slopes for FePRh-HT2 and FePPy-HT2 are 70 and 79 mV dec^{-1} respectively. Therefore, the overpotentials of the two catalysts can be expressed (in mV) as follows:

$$\eta_{FePRh-HT2} = 70 \log \left(\frac{i_{FePRh-HT2}}{i_{0,\ FePRh\text{-}HT2}}\right) \quad (3\text{-}12)$$

$$\eta_{FePPy-HT2} = 79 \log \left(\frac{i_{FePPy-HT2}}{i_{0,\ FePPy\text{-}HT2}}\right) \quad (3\text{-}13)$$

At the on-set potential, the current density of both catalysts can be set as follows:

$$i_{FePRh\text{-}HT2} = i_{FePPy\text{-}HT2} = I \tag{3-14}$$

Differences in MSD and BET surface area of these two catalysts can lead to differences in exchange current density. If MSD is the sole reason responsible for the difference in overpotential, the exchange current densities should change proportionally.

$$i_{0,\ FePRh\text{-}HT2} = \frac{4.203}{3.329} * i_{0,\ FePPy\text{-}HT2} = 1.26 * i_{0,\ FePPy\text{-}HT2} \tag{3-15}$$

Then the difference in on-set potential can be calculated as follows:

$$\Delta E^{MSD}_{on\text{-}set,\ 1} = \eta_{FePPy\text{-}HT2} - \eta_{FePRh\text{-}HT2} \tag{3-16}$$

$$= 70 \log \left(\frac{i_{FePPy\text{-}HT2}}{i_{0,\ FePPy\text{-}HT2}}\right) - 70 \log \left(\frac{i_{FePRh\text{-}HT2}}{i_{0,\ FePRh\text{-}HT2}}\right) = 70 \log \left(\frac{i_{FePPy\text{-}HT2}}{i_{0,\ FePPy\text{-}HT2}} * \frac{i_{0,\ FePRh\text{-}HT2}}{i_{FePRh\text{-}HT2}}\right)$$

$$= 70 \log \left(\frac{i}{i_{0,\ FePPy\text{-}HT2}} * \frac{1.26 * i_{0,\ FePPy\text{-}HT2}}{i}\right) = 70 \log(1.26) = 7.0\ mV$$

$$\Delta E^{MSD}_{on\text{-}set,\ 2} = \eta_{FePPy\text{-}HT2} - \eta_{FePRh\text{-}HT2} \tag{3-17}$$

$$= 79 \log \left(\frac{i_{FePPy\text{-}HT2}}{i_{0,\ FePPy\text{-}HT2}}\right) - 79 \log \left(\frac{i_{FePRh\text{-}HT2}}{i_{0,\ FePRh\text{-}HT2}}\right) = 79 \log(1.26) = 7.9\ mV$$

Then $\Delta E^{MSD}_{on\text{-}set}$ should be in the range from 7.0 to 7.9 mV, which is 7.5 mV on average.

Likewise, if BET surface area is the solo reason responsible for the overpotential, the exchange current densities should change proportionally, as exchange current density is proportional to surface roughness of catalyst-coated electrode which is also proportional to surface area of catalyst.

$$i_{0,\ FePRh\text{-}HT2} = \frac{1291}{420} * i_{0,\ FePPy\text{-}HT2} = 3.07 * i_{0,\ FePPy\text{-}HT2} \tag{3-18}$$

Then the difference in on-set potential can be calculated as follows:

$$\Delta E^{BET}_{on\text{-}set,\ 1} = \eta_{FePPy\text{-}HT2} - \eta_{FePRh\text{-}HT2} \tag{3-19}$$

$$= 70\ log\ (\frac{i_{FePPy\text{-}HT2}}{i_{0,\ FePPy\text{-}HT2}})\text{-}70\ log\ (\frac{i_{FePRh\text{-}HT2}}{i_{0,\ FePRh\text{-}HT2}}) = 70\ log(3.07) = 34.1\ mV$$

$$\Delta E^{BET}_{on\text{-}set,\ 2} = \eta_{FePPy\text{-}HT2} - \eta_{FePRh\text{-}HT2} \tag{3-20}$$

$$= 79\ log\ (\frac{i_{FePPy\text{-}HT2}}{i_{0,\ FePPy\text{-}HT2}})\text{-}79\ log\ (\frac{i_{FePRh\text{-}HT2}}{i_{0,\ FePRh\text{-}HT2}}) = 79\ log(3.07) = 38.5\ mV$$

Then $\Delta E^{BET}_{on\text{-}set}$ should be in the range of 34.1 to 38.5 mV, which is 36.3 mV on average.

Thus, in total, the calculated on-set potential/overpotential difference caused by BET surface area and MSD ranges from 41.1 to 46.4 mV, which is 43.8 mV on average. It does not match the actual onset potential difference of these two catalysts (60 mV), indicating the indirect positive effect of sulfur on MSD and BET surface area (accessibility of active sites) cannot be the single reason for the improved activity of FePRh-HT2. Therefore, turn-over frequency (TOF) at the potential of 0.80 V vs SHE for both two catalysts were calculated based on mass activity (MA) and MSD, bearing 0.237 e s^{-1} $site^{-1}$ for FePRh-HT2 and 0.038 e s^{-1} $site^{-1}$ for FePPy-HT2 (**Table 3-1**). The enhanced TOF of FePRh-HT2 indicates possible direct effect of extra sulfur doping on the structure of active sites itself.

The atomic ratio nitrogen to sulfur is 2:1 on the basis of XPS survey (**Figure 3-11**) and the dominant sulfur species in FePRh-HT2 is C-S-C as shown in the high-resolution XPS spectra of S 2p (**Figure 3-14)**. Thus, an S-doped model of two sulfur atoms linked as C-S-C in the typical FeN_4C_{10} active site structure was introduced to compare with S-free FeN_4C_{10} active site model in the DFT calculation towards ORR (**Figure 3-15 a,b)**. Due to the size and steric hindrance of the sulfur atoms, some pin-hole defects around doped sulfur atoms are introduced in the S-doped FeN_4C_{10} active site model (**Figure 3-15 b**). Accordingly, **Figure 3-15 c & d** show the changes of free energies in each step of ORR of the S-free and

S-doped FeN_4C_{10} active site model at zero electrode potential (U=0 V *vs* SHE), equilibrium potential (U = 1.23 V *vs* SHE) and the comparative potential (U = 0.80 V *vs* SHE). It shows that, at the equilibrium potential (U = 1.23V vs SHE), the OOH* and O* formation is energetically negative (exothermic) and the other steps are positive (endothermic) for both models, indicating the last two electrons transfer limit the whole ORR. When the same overpotential was applied (U = 0.80 V *vs* SHE), despite that the formation energies of last two steps for both active sites are still positive, the third step of S-doped FeN_4C_{10} active site is nearly thermodynamically-favorable. This finding suggests that the ORR activity of S-doped FeN_4C_{10} active site on graphene is higher than that of S-free one at the potential of 0.80 *vs* SHE, which is in agreement with the high MA and TOF of FePRHh-HT2 in **Table 3-1**.

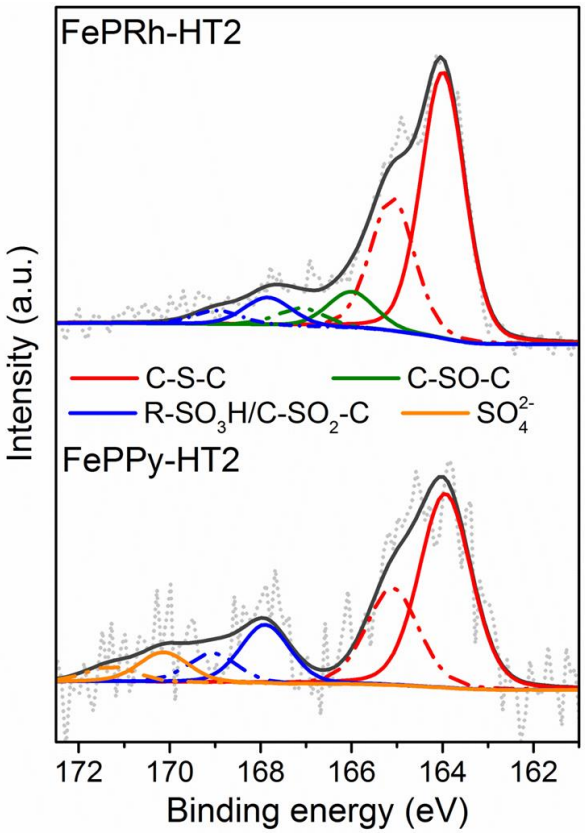

Figure 3- 14 High-resolution XPS spectra of S 2p for FePRh-HT2 and FePPy-HT2.

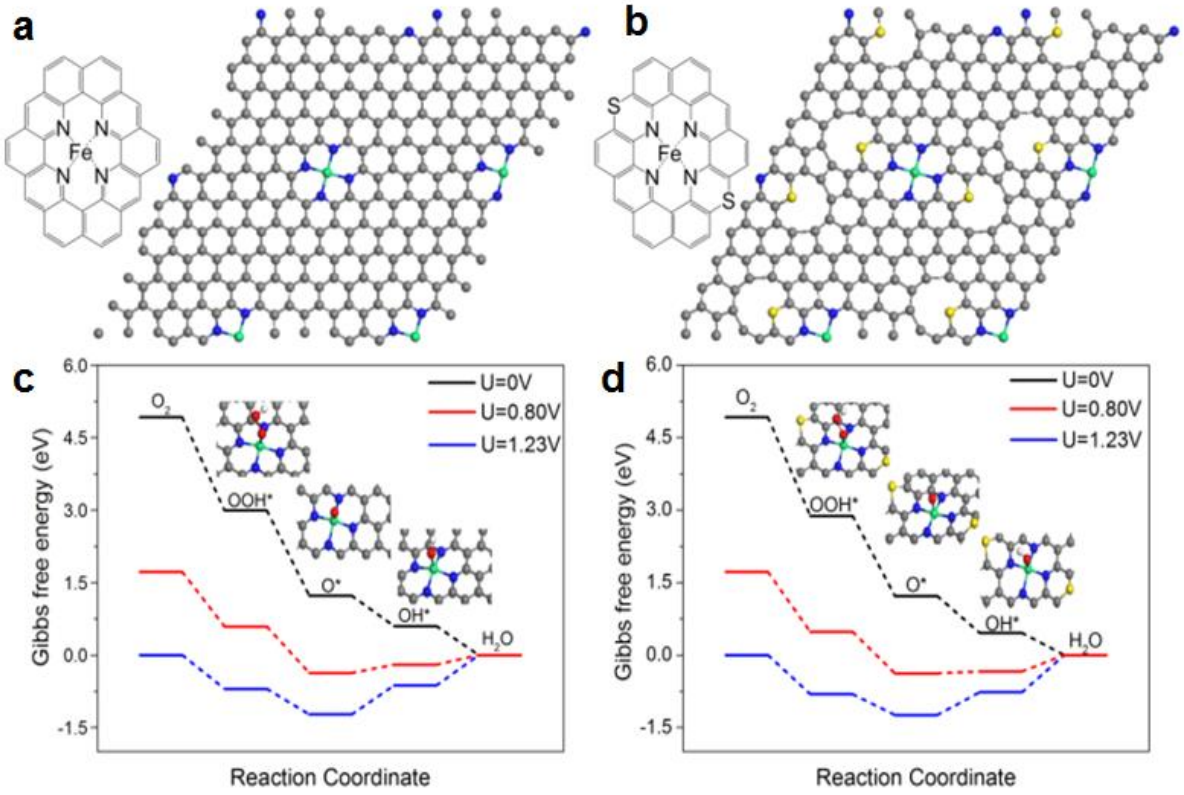

Figure 3- 15 Extended models of (a) S-free and (b) S-doped FeN_4C_{10} active sites on graphene sheets. Corresponding free energy diagrams of intermediates in ORR on (c) S-free and (d) S-doped FeN_4C_{10} active sites on graphene sheets as a function of the electrode potential.

For the S-free FeN_4C_{10} active site, the bonding distances between Fe and adjacent N atoms are found to be 1.89 Å. The Fe-N distances in the S-doped FeN_4C_{10} active site is slightly longer– in the range of 1.92 - 1.94 Å (**Table 3-4**). The cohesive energies ($E_{coh,Fe}$) are 9.00 eV and 8.86 eV for S-free and S-doped FeN_4C_{10} active sites, respectively. These results suggest that S-free FeN_4C_{10} active site is slightly more stable than the S-doped FeN_4C_{10} active site. However, it was reported that the demetallation and a reduction in activity of

doped graphene material can occur in the presence of oxygen.[221, 230] Therefore, the cohesive energies of S-free and S-doped FeN_4C_{10} active sites in the presence of O_2 were calculated. It was found that E_{coh,Fe,O_2} for the S-doped FeN_4C_{10} active site is 10.11eV, which is higher than that of the S-free FeN_4C_{10} active site (9.75 eV). This observation indicates that, in the presence of oxygen reactant, the electrochemical stability of S-doped FeN_4C_{10} active site is improved in comparison with S-free FeN_4C_{10} active site. The enhanced stability of S-doped active site structure is also in agreement with the durability tests of FePRh-HT2 and FePPy-HT2, as well as the DFT results for S-doped iron phthalocyanine (FeSPc) and S-doped graphene as the carbon support for Pt catalysts.[214, 231]

Table 3- 4 Bond lengths between the Fe and N atoms, O_2 adsorption energies, and the cohesive energies of Fe and Fe-O_2 in the investigated S-free and S-doped FeN_4C_{10} active sites.

	Fe-N1 (Å)	Fe-N2 (Å)	Fe-N3 (Å)	Fe-N4 (Å)	E_{ads,O_2} (eV)	$E_{coh,Fe}$ (eV)	E_{coh,Fe,O_2} (eV)
FeN_4C_{10}	1.89	1.89	1.89	1.89	-0.75	9.00	9.75
S-doped FeN_4C_{10}	1.94	1.92	1.94	1.92	-1.25	8.86	10.11

3.4 Conclusions

With the help of different characterization, it is found that sulfur can enhance the ORR activity and durability of a Fe-N-C catalyst through the comprehensive effects on Fe-N_x active sites. Firstly, sulfur can tune the active site density by altering the intermediate from Fe/Fe_3C to FeS, which can reduce the destruction of Fe-N_x active sites by Fe/Fe_3C catalyzed graphitization reaction. Secondly, the introduction of sulfur can increase the

accessibility of active sites by introducing hierarchically porous structure and high surface area. The outgassing from the decomposition of N, S-contained precursor (PRh) and the leaching out of sacrificial FeS nanoparticles in the acid help to construct macro-, meso- and micro-pores. Thirdly, as revealed by DFT calculations, sulfur could dope into the structure of Fe-N_4 active site. The S-doped Fe-N_4 active site demonstrates better electron transfer at 0.8V vs RHE and better stability in the presence of oxygen compared to the S-free Fe-N_4 active site. Therefore, the excellent ORR activity in the half-cell test, the promising performance in the real H_2-air PEMFC as well as the excellent durability of FePRh-HT2 could be explained. Moreover, this discovery suggests new ideas for the rational design and development of highly-active and durable NPMCs, such as introducing sulfur precursor with nitrogen, iron precursors and carbon support.

Chapter 4: Porous Nitrogen-rich Polymer Film Derived Free-standing Metal-free Catalyst for Oxygen Reduction Reaction

This chapter includes content from the following draft in preparation:

G. Jiang, J. Zhang, H. Zarrin, T. Cumberland, J.H. Ahn, D. Higgins, M. Li, M.A. Hoque, P. Zamani, K. Feng, Z. Chen. Porous Nitrogen-rich Polymer Film Derived Free-standing Metal-free Air Electrode for Oxygen Reduction Reaction. (2017)

4.1 Introduction

Currently, the polymer electrolyte membrane (PEM) fuel cell, owing to its high fuel efficiency and zero emissions at the point of operation, represents one of the most promising energy conversion technologies.[232] For widespread commercialization of PEM fuel cell, one crucial factor is reducing the high cost caused by the exclusive use of expensive platinum-based catalysts at the cathode, due to the slow kinetics of the oxygen reduction reaction (ORR).[233-235] Therefore, searching for efficient and less expensive non-platinum catalysts (NPC) for ORR is extremely desirable to commercialize the clean operating, efficient electrochemical devices.[236-240]

Giving the fact that there are a certain amount of metal impurities in the commercial carbon support like carbon black, carbon nanotubes and graphite, it is unwise to prepare the metal-free catalyst from those. [173, 241, 242] As to those graphene based metal-free catalyst derived from graphite oxide (GO), Wang et al. presented more than 1000 ppm metallic impurities in this type of graphene, which will increase the ORR activity greatly in alkaline electrolyte. [171] Similarly, the commercial carbon black and carbon nanotube normally

contain a certain amount of metal impurities. Therefore, we choose to pyrolyze nitrogen-contained polymer synthesized without any intentional metal content introduced in the procedure. The new nitrogen precursor, poly ([5,5'-bi-1H-benzimidazole]-2,2'-diyl-2,6-pyridinediyl) (PBI-Py), was synthesized without any metal ingredients added in the procedure, implying the totally metal-free nature of the catalyst. The as-prepared free-standing catalyst demonstrates the highly porous structure and huge surface area as well as the high ORR activity in both acidic and alkaline electrolyte.

In this study, we develop a new methodology to fabricate a highly porous free-standing nitrogen doped carbon material as the metal-free catalyst for ORR in both acidic and basic electrolyte. The solution-casting methodology derived from the fabrication of porous membrane procedure is introduced to the catalyst fabrication for the first time. There are several advantages of this methodology for NPMC preparation superior to others. Firstly, with the polymer matrix as the sample placed in the furnace, the final catalyst product tends to be a free-standing carbonized catalyst which could simplify the catalyst layer fabrication in further. Secondly, the porosity of the catalyst could be tuned by the amount of pore agent blended in the casting solution, which could control the activity of the catalyst to a certain degree. Also, the choice of pore agent and combination of different pore agents could be applied to generate different pores in the catalyst. Macropores allows oxygen flowing in the catalyst layer while micro-/meso- pores enables sufficient exposure and improved accessibility of ORR-catalytic sites. [164] Furthermore, considering the high loading of NPMC as opposed to Pt/C, the thick catalyst layer could be replaced by well-designed free-standing carbonized catalyst film.

4.2 Experimental

4.2.1 Synthesis of PBI-Py

The synthesis of PBI is well described in the literature [243]. In this study, according to **Figure 4-1**, 4.7 mmol of 3,30-diaminobenzidine (DAB, Aldrich) with an equivalent molar amount of 2,6-pyridinedicarboxylic acid (PDA, Aldrich) was dissolved in polyphosphoric acid (PPA, Alfa Aesar) in a round-bottom flask with a magnetic stirrer under a slow flow of nitrogen gas. After stirring for 7 h at 200 ^{o}C, the reaction mixture turned dark reddish brown and became viscous. The reaction was quenched by pouring the hot solution into a large amount of cold water. The formed PBI fibers were stirred and washed for 48 h in DDI water and subsequently for 7 h in 2 M ammonium hydroxide solution followed by drying in an oven at 100 ^{o}C overnight.

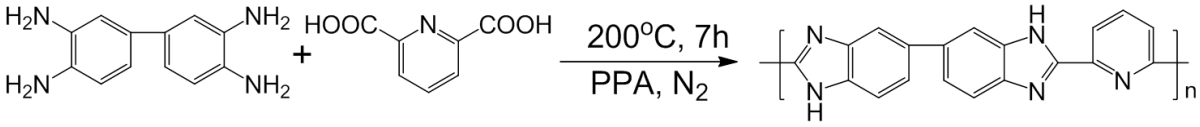

Figure 4- 1 The synthesis and chemical structure of PBI-Py

4.2.2 Preparation of free-standing porous PBI-Py catalyst

A schematic of fabricating KOH-doped porous PBI is displayed in **Figure 4-2**. As shown, 1 wt.% dried PBI-Py polymer with different amounts of dibutyl phthalate (DBP, Aldrich) were dissolved in dimethyl sulfoxide (DMSO, Aldrich) under stirring and heating until an orange homogeneous solution was obtained. Then, it was spread onto a glass plate and placed in an oven. The temperature ramp was from 80 to 190 ^{o}C over 12 h in order to slowly evaporate the solvent. After the heating was finished, the glass plate was immersed in DDI

water in order to detach the membrane from the plate. Then, DBP was extracted by immersing the membranes in methanol for 3 h, 1h per each time. The porous PBI-Py membrane was dried at 80 ^{o}C until a constant weight was achieved. After that, the dry membranes were placed in a quartz tube with the argon gas flowing at a rate of 50mL min^{-1} and gradually heated up to a certain temperature to be annealed for 1h. The free-standing porous N-doped carbon films were carefully taken out from the quartz tube and reserved for different characterizations. Here, the catalysts were named as xPBI-Py-T, where x represents the ratio of DBP accounts in casting solution (60, 90 and 95%) and T stands for the annealing temperature (800, 900, 1000 and 1100 ^{o}C), respectively.

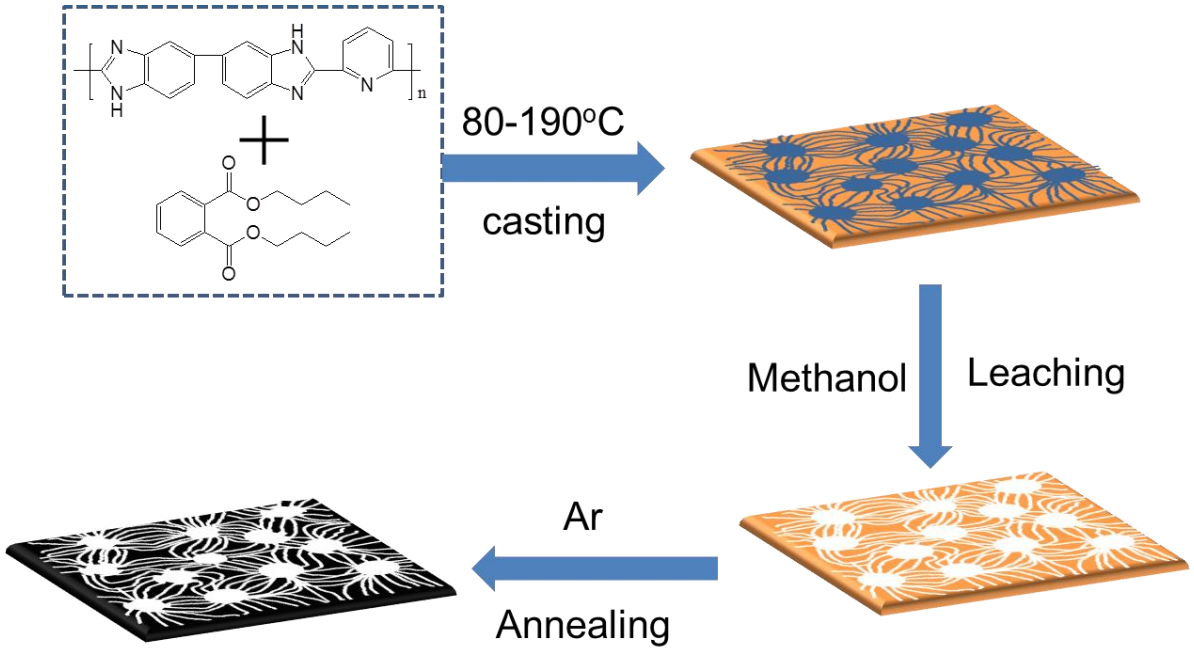

Figure 4- 2 The schematic for the fabrication of xPBI-Py-T catalyst

4.2.3 Structural and physicochemical characterization

1H NMR spectra and FT-IR spectra were applied to identify the structure of PBI-Py. 1H NMR spectra were measured at 500 MHz on a Bruker Analytik GmbH spectrometer. FT-IR

spectra were recorded on 35-40 μm thick membrane samples using a PerkinElmer-283B FT-IR spectrometer. Scanning electron microscopy (SEM) (LEO FESEM 1530) and transmission electron microscopy (TEM) (Philips CM300) was utilized to observe the morphology and surface structure. Brunauer-Emmett-Teller (BET) (Micromeritics ASAP 2020) analysis is used to obtain the nitrogen adsorption-desorption isotherm and the surface area of catalyst in further. X-ray diffraction (XRD) (AXS D8 Advance, Brunker) using Cu Kα source and Raman spectroscopy (Senterra, Brunker) are used to identify the graphitic structure and defects in the catalyst after pyrolysis. X-ray photoelectron spectroscopy (XPS) (K-Alpha XPS spectrometer, Thermal Scientific) was conducted to determine the atomic composition and elucidate the identity of nitrogen species on the surface.

4.2.4 Electrochemical characterization

ORR activity was evaluated by RDE and RRDE testing. A potentiostat (Pine Instrument Co., AFCBP-1) was connected to a rotation speed controller (Pine Instrument Co., AFMSRCE). A conventional three-compartment electrochemical cell was applied. A saturated calomel electrode (SCE) and a reversible hydrogen electrode (RHE) were used as reference electrodes in basic (0.1M KOH) and acidic (0.1M $HClO_4$) electrolyte respectively. All potentials reported herein have been converted to the RHE scale. The RRDE, the working electrode, consists of a glassy carbon electrode (5 mm OD), giving an apparent surface area of 0.19635 cm^2 and a platinum ring electrode (99.99 % Pt, 6.5 mm ID, 7.5 mm OD), while a graphite rod functions as the counter electrode. The working electrode was prepared as follows. Initially, 2 mg of the catalyst was dispersed ultrasonically in 500 μL 0.03 wt.% Nafion/isopropanol for two hours. Then, 30 μL of the above solution was

deposited onto the glassy carbon electrode and allowed to dry to achieve the loading of 0.6 mg cm^{-2}. Prior to each test, the electrode was cycled several times in the range of 0~1.2 V v.s. RHE in the acidic electrolyte and -1~0.2 V v.s. SCE in the basic electrolyte to produce clean surfaces and activate the catalysts. Cyclic voltammetry (CV) was done under both nitrogen and oxygen saturated electrolyte at a scan rate of 50 mV s^{-1}. Linear sweep testing was performed in oxygen saturated electrolyte at the rotation speeds of 100, 400, 900, 1600 rpm and a scan rate of 10mV s^{-1}. Background currents obtained under nitrogen saturation were removed to eliminate capacitance and redox contributions.

4.3 Results and discussion

The **Figure 4-3a** represents 1H NMR spectra of PBI-Py using deuterated dimethyl sulfoxide (DMSO-d6) solutions, which confirm the successful synthesis of the polymer. The proton chemical shifts (δH) are 13.22 (H1), 8.33 (H2), 8.05 (H3 & H4), 7.86 (H5), 7.67 (H6) [243], which are assigned to the protons on the aromatic groups in PBI-Py.

The FT-IR spectrum of the developed PBI-Py membrane is shown in Figure 4-3b. In this figure, the typical absorption peaks ascribed to the PBI-Py membrane were observed at 804 cm^{-1} (heterocyclic-ring vibration or C-H out-of-plane bending), 1271cm^{-1} (imidazole ring breathing), 1306 cm^{-1} (bending vibration of N-H), 1456 cm^{-1}(in-plane ring vibration of pyridinediyl benzimidazole), 1572 cm^{-1} (stretching of C=N), 1599 cm^{-1} (ring vibration of conjugation between benzene and imidazole rings), 1629 cm^{-1} (C=C stretching), and 3172 cm^{-1} (self-associated N-H stretching) [243, 244]. With the help of analysis of NMR and FT-IR, the structure of PBI-Py was identified as it is described in the literature. [245]

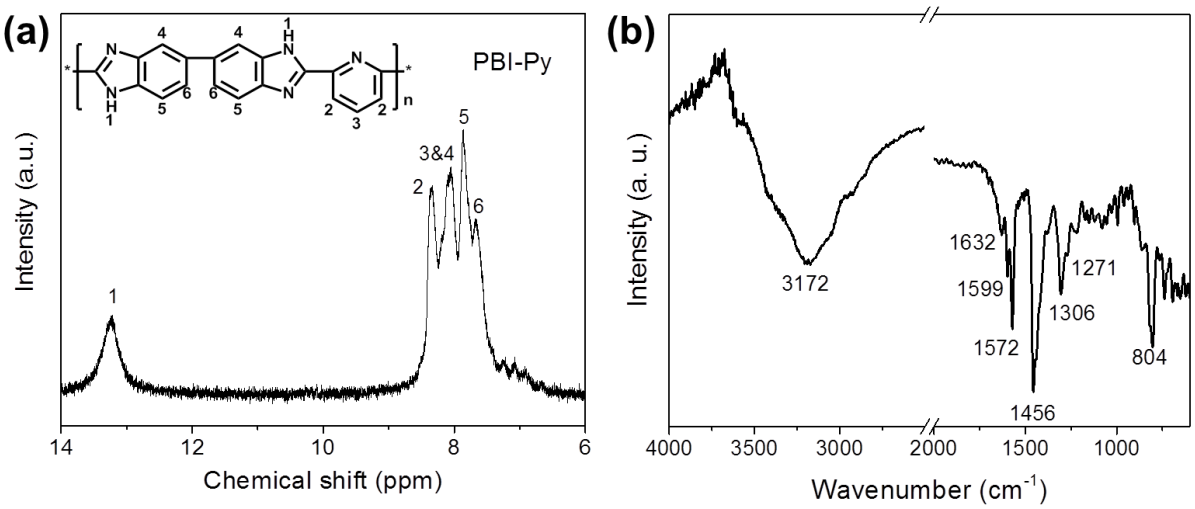

Figure 4- 3 (a) NMR and (b) FTIR spectra of synthesized PBI-Py

After leaching out DBP, the porous PBI-Py membrane is obtained as an opaque yellow membrane in **Figure 4-4** (left) whilst it turns into a totally black carbon film after the pyrolysis at high temperature **Figure 4-4** (right). The fact that the membrane shape did not collapse indicates its potential as the free-standing catalyst/electrode for ORR.

Figure 4- 4 Digitial photos of porous PBI-Py film before (left) and after pyrolysis (right)

The microstructure of porous PBI-Py membranes before and after pyrolysis was investigated by SEM. As shown in Figure 4-5, the porous structure was identified in the cross-section of PBI-Py membranes both before and after pyrolysis. Figure 4-5 (a-c) demonstrated a trend that the more DBP was introduced, the more porous and the thicker is

the membrane. It is noted that the pore was not distributed homogeneously in low porosity PBI-Py membrane **(Figure 4-5a)** which displays a dense surface layer. The pores in those pristine PBI-Py membranes are of micrometer size. After being annealed at 1000^{o}C for 1h, those xPBI-Py-1000 samples demonstrated denser structure and lower thickness as opposed to those pristine membranes according to the cross-section SEM in **Figure 4-5 (d-f).** When they were zoomed in further, interconnected nano-sized pores were found instead of large micron-sized pores **(Figure 4-6 (a-c))**. The carbon walls for pores are varying from ca. 100 to 200 nm. The pore size shrinking could be resulted from the melting and thermal decomposition of PBI-Py polymer chain when the membrane was gradually heated in the furnace. At the same time, the surfaces of different carbon films shown in **Figure 4-6 (d-f)** demonstrate a significant difference. With the increase of DBP introduced into the original porous PBI-Py film, the obtained carbon films show an increase in nano-size pores and decrease in micron-size pores and the carbon around the void changes from interconnected webs and fibrils to piled fine nano-rods and nano-branches.

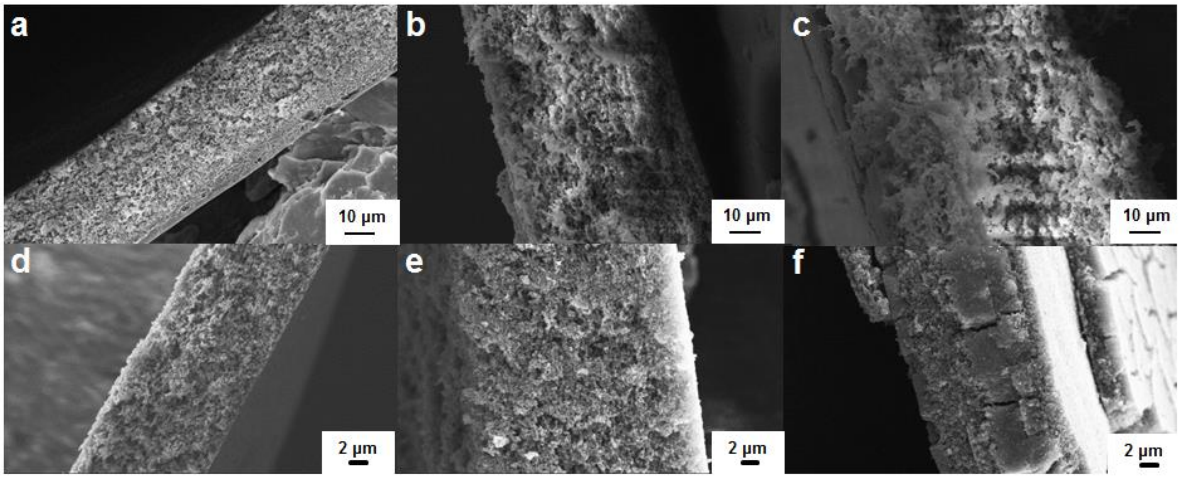

Figure 4- 5 Cross-section SEM images of xPBI-Py membranes before (a, b, c) and after pyrolysis (d, e, f), where the porosity, x equals to 60% (a, d), 90% (b, e) and 95% (c, f).

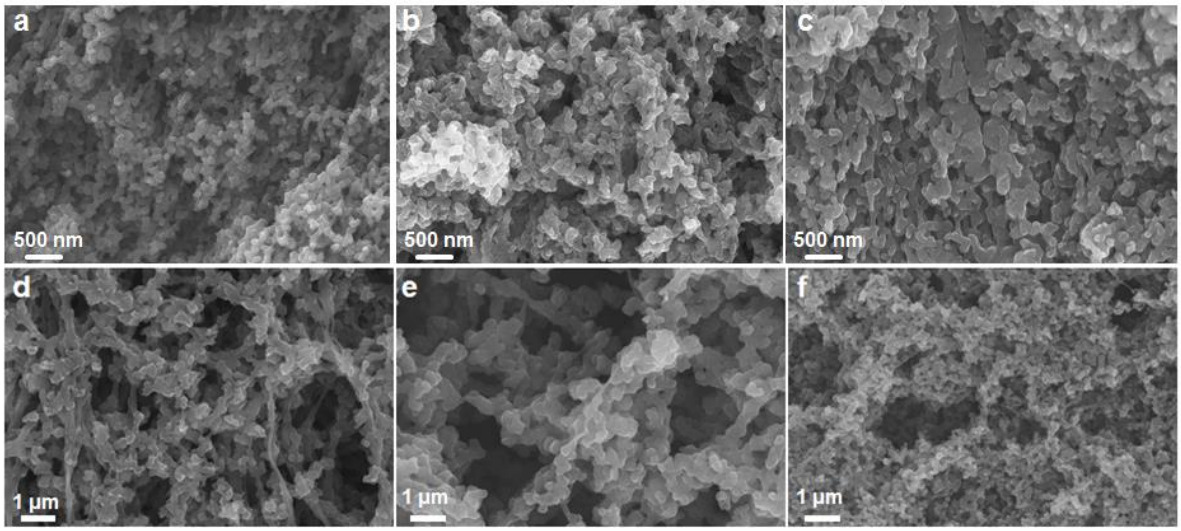

Figure 4- 6 SEM images of cross-section (a-c) and surface (d-f) of xPBI-Py-1000, where the porosity, x equals to 60% (a, d), 90% (b, e) and 95% (c, f).

Figure 4-7 displays the surface morphology of 95PBI-Py-T catalyst with different annealing temperature. The surfaces of 95PBI-Py-T catalysts appeared highly porous with macropores as large as micrometers **(Figure 4-7 (a-d))** and smaller nano-sized pores among the carbon network **(Figure 4-7 (e-h))**. The 3D-macroporous framework structure of 95PBI-Py-T is similar to the catalyst structure derived from the commercial cellulose filter film.[164] Furthermore, its highly porous structure does not change much along with the increase of annealing temperature. Then, the morphology of 95PBI-Py-1000 catalyst was investigated in further by TEM. As displayed in **Figure 4-8a**, the carbon network structure is found and the size is varied from 100-200 nm. The small gaps or pores among each carbon flakes in **Figure 4-8b** is less than 100 nm and part of them are mesoporous. Large amounts of micropores in the catalyst contributed greatly to the specific surface area. Macropores and a small amount of mesopores were co-existed, which is in agreement with the SEM and TEM images.

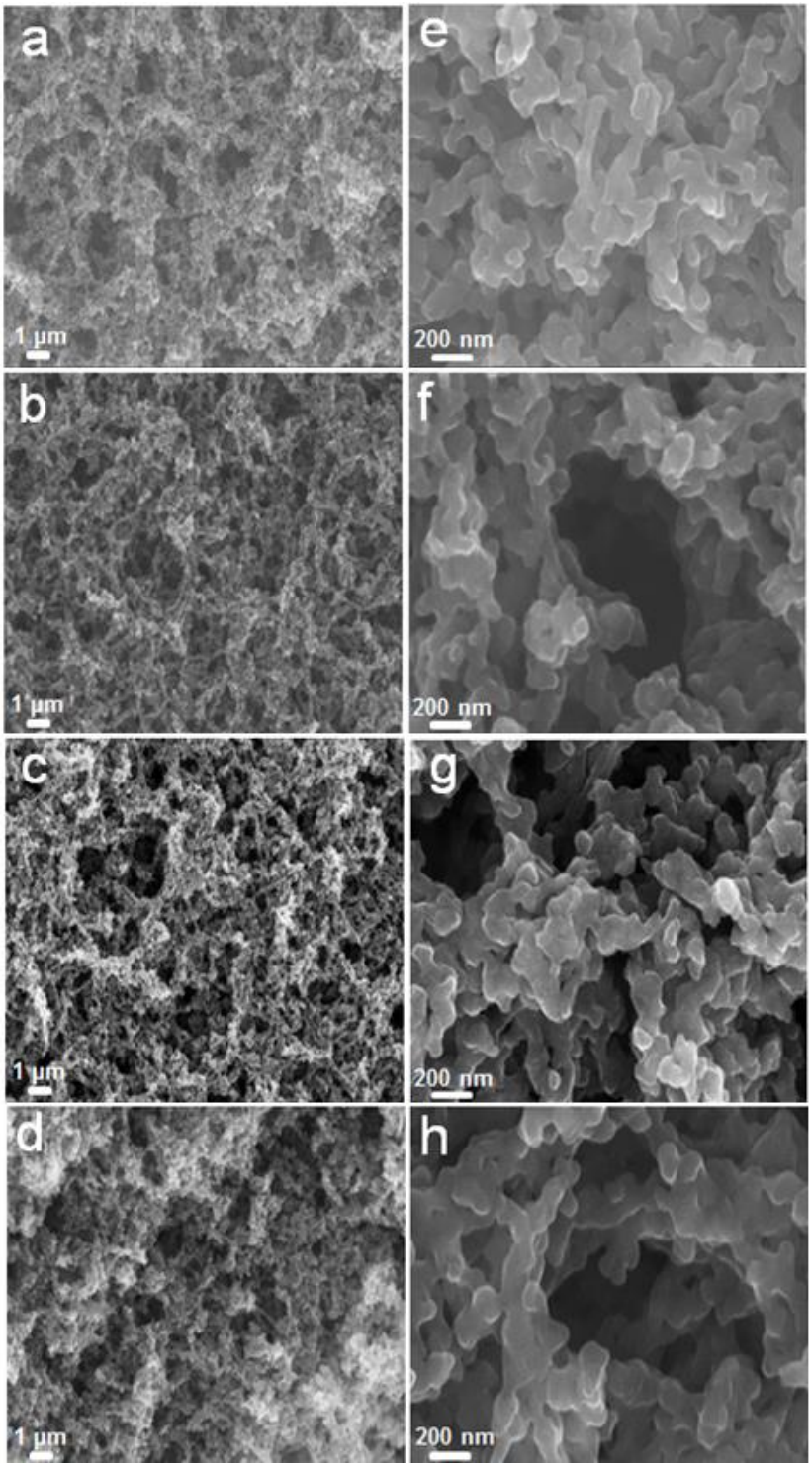

Figure 4- 7 Surface SEM images surface of 95PBI-Py-T, where the heat treatment temperature, T equals to 800^{o}C (a, e), 900^{o}C (b, f), 1000^{o}C (c, g) and 1100^{o}C(d, h).

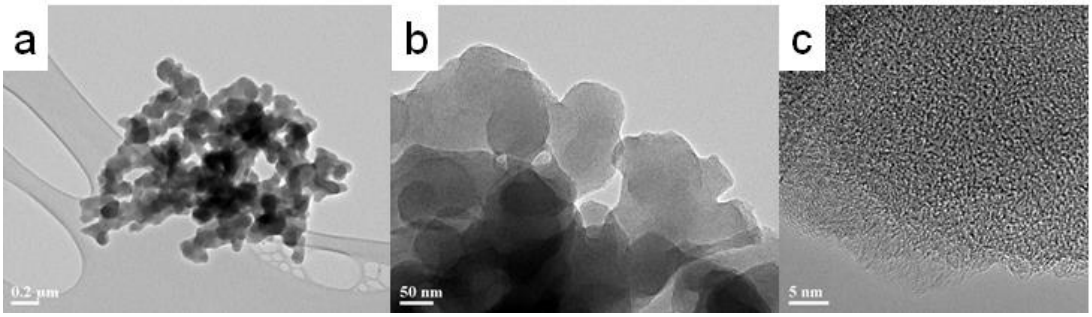

Figure 4- 8 TEM (a,b) and HR-TEM (c) images of 95PBI-Py-1000

The nitrogen adsorption-desorption isotherm plots of catalysts with different porosity were obtained from BET analysis (**Figure 4-9a**). The specific surface area of xPBI-Py-1000 increases together with the amount of DBP mixed with PBI-Py, giving the value of 469, 600 and 902 m^2 g^{-1} for 60%, 90%, and 95% porosity, respectively. The increase of surface area is in line with the morphology in SEM images. All three curves resembles each other----the nitrogen adsorption increased dramatically at the low relative pressure, which implied the existence of micropores in the sample. The typical pore distribution for xPBI-Py-1000 is calculated by BJH method and plotted in **Figure 4-9b**. Large amounts of micropores in the catalyst contributed greatly to the specific surface area. Macropores and a small amount of mesopores were co-existed, which is in agreement with the SEM and TEM images.

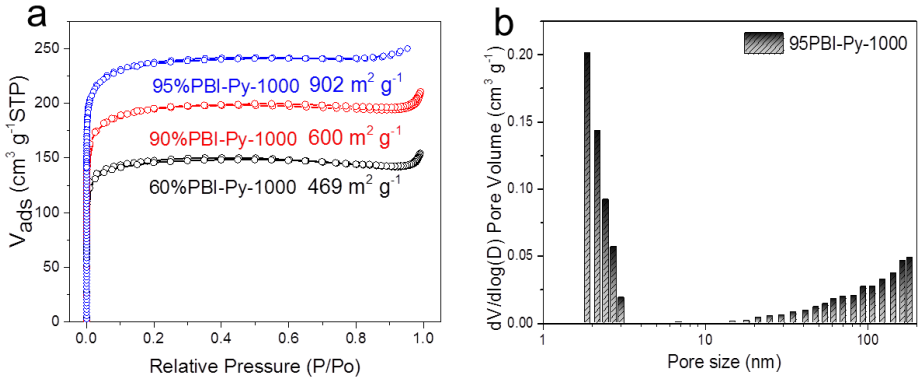

Figure 4- 9 (a) Nitrogen adsorption-desorption isotherm of xPBI-Py-1000 (x= 60%, 90% and 95%) and (b) BJH method-calculated pore size distribution for 95%PBI-Py-1000.

After being annealed at high temperature, the backbone of PBI-Py polymer chain decomposed and changed into the carbon. The Raman spectra in **Figure 4-10** are applied to characterize the carbon structure of catalyst, giving two peaks at 1340 and 1580 cm^{-1}, corresponding to the characteristic D and G bands, respectively, of graphitic carbons.[141] As the G band is related to tangential vibrations of sp^2 carbon atoms, [141] its presence on the spectra is suggestive of the existence of graphitic structure in xPBI-Py-T. On the other hand, the D band, which corresponds to the defect band, must be due to the presence of N, O dopant atoms and the concomitant absence of some graphitic carbons in the xPBI-Py-T materials.

By obtaining the ratio of intensities of the two bands (i.e., I_D/I_G), [141] the relative degree of order/disorder in the xPBI-Py-T materials is then determined. In the case of 95%PBI-Py-T **(Figure 4-10a)**, the I_D/I_G ratio decreases from 1.07 to 0.98 when the pyrolysis temperature is raised from 800 ℃ to 1100 ℃, which indicates the increase in the degree of ordered graphitic structure in materials prepared at higher pyrolysis temperatures.[141] Although the I_D/I_G ratio of xPBI-Py-1000 increases slightly along with porosity, the change is not significant, suggesting in-plane graphitic (or defect) structure is independent of the amount of DBP used for the membrane casting (Figure 4-10b). The effect of DBP amount on I_D/I_G ratio is similar to published work on the metal-free catalyst fabricated with silica colloid as the pore agent. [141]

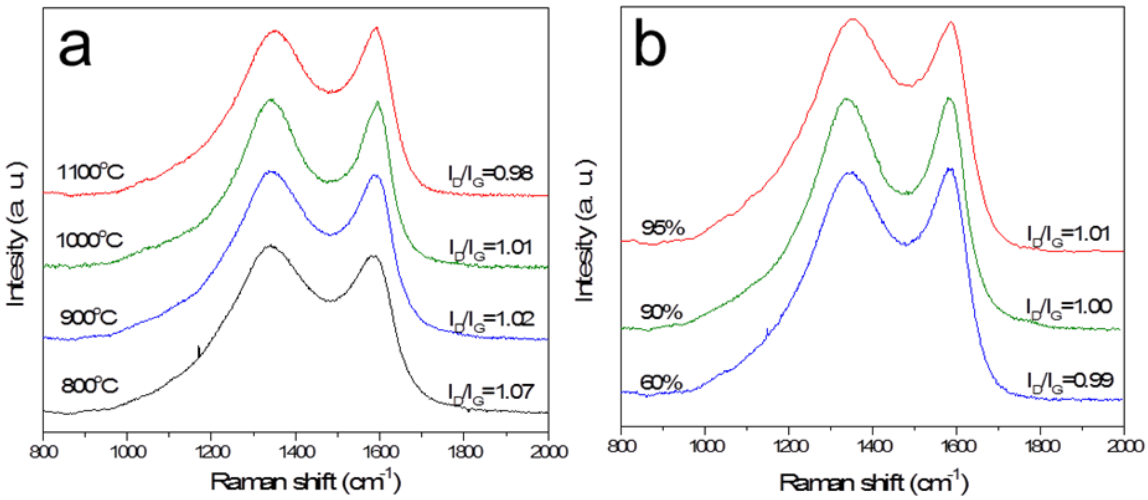

Figure 4- 10 Raman spectra of (a) 95PBI-Py-T and (b) xPBI-Py-1000

Also, XRD is applied to check the crystal structure of carbon in **Figure 4-11**. The figure shows a major peak (002) at 23.73°, 22.80° and 22.83° which corresponds to an average interlayer spacing of 3.75, 3.90 and 3.89 Å for xPBI-Py-1000 with 60, 90 and 95% porosity respectively. These d-spacing values are a little larger than that of graphite (3.36 Å) due to doping with nitrogen and oxygen.[196] It is interesting to note that increasing the porosity could lead to the increase of d-spacing. The more pore agents were introduced, the more defects or disorder were generated in the xPBI-Py-1000 catalyst. The effect of porosity on the graphitic structure is more significantly illustrated by XRD pattern than Raman spectra, which may be ascribed to the influence of highly porous structure on the detected angle of X-ray. In addition, the widening of (002) peak, i.e. the π-stacking peak, is evidence that high porosity can help to exfoliate the nano-graphitic π-stacks in the xPBI-Py-1000 catalyst and results in the possible increase of exposed active sites. [164] Around 43°, there are weak diffraction peaks that correspond to (100) planes.[164, 196]

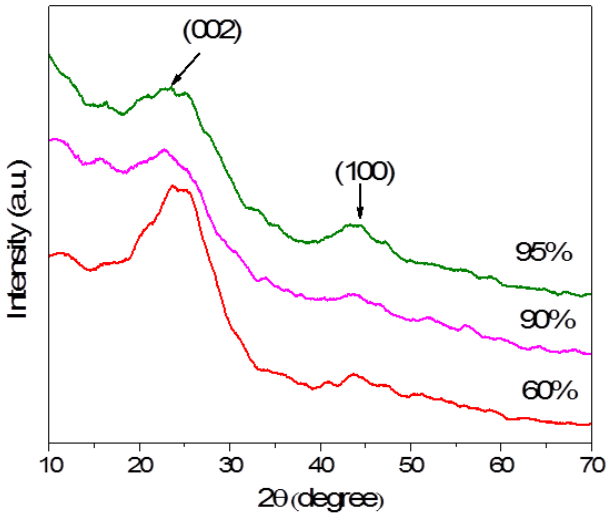

Figure 4- 11 XRD pattern of xPBI-Py-1000

The XPS survey spectra of 95PBI-Py-T materials **(Figure 4-12a)** shows three prominent peaks associated with C 1s, N 1s and O 1s electrons without any other peaks for the transition metal like iron or cobalt, which indicates the fact of no metal in the catalyst. The composition, in term of the ratio of nitrogen to carbon (N/C) is varied with the anneal temperature **(Figure 4-12b)**. Specifically, the N/C ratio kept decreasing along with the elevated temperature, from 9.46% at 800^{o}C to 1.64% at 1100^{o}C, which is in agreement with plenty of nitrogen-doped carbon materials. [140-142] High-resolution N 1s XPS peaks of 95PBI-Py-800 were placed in the **Figure 4-12c** to illustrate the nitrogen species on the surface of the catalyst. Four peaks corresponding to pyridinic-N (~398 eV), pyridonic or pyrrolic-N (~400 eV), quaternary-N (~400 eV), and oxized-N (403-405 eV) species were deconvoluted.[141] As the pyrolysis temperature is raised from 800 to 1100 ℃, the percentage of quaternary-N increases, whilst those of pyridonic or pyrrolic-N and pyridinic-N decrease and the ratio of oxidized nitrogen varies in a certain range **(Figure 4-12d)**.

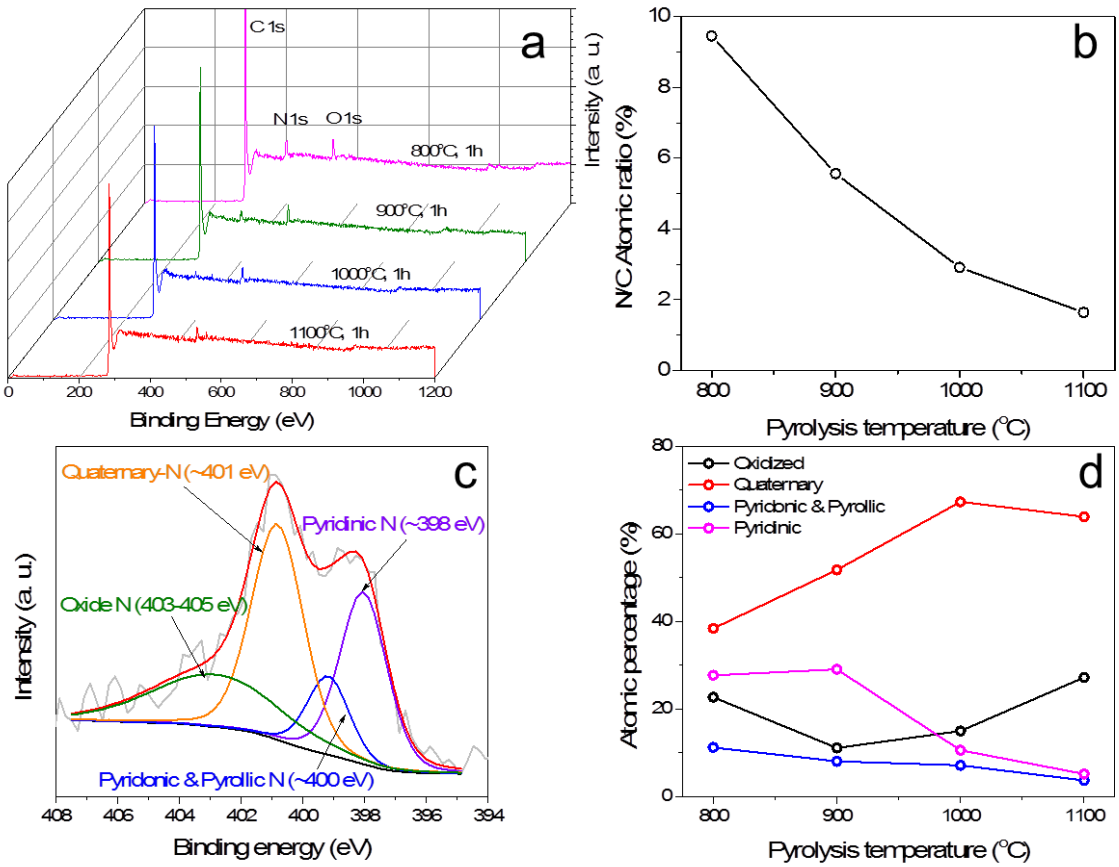

Figure 4- 12 XPS analysis: (a) survey spectra of 95PBI-Py-T (b) N/C atomic ratios versus pyrolysis temperature, (c) Typical high-resolution XPS spectrum of N 1s for 95%PBI-Py-800 and (d) N species present in 95%PBI-Py-T materials, where T is 800, 900, 1000 or 1100 ℃.

In order to confirm the nature of metal-free catalysts, the high-resolution Fe 2p XPS spectrum of a catalyst is shown in **Figure 4-13**, indicating no significant amount of iron exists in 95%PBI-Py-1000 catalyst. Considering the resolution of elemental detection of XPS is 0.1% in atomic, ICP-OES test is conducted to precisely determine the metal content in the final catalyst. As presented in **Table 4-1**, the transition metals that reported to be ORR-active, including Fe, Co, Ni and Mn were found to be lower than 10 ppm in the final

95%PBI-Py-1000 catalyst. According to literature,[173] the significant ORR activity enhancement in an alkaline electrolyte of N-doped carbon materials was observed only when the iron content reaches as high as 50 ppm. Generally, Mn-based M-N-C catalyst is not as ORR active as Fe-based M-N-C catalyst.[246] Thus, by extension, the threshold of Mn content in N-doped carbon materials that could noticeably improve ORR activity is even lower. Therefore, 95%PBI-Py-1000 is a real metal-free catalyst.

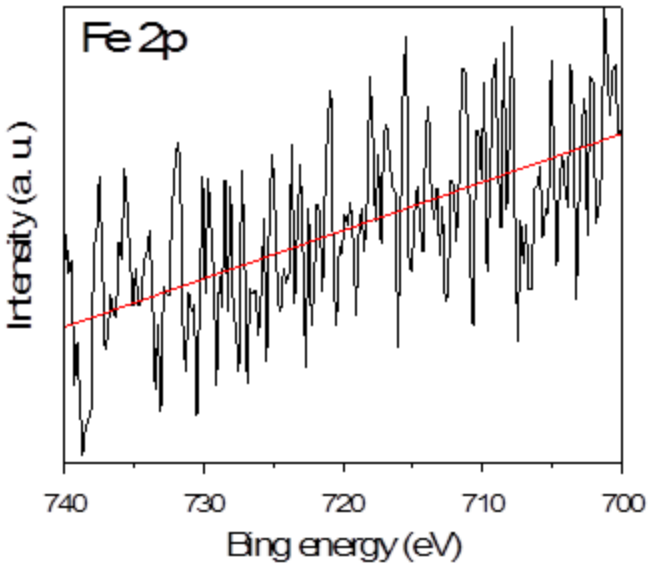

Figure 4- 13 High-resolution Fe 2p XPS spectrum of 95%PBI-Py-1000

Table 4- 1 Metal impurities in 95%PBI-Py-1000 detected by ICP-OES

Elements	Metal content /ppm
Mn	5.96 ± 0.09
Ni	3.44 ± 3.37
Fe	0.54 ± 0.36
Co	Not detected

The ORR activity of different xPBI-Py-T catalysts is investigated and demonstrated in Figure 4-13. According to **Figure 4-14a**, 60%PBI-Py-900 shows relatively low on-set

potential, half-wave potential and limiting current at about 0.6V, 0.4V and 2 mA cm^{-2} in the acidic electrolyte. Once the porosity increases to 90%, the limiting current increases as opposed to 60%PBI-Py-900. Then, the on-set potential and half-wave potential could be greatly enhanced to 0.8V and 0.435V respectively when five more percent of porosity was introduced. The result shows more ORR activity than that of the complex of cobalt and PBI-Py coated carbon nanotube in the literature.[245] Then, a 95%PBI-Py membrane was chosen to investigate the effect of pyrolysis temperature on the ORR activity. Four LSV curves corresponding to anneal temperature of 800, 900, 1000 and 1100 ^{o}C appears similar to each other (**Figure 4-14b**). With the increase of the annealing temperature, the half-wave potential shifted positively from 0.34V to 0.53V. The difference between 95%PBI-Py-1000 and 95%PBI-Py-1100 lies in the larger limiting current for the latter.

Likewise, xPBI-Py-900 catalysts were performed in 0.1M KOH solution (**Figure 4-13**c). The ORR activity of the catalyst is much higher and the improvement of ORR activity attributed to the porosity is more significant in the basic electrolyte as opposed to those in acidic condition. The dramatic increase in term of the on-set potential, half-wave potential and limiting current from 0.88V, 0.63V and 2.3mA cm^{-2} for 60%PBI-Py-900 to 0.95V, 0.8V and 3.4 mA cm^{-2} for 95%PBI-Py-900 respectively proves the importance of porosity to ORR activity directly. Then, 95%PBI-Py-T catalysts loaded to check the effect of pyrolysis temperature on the ORR activity. The ORR activity was enhanced when anneal temperature increased to 1000^{o}C and it degraded marginally when the temperature reached 1100^{o}C. The on-set potential of 95%PBI-Py-1000 could reach as high 0.96V which is close to the work of heat-treated PBI-BuI coated carbon nanofiber whilst the half-wave potential, 0.82V, in this work is much higher than that of reported work which around 0.77V.[247] The ORR activity is

close to the performance of commercial Pt/C catalyst and is much higher than that of reported N-doped carbon metal-free catalysts. [140, 141, 163] To sum, the high porosity and high temperature treatment could enhance the ORR activity for xPBI-Py-T in both acidic and basic electrolyte and the 95%PBI-Py-1000 could be a promising metal-free catalyst for ORR both two kinds of electrolytes.

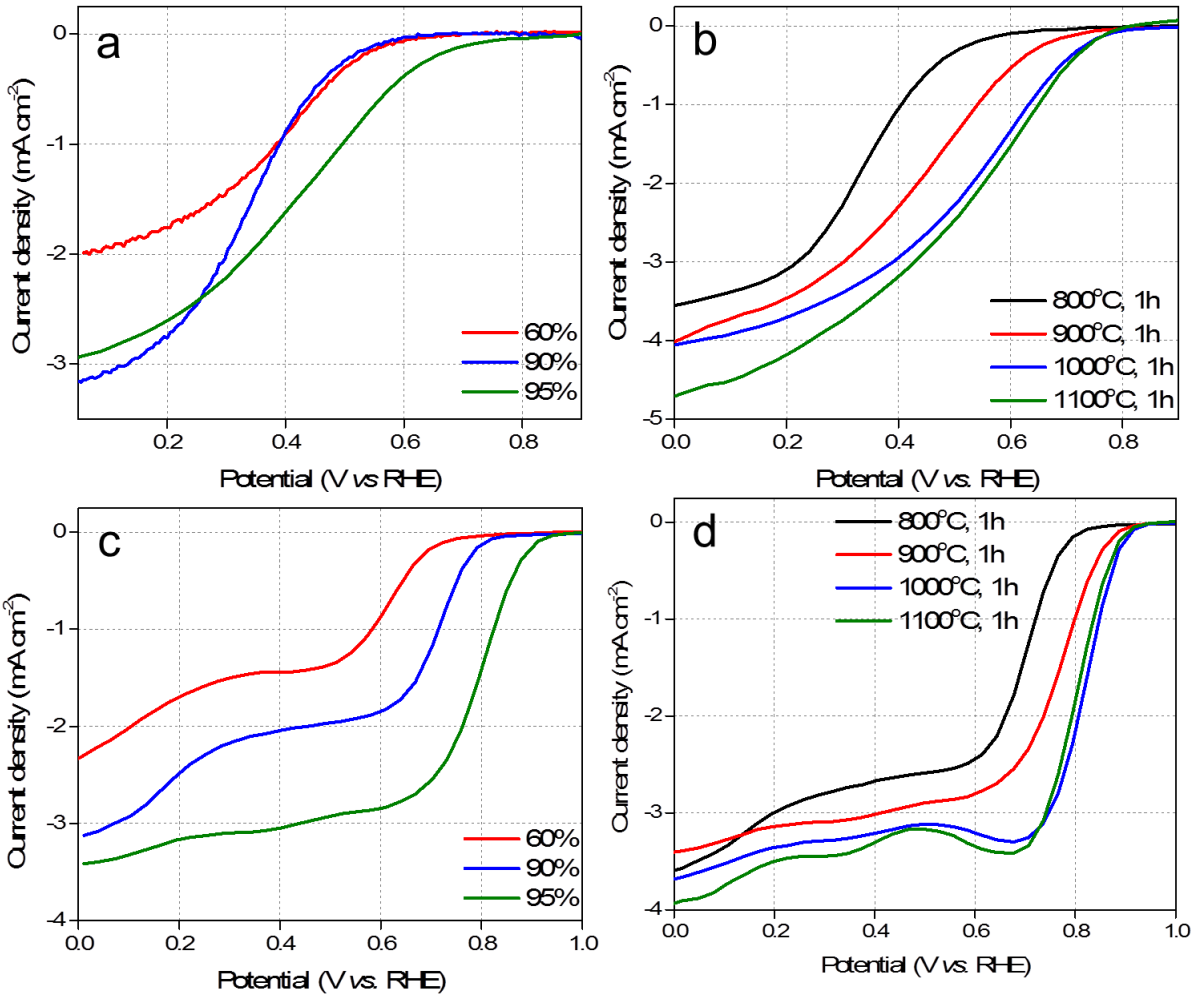

Figure 4- 14 Polarization curves of xPBI-Py-900 catalyst (x=60, 90 and 95%) performed in O_2 saturated (a) 0.1M $HClO_4$ and (c) 0.1M KOH and polarization curves

of 95PBI-Py-T (T= 800, 900, 1000 and 1100^{o}C) tested in O_2 saturated (b) 0.1M $HClO_4$ and (d) 0.1M KOH at rotation speed of 900rpm.

The stability of the optimal catalyst, 95%PBI-Py-1000 is assessed via ADTs in the half-cell measurement in the alkaline medium. After repeating cycles from 0 to 1.2 V vs RHE for 6000 times in the N_2-saturated electrolyte, the CV curves decrease marginally, indicating a slight decrease (< 5%) in capacitance of the catalyst, hence the electrochemical surface area **(Figure 4-15a).** The polarization curve of 95%PBI-Py-1000 shown in the **Figure 4-15b** after cycles demonstrate unchanged on-set potential and half-wave potential, giving 0.96 V and 0.82 V vs RHE, respectively, implying the unchanged kinetic mechanism of ORR. The only difference is the decrease of limiting current density (3.02 mA cm^{-2} vs. 3.36 mA cm^{-2}), indicating the change of diffusion onto the active sites, which could be attributed to the decrease in electron conductivity or in hydrophobicity. By comparison, commercial Pt/C catalyst is tested in the same condition, giving a dramatic decrease of half-wave potential from 0.86 V to 0.80 V vs. RHE (**Figure 4-15c**). Therefore, in terms of half-wave potential, 95%PBI-Py-1000 demonstrates superior stability to that of commercial Pt/C catalyst. Furthermore, the stability of 95%PBI-Py-1000 and Pt/C in the presence of methanol is compared in the **Figure 4-15d**, showing that the metal-free catalyst is tolerant to the methanol while Pt/C is not. The superiority in methanol tolerance 95%PBI-Py-1000 to Pt/C catalyst indicates less fuel cross-over effect as well as poison effects on ORR catalyst.[20, 168]

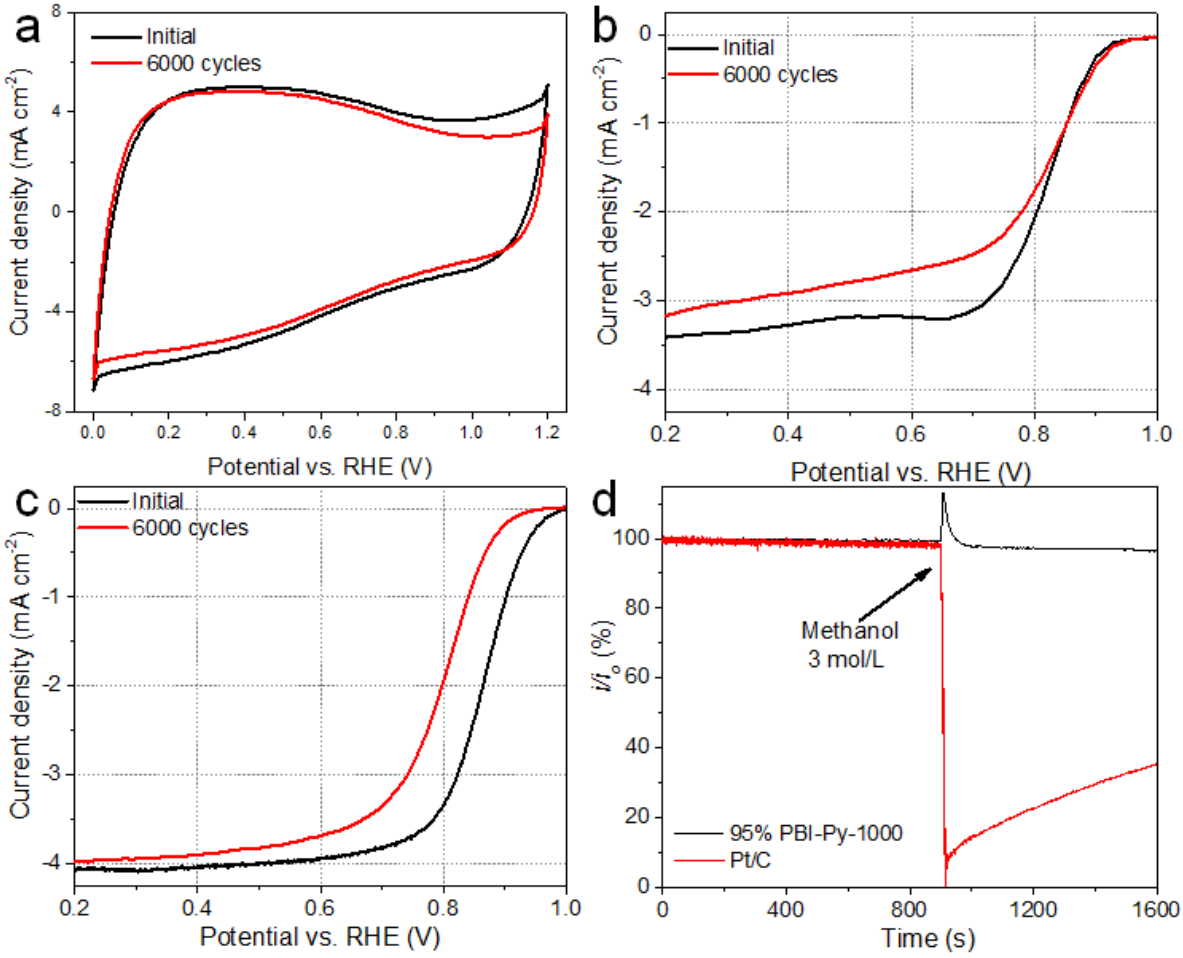

Figure 4- 15 (a) CV curves and (b) polarization curves of 95%PBI-Py-1000 catalyst as well as (c) polarization curves of Pt/C before and after ADT tests cycling from 0 to 1.2 V vs RHE in N_2 saturated 0.1M KOH for 6000 times with scan rate of 50 mV s^{-1}. (d) Methanol tolerance of 95%PBI-Py-1000 catalyst and Pt/C catalyst. Methanol is added into the electrolyte to reach a concentration of 3 mol L^{-1} at about 900 s.

4.4 Conclusions

The highly porous free-standing metal-free catalysts were successfully prepared by the solution casting methodology followed by annealing the porous PBI-Py membrane at

high temperature. The specific 3D nano-network structure, giving the specific surface area as high as 902 m^2 g^{-1} for 95PBI-Py-1000, entitled the catalyst with high ORR activity in both acidic and basic electrolyte. RDE tests show that both porosity and higher annealing temperature could improve the ORR activity greatly in both acidic and alkaline electrolyte. Among all the samples tested, the 95%PBI-Py-1000 demonstrates the highest ORR activity, which is even higher than that of reported metal-free catalysts. Specifically, 95PBI-Py-1000 shows comparable activity to commercial Pt/C catalyst in alkaline electrolyte. The high ORR activity of 95PBI-Py-1000 proves the feasibility of this solution casting methodology for the catalyst fabrication and the promising potential of PBI-Py as the nitrogen precursor for NPMC fabrication.

Chapter 5: Mesoporous Nitrogen-doped Carbocatalysts Derived from Cellulose Nanocrystals as Metal-free Catalyst for Oxygen Reduction Reaction

This chapter is based on the following works that are submitting to *Carbon* and *Applied Catalysis B: Environmental*, respectively.

G. Jiang,[†] X. Wu,[†] M. Chen, A. Yu, R.M. Berry, Z. Chen, K.C. Tam, Mesoporous Nitrogen-doped Carbon Nanorods Derived from Biomass as Metal-free Carbocatalysts, *Carbon.* 2017

X. Wu,[†] G. Jiang,[†] M. Chen, Q. Yao, A. Yu, J.Y. Lee, R.M. Berry, K.C. Tam, Polydopamine-modified N-enriched mesoporous carbon derived from biomass for supporting highly dispersed metal nanocatalysts, *Applied Catalysis B: Environmental*, APCATB-D-17-00970

5.1 Introduction

Catalysts play a pivotal role in 90% of the chemical process and the manufacturing of over 60% of the chemical products.[248] Various homogeneous or heterogeneous metals, metal oxides, or hybrid composite materials have been extensively explored since they are among the most vibrant catalysts for a wide range of reactions in modern chemistry. However, the challenges associated with the real world application of these catalysts are most commonly related to nanoparticle agglomeration, catalyst leaching, and reusability, which directly lead to the decay of catalytic performance, economics, and environmental problems. Moreover,

the high cost and low abundance of the metal-based material further restrict their usage industrially. Increasing research activities are directed towards the exploration of metal-free, and cost-effective catalyst materials derived from the abundant resources as sustainable alternatives to traditional metal-based catalysts. Within the context, 'carbocatalyst' has evolved as a new class of catalysts and the materials used are carbonaceous materials composed predominantly of carbon. In this case, carbon is used exclusively as catalysts rather than as the support for traditional metal/metal oxides. In recent years, zero-dimensional fullerene, one-dimensional carbon nanotubes, two-dimensional graphene and various three-dimensional carbon nanostructures have been proposed.[249-254] It was further demonstrated experimentally and theoretically that doping with heteroatoms can effectively enhance the catalytic activity of carbocatalysts as the result of the unique electronic properties due to heteroatom-induced charge transfer and delocalization[160, 255]. Nitrogen (N) is the most widely-investigated doping element and various N-doped carbon materials including carbon nanotube[256, 257], carbon nanofiber[111, 258], porous carbon[259], graphene[2, 260-262] *etc.* have been developed. Within the context, most of the studies on N-carbocatalyst focused on catalyzing oxygen reduction reaction (ORR) and their results suggest an excellent catalytic activity with long-term durability, and higher tolerance to poisoning than metal-based catalysts[141, 163, 164]. In these studies, the high catalytic activity surpassing metal-based catalyst was achieved, and the critical role of N doping was clearly demonstrated.

Despite its promise, significant challenges still remain for achieving the adequate and homogeneous N doping using simple procedure and apparatus that meets the practical considerations.[263, 264] It is also highly desirable to engineer the carbon structure with controlled mesopores (pores within 2nm - 50nm) that were demonstrated to efficiently

reduce the mass transfer and accelerate the reaction kinetics[265] Current strategies to achieve N-doped mesoporous carbon structures often necessities the use of exotic hard templates, expensive surfactants, high-cost polymeric carbon sources and complicated procedures, which is costly, energy-consuming and low in yield.[265] Post-activation at an extremely high temperature (>1000^{o}C) are also applied for the desired porosity.[265] Therefore, the motivation of this research is to develop a facile synthesis of mesoporous N-doped carbon as high efficient metal-free catalysts using abundant and environmental benign resources for practical applications.

As a new class of nanomaterial derived from renewable biomass, cellulose nanocrystals (CNCs) can be extracted from plants and marine animals. The high aspect ratio, superior mechanical properties, water dispersibility and highly reactive surface, make CNC an ideal platform for various functionalizations.[266] The material itself is an ideal carbon source and is also promising for templating various carbon structures.[266] Moreover, Canada has commissioned a demonstration plant that can produce 1000 kg per day, giving tremendous impetus to its wide application.

In this research, mesoporous N-doped carbon nanorods (N-CNRs) were fabricated from melamine formaldehyde (MF) coated cellulose nanocrystals (CNCs). CNCs with unique rod-structure was used as the main carbon precursor for self-templated carbon nanorod. It also serves as an ideal template to induce the well-controlled MF polymerization on the surface of CNCs before pyrolysis. The functionalization of highly porous MF resin not only introduces desired N-doping but also generates favorable mesoporous structure prior to pyrolysis. Moreover, the coating of MF resin was demonstrated to critically protect and stablize the fibrous shape of CNCs during carbonization, contributing to the high surface

area and pore volume of N-CNR. A very high N-doping content and mesoporous carbon structure were achieved through a facile one-step pyrolysis without using any sacrificing template or activation process. N-CNRs also exhibit excellent catalytic activity for ORR, with a high on-set potential of 0.87V (vs RHE), a half-wave potential of 0.73V (vs RHE) as well as a decent selectivity to four electron reduction pathway of oxygen. We believe that our strategy of synthesizing mesoporous N-doped carbon nanostructure from widely available biomass with low-cost processing provides a practical and sustainable alternative as a metal-free catalyst for a wide range of electrochemical or chemical applications.

5.2 Experimental

5.2.1 Materials and Catalyst Synthesis

Cellulose nanocrystals (CNCs) were provided by FP Innovations and Celluforce Inc. All the chemicals used in this study were of analytical grade, purchased from Sigma-Aldrich, and used as received. In a typical synthesis, 2.2 g of melamine and 4.0 mL of formaldehyde (37% in water) were mixed in 10 mL deionized water in a 50 mL flask, followed by pH adjustment to be between 8 and 9 using NaOH solution. The temperature was increased to 80 ℃ under mechanical or magnetic stirring. The solution turns from cloudy to transparent within about 5 min. After 30 min, the precursor is ready for the next step. 100 mL of 1% CNC suspension was mixed with the MF precursor from step 1, and the pH was adjusted to between 4 and 5 using HCl solution. The suspension was stirred for 2 h at 80 ℃. During the process, the cross-linked melamine formaldehyde resin condenses on the CNC surface and forms a coating. The suspension was then allowed to cool to room temperature and purified

by repeated filtration and washing with DI water. MF resin was synthesized under identical conditions in the absence of CNCs. The nitrogen-doped carbonized MFCNCs (N-CNRs) were prepared by pyrolysis of freeze-dried MFCNCs in a quartz tube under a flow of argon at a desired temperature of between 900 ℃ over 2 hours at 5 ℃ min^{-1}. After cooling to room temperature, N-CNRs were ground to fine powders.

5.2.2 Physicochemical Characterizations

The morphologies of samples synthesized from each step were imaged using a Philips CM10 transmission electron microscope (TEM). In particular, CNC was imaged with a JEM-2100 high-resolution TEM (HRTEM) and the sample was stained with 2% (w/w) uranyl acetate negative stain for high-resolution imaging. The mass loading of MF coating in the composite material of MFCNCs was determined by thermal gravimetric analysis (TGA) where samples were heated from 25 to 800 ℃ at a heating rate of 10 ℃ min-1 under 10 ml min-1 N_2 flow. The functional groups of CNC, MFCNC, and N-CNR was characterized by FT-IR (PerkinElmer 1720 FT-IR spectrometer). For sample preparation, freeze-dried samples were mixed with KBr and then compressed into pellets for measurements at a resolution of 4 cm^{-1}. X-ray photoelectron spectroscopy (XPS) was conducted to determine the surface composition of the composite material using a Thermal Scientific K-Alpha XPS spectrometer.

5.2.3 Electrochemical Characterizations

The ORR activity of the catalyst is investigated with a rotating disc electrode (RDE) half-cell that consists of a catalyst coated glass carbon electrode (GCE) as working electrode, a graphite rod as contour electrode and a reversible hydrogen electrode (RHE) as the

reference electrode. Typical catalyst ink is the homogeneously sonicated mixture of 10 mg of N-CNR catalyst, 750 μL isopropanol (IPA) and 250 μL 0.25% Nafion IPA solution. A portion of 16 μL of ink is dropped on the surface of GCE, achieving a catalyst loading of 0.6 mg cm-2. All the electrochemical experiments were performed on a computer-controlled bipotentiostat (Pine Instrument Company, USA) at room temperature. Cyclic voltammetry (CV) curves were recorded with a scan rate of 50 mV s^{-1} in the O_2/N_2 saturated 0.1 mol L^{-1} KOH while steady-state ORR polarization curves were curves obtained with linear staircase voltammetry (LCSV) under different rotation speed in the O_2 saturated electrolyte.

5.3 Results and Discussion

The synthesis of N-MFCNC is illustrated in **Figure 5-1**. MF precursor was first well mixed with CNCs followed polymerization and condensation on the surface of CNCs into MF resin coating. The well-dispersed core-shell structured hybrid particles are successfully formed and imaged in **Figure 5-2b**. Compared with the pristine CNC shown in **Figure 5-2a**, the surface of MFCNC less defined due to the amorphous polymer coating. MFCNCs also appear thicker than CNCs in diameter, from which the layer of MF coating can be roughly measured to be around 19 nm. The good water dispersibility, high surface area, and high aspect ratio make CNC a nice template to support the polycondensation of MF layer with the defined shape. MF resin is a highly cross-linked porous network that is expected to render the desired porosity in the carbon structure after pyrolysis. It is also very high in N content, suitable as N-precursor for desirable doping content. To further confirm the presence of MF in the MFCNC system, FTIR spectra were acquired and compared with those of MFCNC and CNC (**Figure 5-3**). Several peaks in the MFCNC spectrum are absent in the CNC

spectrum. The new peaks are due to the 1, 3, 5-triazine ring (at 1556 and 812 cm^{-1}) and the methylene C-H bending vibration (at 1330 cm^{-1}) of melamine.[23]

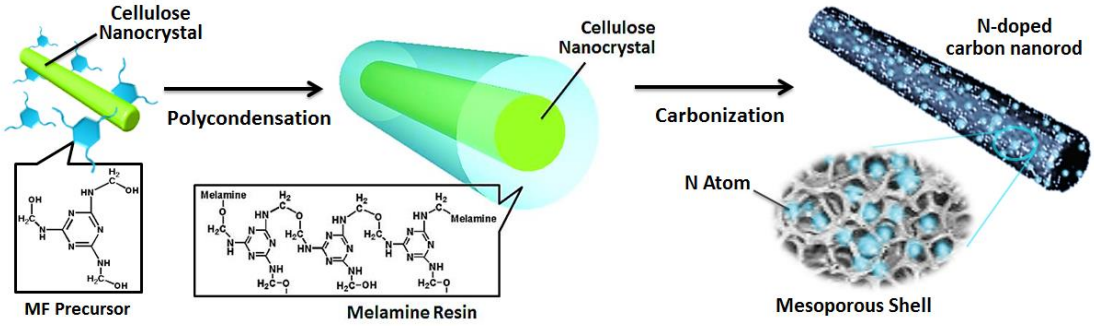

Figure 5- 1 Schematic of the synthesis of nitrogen-doped carbon nanorods.

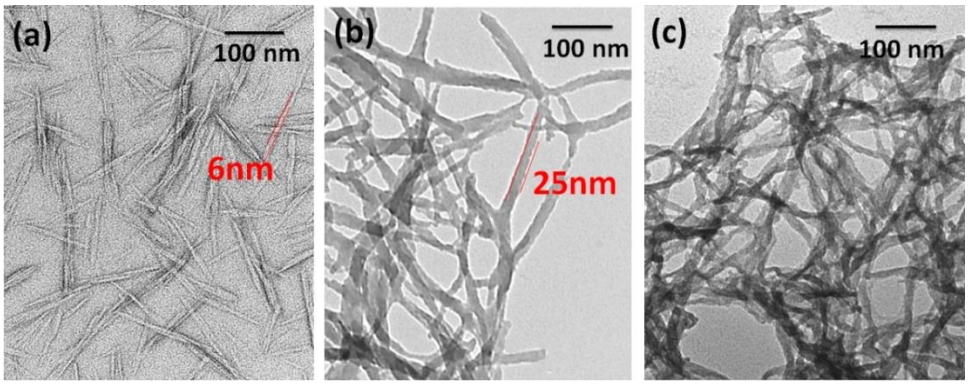

Figure 5- 2 TEM images for (a) pristine CNCs, (b) MFCNCs and (c) N-CNR

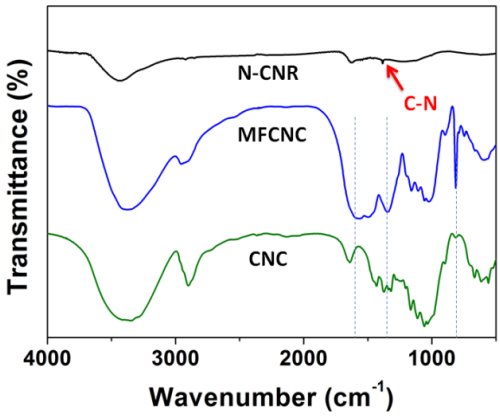

Figure 5- 3 FTIR spectra for pristine CNC, MFCNC, and N-CNR samples.

In the second step, the hybrid material of MFCNC was paralyzed at 900 degrees under

the inert atmosphere to ensure sufficient graphitization. TEM image in **Figure 5-2c** shows the well-preserved fibrous morphology for the N-CNR with a slight shrinkage in diameter. The fibrous morphology allows the full potential of catalytic activity to be explored due to the highly exposed surface area and pore sites. Compared with the FT-IR spectra of MFCNC, most of the adsorption peaks diminished for N-CNR due to loss of functional groups during carbonization. A new peak, however, was shown at around 1381 nm^{-1}, representing C-N stretch, indicating the successful N doping in the carbon frame. Similar peak was also observed for N-doped graphene and N-doped carbon dots in other works.[140, 164]

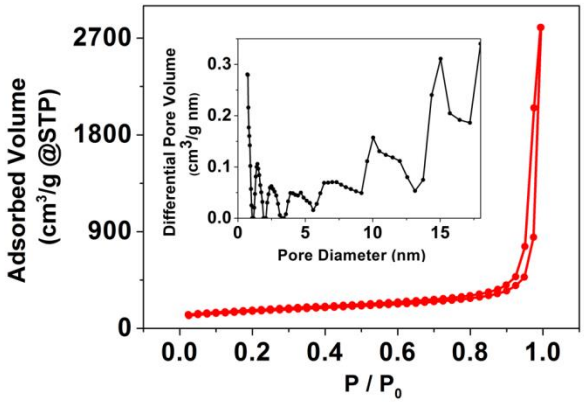

Figure 5- 4 N_2 adsorption/desorption isotherms with inset showing the corresponding pore size distribution for N-CNR.

Table 5- 1 Summary of the composition information from elemental analysis, surface area and pore properties from BET measurement for MFCNC and N-CNR samples.

	N(%wt)	C (%wt)	BET Surface Area ($m^2 g^{-1}$)	Total Pore Volume ($cm^3 g^{-1}$)	Mean Pore Diameter (nm)
MFCNC	34.73	38.09	212.8	0.07	1.34
N-CNR	8.45	75.53	564.2	2.03	1.65

The effect of carbonization on the composition of the MFCNC was carefully investigated.

Table 5-1 summarizes the composition from the elemental analysis for MFCNC before and after carbonization. An effective nitrogen doping using MF coating strategy was confirmed with nitrogen content reaching 8.45%. Pore size distribution (PSD) curves and isotherms were further performed to characterize the pore structure and surface area of the obtained N-CNRs since these properties are also pivotal for the catalytic performance. The isotherms of N-CNR in **Figure 5-4** exhibited the representative type III behavior defined by IUPAC with an H_3 type hysteresis loop. The sharp capillary condensation step at high relative pressures $P/P_0 > 0.90$ suggests the existence of large mesopores and macropores. The result agrees well with the PSD characterization, where it shows that pores are well developed throughout mesopore region. From the measurement, N-CNR possessed a high specific surface area of 564.2 $m^2 g^{-1}$, as well as a desirable mesoporous structure with a mean diameter of 1.65 nm and a high pore volume of 2.03 $cm^3 g^{-1}$. This is expected to be rather beneficial for the enhanced catalytic activity due to favorable contact with the reactants.

ORR is an essential reaction existed in many energy conversion and storage devices such as fuel cells[140, 141, 163, 164], metal-air batteries[267-269]. However, without the assistance of catalyst, the sluggish ORR could not proceed effectively, efficiently and practically in the aforementioned devices. Since heteroatoms doped carbon materials were proved to be one series of effective ORR catalysts, herein the N-CNR was evaluated electrochemically for ORR. As displayed in **Figure 5-5a**, CV was first conducted for N-CNR under both N_2 and O_2 saturated electrolyte. The typical quasi-rectangular shape of the profile is obtained in the presence of N_2 whilst a significant redox peak with a current density of 1.23 mA cm^{-2} at 0.7V vs RHE is observed with oxygen bubbling in the electrolyte, clearly indicating the

capability of N-CNR to catalyze ORR. Polarization curves of N-CNR under different rotation speeds were also recorded by RDE and illustrated in **Figure 5-5b**. The polarization curves of N-CNR under 900 rpm shows the on-set potential of 0.87V and half-wave potential of 0.73V, indicating its decent ORR activity. Moreover, the high diffusion-limited current density (4.21 mA cm^{-2}) is comparable to the commercial Pt/C catalyst in the literature[140], which may relate to fast diffusion of reactants via the high surface area of N-CNR. The associated Koutecky-Levich plot is depicted via the reciprocal of measured current density against the reciprocal of the square root of rotation rate in **Figure 5-5c**. The number of transferred electrons of N-CNR could reach 3.83 (**Figure 5-5c**, insert), suggesting quasi four-electron reduction pathway dominates the reaction. The Tafel plot is also presented to analyze the ORR activity of N-CNR (**Figure 5-5d**). The Tafel slope is read as 66 mV dec^{-1} at the low overpotential region, where the ORR reaction is mainly controlled by the kinetic reaction on the surface of N-CNR, is similar to the reported values of N-doped graphene or CNT in the literature.[141, 163, 164, 268] This could be attributed to the change of the electron cloud density on the carbon structure with the introduction of nitrogen doping[164]. Based on the analysis of the high-resolution spectrum of N 1s (**Figure 5-6**), four different nitrogen species could be identified, namely pyridinic (398 eV), pyrrolic (399.9 eV), graphitic (400.9 eV) and oxide (402.8 eV). Among them, pyridinic and graphitic nitrogen are dramatically related to the ORR activity[19, 140, 141, 164, 269], especially the adjacent carbon atoms to pyridinic nitrogen are considered as the major active site in N-doped carbon materials[19]. Therefore, the nitrogen composition with high ratios of pyridinic (36%) and graphitic (34%) nitrogen explains the high ORR activity of N-CNR. Besides, high BET surface area with meso-porous structure benefits the accessibility of active sites as well as

the diffusion of reactants in the N-CNR[163, 164], which mainly relates to the activity at the diffusion controlled region with high over potential in **Figure 5-5b**. To sum, N-CNR demonstrates decent ORR activity in the alkaline electrolyte.

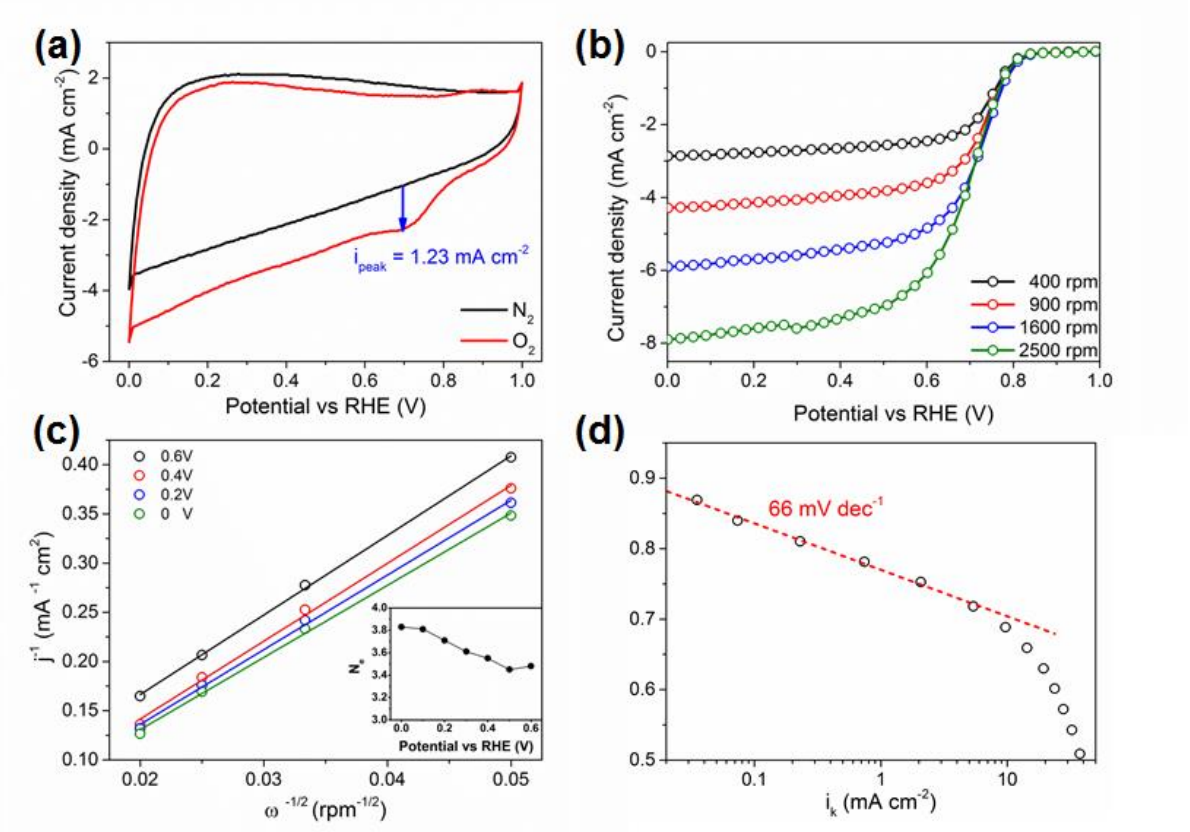

Figure 5- 5 ORR performance of N-CNR: (a) CV curves under both N_2 and O_2 saturated 0.1 mol L^{-1} KOH; (b) LSV curves under different rotating speeds; (c) K–L plots under different potential vs RHE with transferred number of electrons (insert plot); (d) Tafel plot.

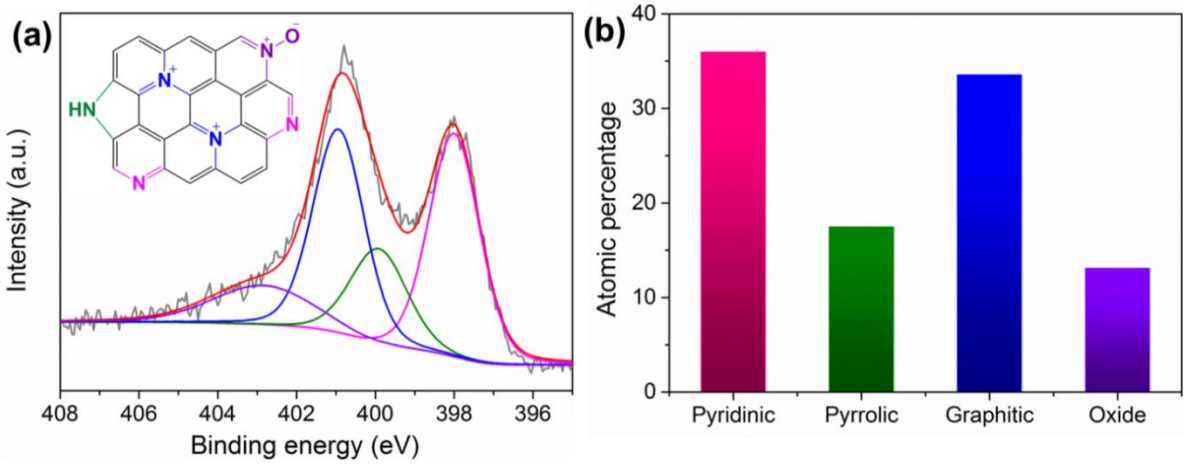

Figure 5- 6 (a) High-resolution XPS spectrum of N 1s and the structure of different nitrogen species; (b) composition of nitrogen species in N-CNR.

5.4 Conclusions

In conclusion, novel N-doped mesoporous carbon nanorods were developed using abundant and renewable carbon source, cost-effective synthesis, and easily accessible apparatus. Core-shell structured MFCNC with a rather smooth surface validates the homogeneous coating of MF templated by CNCs. The strategy of MF functionalization introduces efficient N-doping, mesoporosity as well as the critical stabilizing effect for the fibrous-structure of N-CNR through one-step pyrolysis. The prepared N-CNR demonstrated promising catalytic activity towards the electrocatalytic reaction of ORR. The superior catalytic performance is mainly attributed to the high N-doping content introducing abundant active sites, as well as high surface area mesoporous structure leading to high accessibility of active sites and efficient reactant transfer and diffusion.

Chapter 6: Conclusions and Future Work

6.1 Summary and conclusions

To develop low-cost non-precious metal catalysts with high ORR activity and stability for fuel cell applications, various experiments were conducted to synthesize one M-N-C catalyst and two metal-free catalysts towards ORR. The first special M-N-C catalyst was a novel N, S-co-doped Fe-N-C catalyst which was successfully fabricated and evaluated for ORR activity and durability as well as the single cell performance in a real H_2-air PEMFC. The first metal-free catalyst was prepared in a special methodology and in the shape of carbon film which was proved to be a true metal-free catalyst. The last study applied the extreme low-cost biomass precursor, cellulose, to fabricate the metal-free catalyst and lower the price of ORR catalyst in further.

In Chapter 3, a novel N, S-co-doped Fe-N-C catalyst was successfully synthesized from the high temperature treated composite of *in-situ* polymerized novel N, S-co-existed precursor, polyrhodanine (PRh) on the acid treated carbon black via the initiation of $FeCl_3$. The Fe-N-C catalyst was obtained after a two-step heat-treatment process and an acid-leaching step in between. This catalyst demonstrated excellent ORR activity, bearing a half-wave potential of 0.77 V vs RHE in the acidic electrolyte and excellent H_2-air PEMFC performance, ranking the obtained peak power density 386 mW cm^{-2} at 0.46 V among the best reported NMPC catalyst in H_2-air PEMFC in the world. Also, it tends to catalyze the oxygen reduction via four electron pathway according to its number of transferred electrons (>3.94) and low peroxide yield (< 2.8 %). Moreover, it also demonstrated excellent

durability, showing only 32 mV downshift after 5000 potential sweep cycles in the ADT tests. Meanwhile, with the assistance of different characterization techniques and the comparison with an S-free nitrogen precursor (polypyrrole, PPy), the roles of sulfur in this N, S-co-doped Fe-N-C were unveiled. Sulfur can benefit the ORR activity and durability of FePRh-HT2 catalyst regarding morphology, active sites density as well as the molecular structure of active sites. Firstly, in the presence of sulfur, FeS nanoparticles were formed during pyrolysis and they function as the macro- and meso-pore agents to enhance the BET surface area in addition to the mass diffusion after acid leaching. Secondly, the formation of FeS during the pyrolysis inhibited the formation of Fe_3C and facilitated the formation of the Fe-Nx active sites, resulting in higher active sites density and TOF of FePRh-HT2 as opposed to FePPy-HT2. Thirdly, the sulfur-doped Fe-N_4 active site structure demonstrates a better affinity to O_2 molecule when compared to the Fe-N_4 active site structure in the DFT calculation, which is in good agreement with the better ORR stability of the FePRh-HT2 catalyst. Therefore, the multi-functionality of sulfur from the precursor PRh endows this N, S-co-doped NPMC with high ORR activity and durability.

In Chapter 4, to further decrease the cost of NPMC, simplification of the fabrication process and to check the true nature of metal-free catalysts, a series of highly porous free-standing metal-free catalysts were successfully prepared via the solution casting methodology followed by annealing the porous PBI-Py membrane at high temperature. The obtained catalyst is truly metal-free owing to the intentional avoidance of the introduction of transition metals and metal-contaminated material like graphene oxide or commercial carbon black and CNT. By tuning the amount of pore agent, DBP in the casting solution, the pores and surface area of the specific 3D nano-network structure in final catalyst could be adjusted,

producing a specific surface area as high as 902 m^2 g^{-1} for 95%PBI-Py-1000. RDEd tests also disclosed that high porosity and high annealing temperature could improve the ORR activity greatly in both acidic and alkaline electrolyte. The optimal catalyst, 95%PBI-Py-1000 demonstrates comparable activity ($E_{1/2}$ = 0.82 V vs. RHE) and durability to commercial Pt/C catalyst in alkaline electrolyte and superior methanol tolerance to that of commercial Pt/C catalyst. The results not only suggest PBI-Py as a decent nitrogen precursor for metal-free catalysts, but also indicate that the solution casting methodology as a feasible methodology for NPMC fabrication.

In Chapter 5, biomass precursor, cellulose nanocrystals (CNC) were applied to develop N-doped mesoporous carbon nanorods as the metal-free catalysts to introduce another level of environmental-benignity and low cost to the catalyst. With a smooth coating of MF on the surface of CNC, the MFCNC derived fibrous-structure of mesoporous nitrogen-doped carbon nanorods, N-CNR were obtained via one-step pyrolysis. The decent catalytic activity towards ORR in the alkaline electrolyte is mainly attributed to the high N-doping content as well as the high surface area, resulting in high accessible active site density.

As a result, the contributions of this work are summarized as follows:

1. Novel N, S-co-doped Fe-N-C catalyst with high ORR activity, durability and H_2-air performance was prepared and reported for the first time via novel N, S-containing precursor such as polyrhodanine (PRh).
2. It is the first-ever work showing the introduction of sulfur in nitrogen precursor increases the ORR activity of Fe-N-C catalyst not only indirectly via tuning the synthetic chemistry towards the enhancement of active sites density and the

accessibility to them, but also directly via the doping into the chemical structure of the active site.

3. It is also the first time solution casted porous membrane was used to fabricate free-standing NPMC.
4. Both PBI-Py and earth-abundant biomass cellulose nanocrystals were converted into nitrogen doped carbon materials to decently catalyze ORR as metal-free catalysts.
5. The cost of ORR catalyst could be reduced via using N, S-co-doped Fe-N-C catalyst in the acidic electrolyte and could be further decreased by the application of PBI-Py and even cellulose derived metal-free catalysts in the alkaline condition.

6.2 Proposed future work

Based on the findings of these studies, some future directions for the catalysts research could be suggested:

1. Heteroatoms doping for NPMC

   The introduction of heteroatoms, such as S, P, and B to the synthesis of NPMCs were encouraged. According to the FePRh project in Chapter 3, it was clear that co-existed sulfur atoms could significantly enhance both ORR activity and durability. Thus, the similar doping of P and B could also tune the ORR activity M-N-C catalysts. Prior to the development of P or B doped M-N-C catalysts, it is necessary to investigate the effects of different sulfur precursors on the M-N-C catalysts, as sulfur appeared in many different oxidation states which in return could affect the chemical environment during the high-temperature treatment. Also, it should be investigated whether a separate sulfur precursor could be used to attain decent ORR activity. To follow, this new sulfur precursor could be utilized to couple

with different high-performance nitrogen precursor at different ratios to maximize the ORR performance. After that, P and/or B precursor with similar chemical structure to the S-analogue could be introduced to investigate its heteroatom doping effects on the ORR activity and durability of M-N-C catalysts. Likewise, the heteroatom-doping could also be introduced for the development of metal-free catalysts derived from either polymer precursors or biomass precursors.

2. Free-standing catalyst layer

    As introduced in Chapter 4, a new method based on solution casted porous membrane is successfully developed for the fabrication of free-standing catalyst layer. This method followed the idea of all-in-one and it shall be tested in multiple electrochemical devices to diversify its potential use, such as Zn-air fuel cell/battery, minimized fuel cell device and so on. Different polymer precursors, nitrogen and/or heteroatom small molecule additives, as well as metal precursors could then be introduced and investigated to further enhance the ORR performance, especially in the acidic electrolyte.

3. Biomass precursors

    It was proved that biomass precursors could be utilized to synthesize low-cost metal-free catalysts according to Chapter 5. Then, it shall also be feasible to use certain biomass precursors with transition metal precursors to synthesize M-N-C catalysts. The proper choice of biomass precursors, such as N, S-contained bio-waste materials, could be used to obtain highly active and durable M-N-C catalysts, even in the acidic electrolyte, with ultralow cost.

References

1. Bi, E.; Chen, H.; Yang, X.; Peng, W.; Grätzel, M.; Han, L. A quasi core–shell nitrogen-doped graphene/cobalt sulfide conductive catalyst for highly efficient dye-sensitized solar cells. *Energy & Environmental Science* 2014, 7, 2637-2641.
2. Higgins, D.; Zamani, P.; Yu, A.; Chen, Z. The application of graphene and its composites in oxygen reduction electrocatalysis: a perspective and review of recent progress. *Energy & Environmental Science* 2016, 9, 357-390.
3. Jiao, Y.; Zheng, Y.; Jaroniec, M.; Qiao, S. Z. Origin of the electrocatalytic oxygen reduction activity of graphene-based catalysts: a roadmap to achieve the best performance. *Journal of the American Chemical Society* 2014, 136, 4394-4403.
4. Eberle, U.; Müller, B.; Von Helmolt, R. Fuel cell electric vehicles and hydrogen infrastructure: status 2012. *Energy & Environmental Science* 2012, 5, 8780-8798.
5. Chen, Z.; Higgins, D.; Yu, A.; Zhang, L.; Zhang, J. A review on non-precious metal electrocatalysts for PEM fuel cells. *Energy & Environmental Science* 2011, 4, 3167-3192.
6. Sinha, J.; Lasher, S.; Yang, Y.; Kopf, P. Direct hydrogen PEMFC manufacturing cost estimation for automotive applications. *Fuel Cell Tech Team Review* 2008.
7. Debe, M. K. Electrocatalyst approaches and challenges for automotive fuel cells. *Nature* 2012, 486, 43-51.
8. Wu, J.; Yuan, X. Z.; Martin, J. J.; Wang, H.; Zhang, J.; Shen, J.; Wu, S.; Merida, W. A review of PEM fuel cell durability: Degradation mechanisms and mitigation strategies. *J Power Sources* 2008, 184, 104-119.
9. Zhang, L.; Zhang, J.; Wilkinson, D. P.; Wang, H. Progress in preparation of non-noble electrocatalysts for PEM fuel cell reactions. *J Power Sources* 2006, 156, 171-182.
10. Bezerra, C. W. B.; Zhang, L.; Lee, K.; Liu, H.; Marques, A. L. B.; Marques, E. P.; Wang, H.; Zhang, J. A review of Fe-N/C and Co-N/C catalysts for the oxygen reduction reaction. *Electrochim Acta* 2008, 53, 4937-4951.

11. Borup, R.; Meyers, J.; Pivovar, B.; Kim, Y. S.; Mukundan, R.; Garland, N.; Myers, D.; Wilson, M.; Garzon, F.; Wood, D. Scientific aspects of polymer electrolyte fuel cell durability and degradation. *Chemical reviews* 2007, 107, 3904-3951.

12. Bu, L.; Zhang, N.; Guo, S.; Zhang, X.; Li, J.; Yao, J.; Wu, T.; Lu, G.; Ma, J.-Y.; Su, D. Biaxially strained PtPb/Pt core/shell nanoplate boosts oxygen reduction catalysis. *Science* 2016, 354, 1410-1414.

13. Stamenkovic, V. R.; Fowler, B.; Mun, B. S.; Wang, G.; Ross, P. N.; Lucas, C. A.; Marković, N. M. Improved oxygen reduction activity on Pt3Ni (111) via increased surface site availability. *Science* 2007, 315, 493-497.

14. Chen, C.; Kang, Y.; Huo, Z.; Zhu, Z.; Huang, W.; Xin, H. L.; Snyder, J. D.; Li, D.; Herron, J. A.; Mavrikakis, M. Highly crystalline multimetallic nanoframes with three-dimensional electrocatalytic surfaces. *Science* 2014, 343, 1339-1343.

15. Jasinski, R. A new fuel cell cathode catalyst. 1964.

16. Wu, G.; More, K. L.; Johnston, C. M.; Zelenay, P. High-Performance Electrocatalysts for Oxygen Reduction Derived from Polyaniline, Iron, and Cobalt. *Science* 2011, 332, 443-447.

17. Lefèvre, M.; Proietti, E.; Jaouen, F.; Dodelet, J.-P. Iron-based catalysts with improved oxygen reduction activity in polymer electrolyte fuel cells. *Science* 2009, 324, 71-74.

18. DOE. Technical Plan - Fuel Cells. http://www1.eere.energy.gov/hydrogenandfuelcells/mypp/pdfs/fuel_cells.pdf.

19. Guo, D.; Shibuya, R.; Akiba, C.; Saji, S.; Kondo, T.; Nakamura, J. Active sites of nitrogen-doped carbon materials for oxygen reduction reaction clarified using model catalysts. *Science* 2016, 351, 361-365.

20. Gong, K.; Du, F.; Xia, Z.; Durstock, M.; Dai, L. Nitrogen-doped carbon nanotube arrays with high electrocatalytic activity for oxygen reduction. *Science* 2009, 323, 760-764.

21. Adler, S. B. Fuel cells: current status and future challenges. *Frontiers of Engineering: Reports on* 2006.

22. Cook, B. Introduction to fuel cells and hydrogen technology. *Engineering Science & Education Journal* 2002, 11, 205-216.

23. Larminie, J.; Dicks, A.; McDonald, M. S. *Fuel cell systems explained*. Wiley New York: 2003; Vol. 2.

24. Hoogers, G. *Fuel cell technology handbook*. CRC press: 2002.

25. Shah, R. Introduction to fuel cells. In *Recent Trends in Fuel Cell Science and Technology*, Springer: 2007; pp 1-9.

26. Mehta, V.; Cooper, J. S. Review and analysis of PEM fuel cell design and manufacturing. *Journal of Power Sources* 2003, 114, 32-53.

27. Zhou, X.; Qiao, J.; Yang, L.; Zhang, J. A Review of Graphene‐Based Nanostructural Materials for Both Catalyst Supports and Metal‐Free Catalysts in PEM Fuel Cell Oxygen Reduction Reactions. *Advanced Energy Materials* 2014, 4.

28. Millichamp, J.; Mason, T. J.; Neville, T. P.; Rajalakshmi, N.; Jervis, R.; Shearing, P. R.; Brett, D. J. Mechanisms and effects of mechanical compression and dimensional change in polymer electrolyte fuel cells–a review. *Journal of Power Sources* 2015, 284, 305-320.

29. Jasinski, R. New Fuel Cell Cathode Catalyst. *Nature* 1964, 201, 1212-&.

30. Liu, Y.; Ishihara, A.; Mitsushima, S.; Kamiya, N.; Ota, K.-i. Transition metal oxides as DMFC cathodes without platinum. *Journal of The Electrochemical Society* 2007, 154, B664-B669.

31. Huang, K.; Bi, K.; Xu, J.; Liang, C.; Lin, S.; Wang, W.; Yang, T.; Du, Y.; Zhang, R.; Yang, H. Novel graphite-carbon encased tungsten carbide nanocomposites by solid-state reaction and their ORR electrocatalytic performance in alkaline medium. *Electrochimica Acta* 2015, 174, 172-177.

32. Dong, Y.; Deng, Y.; Zeng, J.; Song, H.; Liao, S. A high-performance composite ORR catalyst based on the synergy between binary transition metal nitride and nitrogen-doped reduced graphene oxide. *Journal of Materials Chemistry A* 2017, 5, 5829-5837.

33. Shen, M.; Ruan, C.; Chen, Y.; Jiang, C.; Ai, K.; Lu, L. Covalent entrapment of cobalt–iron sulfides in N-doped mesoporous carbon: Extraordinary bifunctional electrocatalysts for oxygen reduction and evolution reactions. *ACS applied materials & interfaces* 2015, 7, 1207-1218.

34. Li, H.; Gao, D.; Cheng, X. Simple microwave preparation of high activity Se-rich CoSe 2/C for oxygen reduction reaction. *Electrochimica Acta* 2014, 138, 232-239.

35. Higgins, D.; Hassan, F.; Seo, M.; Choi, J.; Hoque, M.; Lee, D.; Chen, Z. Shape-controlled octahedral cobalt disulfide nanoparticles supported on nitrogen and sulfur-doped graphene/carbon nanotube composites for oxygen reduction in acidic electrolyte. *Journal of Materials Chemistry A* 2015, 3, 6340-6350.

36. Bashyam, R.; Zelenay, P. A class of non-precious metal composite catalysts for fuel cells. *Nature* 2006, 443, 63-66.

37. Millán, W. M.; Thompson, T. T.; Arriaga, L.; Smit, M. A. Characterization of composite materials of electroconductive polymer and cobalt as electrocatalysts for the oxygen reduction reaction. *International Journal of Hydrogen Energy* 2009, 34, 694-702.

38. Shui, J.; Chen, C.; Grabstanowicz, L.; Zhao, D.; Liu, D.-J. Highly efficient nonprecious metal catalyst prepared with metal–organic framework in a continuous carbon nanofibrous network. *Proceedings of the National Academy of Sciences* 2015, 112, 10629-10634.

39. Jaouen, F.; Proietti, E.; Lefèvre, M.; Chenitz, R.; Dodelet, J.-P.; Wu, G.; Chung, H. T.; Johnston, C. M.; Zelenay, P. Recent advances in non-precious metal catalysis for oxygen-reduction reaction in polymer electrolyte fuel cells. *Energy & Environmental Science* 2011, 4, 114-130.

40. Fu, X.; Choi, J.-Y.; Zamani, P.; Jiang, G.; Hoque, M. A.; Hassan, F. M.; Chen, Z. Co–N decorated hierarchically porous graphene aerogel for efficient oxygen reduction reaction in acid. *ACS applied materials & interfaces* 2016, 8, 6488-6495.

41. Fu, X.; Zamani, P.; Choi, J. Y.; Hassan, F. M.; Jiang, G.; Higgins, D. C.; Zhang, Y.; Hoque, M. A.; Chen, Z. In Situ Polymer Graphenization Ingrained with Nanoporosity in a Nitrogenous Electrocatalyst Boosting the Performance of Polymer‐Electrolyte‐Membrane Fuel Cells. *Advanced Materials* 2017, 29.

42. Zamani, P.; Higgins, D. C.; Hassan, F. M.; Fu, X.; Choi, J.-Y.; Hoque, M. A.; Jiang, G.; Chen, Z. Highly active and porous graphene encapsulating carbon nanotubes as a non-precious oxygen reduction electrocatalyst for hydrogen-air fuel cells. *Nano Energy* 2016, 26, 267-275.

43. Jahnke, H.; Schönborn, M.; Zimmermann, G. Organic dyestuffs as catalysts for fuel cells. *Physical and chemical applications of dyestuffs* 1976, 133-181.

44. Gupta, S.; Tryk, D.; Bae, I.; Aldred, W.; Yeager, E. Heat-treated polyacrylonitrile-based catalysts for oxygen electroreduction. *Journal of applied electrochemistry* 1989, 19, 19-27.

45. Kattel, S.; Atanassov, P.; Kiefer, B. Density functional theory study of the oxygen reduction reaction mechanism in a BN co-doped graphene electrocatalyst. *Journal of Materials Chemistry A* 2014, 2, 10273-10279.

46. Kattel, S.; Atanassov, P.; Kiefer, B. Stability, electronic and magnetic properties of in-plane defects in graphene: A first-principles study. *The Journal of Physical Chemistry C* 2012, 116, 8161-8166.

47. Zitolo, A.; Goellner, V.; Armel, V.; Sougrati, M.-T.; Mineva, T.; Stievano, L.; Fonda, E.; Jaouen, F. Identification of catalytic sites for oxygen reduction in iron-and nitrogen-doped graphene materials. *Nature materials* 2015, 14, 937-942.

48. Tylus, U.; Jia, Q.; Strickland, K.; Ramaswamy, N.; Serov, A.; Atanassov, P.; Mukerjee, S. Elucidating oxygen reduction active sites in pyrolyzed metal–nitrogen coordinated non-precious-metal electrocatalyst systems. *The Journal of Physical Chemistry C* 2014, 118, 8999-9008.

49. Meng, H.; Larouche, N.; Lefevre, M.; Jaouen, F.; Stansfield, B.; Dodelet, J. P. Iron porphyrin-based cathode catalysts for polymer electrolyte membrane fuel cells: Effect of NH3 and Ar mixtures as pyrolysis gases on catalytic activity and stability. *Electrochim Acta* 2010, 55, 6450-6461.

50. Li, W. M.; Yu, A. P.; Higgins, D. C.; Llanos, B. G.; Chen, Z. W. Biologically Inspired Highly Durable Iron Phthalocyanine Catalysts for Oxygen Reduction Reaction in Polymer Electrolyte Membrane Fuel Cells. *J Am Chem Soc* 2010, 132, 17056-17058.

51. Palaniselvam, T.; Kannan, R.; Kurungot, S. Facile construction of non-precious iron nitride-doped carbon nanofibers as cathode electrocatalysts for proton exchange membrane fuel cells. *Chem Commun* 2011, 47, 2910-2912.

52. Ohms, D.; Herzog, S.; Franke, R.; Neumann, V.; Wiesener, K.; Gamburcev, S.; Kaisheva, A.; Iliev, I. Influence of metal ions on the electrocatalytic oxygen reduction of carbon materials prepared from pyrolyzed polyacrylonitrile. *J Power Sources* 1992, 38, 327-334.

53. Widelöv, A.; Larsson, R. ESCA and electrochemical studies on pyrolysed iron and cobalt tetraphenylporphyrins. *Electrochim Acta* 1992, 37, 187-197.

54. Jiang, R.; Chu, D. Remarkably active catalysts for the electroreduction of O 2 to H 2 O for use in an acidic electrolyte containing concentrated methanol. *J Electrochem Soc* 2000, 147, 4605-4609.

55. Maruyama, J.; Abe, I. Fuel cell cathode catalyst with heme-like structure formed from nitrogen of glycine and iron. *J Electrochem Soc* 2007, 154, B297-B304.

56. Chu, D.; Jiang, R. Novel electrocatalysts for direct methanol fuel cells. *Solid State Ionics* 2002, 148, 591-599.

57. Lee, K.; Zhang, L.; Lui, H.; Hui, R.; Shi, Z.; Zhang, J. Oxygen reduction reaction (ORR) catalyzed by carbon-supported cobalt polypyrrole (Co-PPy/C) electrocatalysts. *Electrochimica Acta* 2009, 54, 4704-4711.

58. Manzoli, M.; Monte, R. D.; Boccuzzi, F.; Coluccia, S.; Kašpar, J. CO oxidation over CuO< sub> x</sub>-CeO< sub> 2</sub>-ZrO< sub> 2</sub> catalysts: Transient behaviour and role of copper clusters in contact with ceria. *Applied Catalysis B: Environmental* 2005, 61, 192-205.

59. He, P.; Lefevre, M.; Faubert, G.; Dodelet, J. Oxygen reduction catalysts for polymer electrolyte fuel cells from the pyrolysis of various transition metal acetates adsorbed on 3, 4, 9, 10-perylenetetracarboxylic dianhydride. *Journal of new materials for electrochemical systems* 1999, 2, 243-252.

60. Sawai, K.; Suzuki, N. Heat-treated transition metal hexacyanometallates as electrocatalysts for oxygen reduction insensitive to methanol. *J Electrochem Soc* 2004, 151, A682-A688.

61. Matter, P. H.; Zhang, L.; Ozkan, U. S. The role of nanostructure in nitrogen-containing carbon catalysts for the oxygen reduction reaction. *J Catal* 2006, 239, 83-96.

62. Sahraie, N. R.; Kramm, U. I.; Steinberg, J.; Zhang, Y.; Thomas, A.; Reier, T.; Paraknowitsch, J.-P.; Strasser, P. Quantifying the density and utilization of active sites in non-precious metal oxygen electroreduction catalysts. *Nature communications* 2015, 6.

63. Domínguez, C.; Pérez-Alonso, F.; Salam, M. A.; De La Fuente, J. G.; Al-Thabaiti, S.; Basahel, S.; Peña, M.; Fierro, J.; Rojas, S. Effect of transition metal (M: Fe, Co or Mn) for

the oxygen reduction reaction with non-precious metal catalysts in acid medium. *International Journal of Hydrogen Energy* 2014, 39, 5309-5318.

64. ZHANG, R.; ZHANG, J.; Fei, M.; WANG, W.-y.; LI, R.-f. Preparation of Mn-NC catalyst and its electrocatalytic activity for the oxygen reduction reaction in alkaline medium. *Journal of Fuel Chemistry and Technology* 2014, 42, 467-475.

65. Kinoshita, K. *Carbon: Electrochemical and Physicochemical Properties*. Wiley: 1988.

66. Marsh, H.; Warburton, A. Catalysis of graphitisation. *Journal of Applied Chemistry* 1970, 20, 133-142.

67. Kramm, U. I.; Herrmann-Geppert, I.; Fiechter, S.; Zehl, G.; Zizak, I.; Dorbandt, I.; Schmeißer, D.; Bogdanoff, P. Effect of iron-carbide formation on the number of active sites in Fe–N–C catalysts for the oxygen reduction reaction in acidic media. *Journal of Materials Chemistry A* 2014, 2, 2663-2670.

68. Ranjbar Sahraie, N.; Paraknowitsch, J. P.; Göbel, C.; Thomas, A.; Strasser, P. Noble-metal-free electrocatalysts with enhanced ORR performance by task-specific functionalization of carbon using ionic liquid precursor systems. *Journal of the American Chemical Society* 2014, 136, 14486-14497.

69. Yuan, X.; Ding, X.-L.; Wang, C.-Y.; Ma, Z.-F. Use of polypyrrole in catalysts for low temperature fuel cells. *Energy & Environmental Science* 2013, 6, 1105-1124.

70. Xiao, M.; Zhu, J.; Feng, L.; Liu, C.; Xing, W. Meso/Macroporous Nitrogen‐Doped Carbon Architectures with Iron Carbide Encapsulated in Graphitic Layers as an Efficient and Robust Catalyst for the Oxygen Reduction Reaction in Both Acidic and Alkaline Solutions. *Advanced Materials* 2015, 27, 2521-2527.

71. Wang, Y. C.; Lai, Y. J.; Song, L.; Zhou, Z. Y.; Liu, J. G.; Wang, Q.; Yang, X. D.; Chen, C.; Shi, W.; Zheng, Y. P. S‐Doping of an Fe/N/C ORR Catalyst for Polymer Electrolyte Membrane Fuel Cells with High Power Density. *Angewandte Chemie* 2015, 127, 10045-10048.

72. Zhu, Y.; Zhang, B.; Liu, X.; Wang, D. W.; Su, D. S. Unravelling the structure of electrocatalytically active Fe–N complexes in carbon for the oxygen reduction reaction. *Angewandte Chemie International Edition* 2014, 53, 10673-10677.

73. Niu, W.; Li, L.; Liu, X.; Wang, N.; Liu, J.; Zhou, W.; Tang, Z.; Chen, S. Mesoporous N-doped carbons prepared with thermally removable nanoparticle templates: an efficient electrocatalyst for oxygen reduction reaction. *Journal of the American Chemical Society* 2015, 137, 5555-5562.

74. Strickland, K.; Miner, E.; Jia, Q.; Tylus, U.; Ramaswamy, N.; Liang, W.; Sougrati, M.-T.; Jaouen, F.; Mukerjee, S. Highly active oxygen reduction non-platinum group metal electrocatalyst without direct metal-nitrogen coordination. *Nature communications* 2015, 6.

75. Kramm, U. I.; Lefèvre, M.; Larouche, N.; Schmeisser, D.; Dodelet, J.-P. Correlations between Mass Activity and Physicochemical Properties of Fe/N/C Catalysts for the ORR in PEM Fuel Cell via 57Fe Mössbauer Spectroscopy and Other Techniques. *Journal of the American Chemical Society* 2014, 136, 978-985.

76. Kramm, U. I.; Herrmann-Geppert, I.; Behrends, J.; Lips, K.; Fiechter, S.; Bogdanoff, P. On an Easy Way To Prepare Metal–Nitrogen Doped Carbon with Exclusive Presence of MeN4-type Sites Active for the ORR. *Journal of the American Chemical Society* 2016, 138, 635-640.

77. Zhou, Y.; Neyerlin, K.; Olson, T. S.; Pylypenko, S.; Bult, J.; Dinh, H. N.; Gennett, T.; Shao, Z.; O'Hayre, R. Enhancement of Pt and Pt-alloy fuel cell catalyst activity and durability via nitrogen-modified carbon supports. *Energy & Environmental Science* 2010, 3, 1437-1446.

78. Choi, J. Y.; Hsu, R. S.; Chen, Z. W. Highly Active Porous Carbon-Supported Nonprecious Metal-N Electrocatalyst for Oxygen Reduction Reaction in PEM Fuel Cells. *J Phys Chem C* 2010, 114, 8048-8053.

79. Li, X.; Liu, G.; Popov, B. N. Activity and stability of non-precious metal catalysts for oxygen reduction in acid and alkaline electrolytes. *J Power Sources* 2010, 195, 6373-6378.

80. Liu, G.; Li, X.; Ganesan, P.; Popov, B. N. Studies of oxygen reduction reaction active sites and stability of nitrogen-modified carbon composite catalysts for PEM fuel cells. *Electrochim Acta* 2010, 55, 2853-2858.

81. Nallathambi, V.; Lee, J.-W.; Kumaraguru, S. P.; Wu, G.; Popov, B. N. Development of high performance carbon composite catalyst for oxygen reduction reaction in PEM Proton Exchange Membrane fuel cells. *J Power Sources* 2008, 183, 34-42.

82. Subramanian, N. P.; Kumaraguru, S. P.; Colon-Mercado, H.; Kim, H.; Popov, B. N.; Black, T.; Chen, D. A. Studies on Co-based catalysts supported on modified carbon substrates for PEMFC cathodes. *J Power Sources* 2006, 157, 56-63.

83. Popov, B. N.; Li, X.; Liu, G.; Lee, J.-W. Power source research at USC: Development of advanced electrocatalysts for polymer electrolyte membrane fuel cells. *Int J Hydrogen Energ* 2011, 36, 1794-1802.

84. Cote, R.; Lalande, G.; Faubert, G.; Guay, D.; Dodelet, J.; Denes, G. Non-noble metal-based catalysts for the reduction of oxygen in polymer electrolyte fuel cells. *Journal of new materials for electrochemical systems* 1998, 1, 7-16.

85. Faubert, G.; Cote, R.; Guay, D.; Dodelet, J.; Denes, G.; Bertrandc, P. Iron catalysts prepared by high-temperature pyrolysis of tetraphenylporphyrins adsorbed on carbon black for oxygen reduction in polymer electrolyte fuel cells. *Electrochim Acta* 1998, 43, 341-353.

86. Wang, X.; Lee, J. S.; Zhu, Q.; Liu, J.; Wang, Y.; Dai, S. Ammonia-treated ordered mesoporous carbons as catalytic materials for oxygen reduction reaction. *Chemistry of Materials* 2010, 22, 2178-2180.

87. Bron, M.; Fiechter, S.; Hilgendorff, M.; Bogdanoff, P. Catalysts for oxygen reduction from heat-treated carbon-supported iron phenantroline complexes. *Journal of applied electrochemistry* 2002, 32, 211-216.

88. Jaouen, F.; Marcotte, S.; Dodelet, J.-P.; Lindbergh, G. Oxygen reduction catalysts for polymer electrolyte fuel cells from the pyrolysis of iron acetate adsorbed on various carbon supports. *The Journal of Physical Chemistry B* 2003, 107, 1376-1386.

89. Lefevre, M.; Dodelet, J.; Bertrand, P. Molecular oxygen reduction in PEM fuel cell conditions: ToF-SIMS analysis of Co-based electrocatalysts. *The Journal of Physical Chemistry B* 2005, 109, 16718-16724.

90. Lef èvre, M.; Dodelet, J.-P. Fe-based catalysts for the reduction of oxygen in polymer electrolyte membrane fuel cell conditions: determination of the amount of peroxide released

during electroreduction and its influence on the stability of the catalysts. *Electrochimica Acta* 2003, 48, 2749-2760.

91. Medard, C.; Lefevre, M.; Dodelet, J.; Jaouen, F.; Lindbergh, G. Oxygen reduction by Fe-based catalysts in PEM fuel cell conditions: activity and selectivity of the catalysts obtained with two Fe precursors and various carbon supports. *Electrochim Acta* 2006, 51, 3202-3213.

92. Charreteur, F.; Jaouen, F.; Dodelet, J.-P. Iron porphyrin-based cathode catalysts for PEM fuel cells: Influence of pyrolysis gas on activity and stability. *Electrochim Acta* 2009, 54, 6622-6630.

93. Alves, M. M.; Dodelet, J.; Guay, D.; Ladouceur, M.; Tourillon, G. Origin of the electrocatalytic properties for oxygen reduction of some heat-treated polyacrylonitrile and phthalocyanine cobalt compounds adsorbed on carbon black as probed by electrochemistry and x-ray absorption spectroscopy. *The Journal of Physical Chemistry* 1992, 96, 10898-10905.

94. Bouwkamp-Wijnoltz, A.; Visscher, W.; Van Veen, J.; Tang, S. Electrochemical reduction of oxygen: an alternative method to prepare active CoN< sub> 4</sub> catalysts. *Electrochim Acta* 1999, 45, 379-386.

95. Chung, H. T.; Won, J. H.; Zelenay, P. Active and stable carbon nanotube/nanoparticle composite electrocatalyst for oxygen reduction. *Nature communications* 2013, 4, 1922.

96. Varnell, J. A.; Edmund, C.; Schulz, C. E.; Fister, T. T.; Haasch, R. T.; Timoshenko, J.; Frenkel, A. I.; Gewirth, A. A. Identification of carbon-encapsulated iron nanoparticles as active species in non-precious metal oxygen reduction catalysts. *Nature communications* 2016, 7.

97. Liang, H.-W.; Zhuang, X.; Brüller, S.; Feng, X.; Müllen, K. Hierarchically porous carbons with optimized nitrogen doping as highly active electrocatalysts for oxygen reduction. *Nature communications* 2014, 5.

98. Fu, X.; Zamani, P.; Choi, J.-Y.; Hassan, F. M.; Jiang, G.; Higgins, D. C.; Zhang, Y.; Hoque, M. A.; Chen, Z. In-Situ Polymer Graphenization Ingrained with Nanoporosity in

Nitrogenous Electrocatalyst Boosting the Performance of Polymer Electrolyte Membrane Fuel Cells. *Advanced Materials* 2017.

99. Wu, G.; More, K. L.; Xu, P.; Wang, H.-L.; Ferrandon, M.; Kropf, A. J.; Myers, D. J.; Ma, S.; Johnston, C. M.; Zelenay, P. A carbon-nanotube-supported graphene-rich non-precious metal oxygen reduction catalyst with enhanced performance durability. *Chemical Communications* 2013, 49, 3291-3293.

100. Liu, Y.; Wu, Y.-Y.; Lv, G.-J.; Pu, T.; He, X.-Q.; Cui, L.-L. Iron (II) phthalocyanine covalently functionalized graphene as a highly efficient non-precious-metal catalyst for the oxygen reduction reaction in alkaline media. *Electrochimica Acta* 2013, 112, 269-278.

101. Wen, Z.; Liu, J.; Li, J. Core/Shell Pt/C Nanoparticles Embedded in Mesoporous Carbon as a Methanol‐Tolerant Cathode Catalyst in Direct Methanol Fuel Cells. *Advanced Materials* 2008, 20, 743-747.

102. Joo, S. H.; Pak, C.; You, D. J.; Lee, S.-A.; Lee, H. I.; Kim, J. M.; Chang, H.; Seung, D. Ordered mesoporous carbons (OMC) as supports of electrocatalysts for direct methanol fuel cells (DMFC): effect of carbon precursors of OMC on DMFC performances. *Electrochim Acta* 2006, 52, 1618-1626.

103. Ambrosio, E. P.; Francia, C.; Manzoli, M.; Penazzi, N.; Spinelli, P. Platinum catalyst supported on mesoporous carbon for PEMFC. *Int J Hydrogen Energ* 2008, 33, 3142-3145.

104. Joo, J. B.; Kim, P.; Kim, W.; Kim, J.; Yi, J. Preparation of mesoporous carbon templated by silica particles for use as a catalyst support in polymer electrolyte membrane fuel cells. *Catalysis Today* 2006, 111, 171-175.

105. Chen, Z.; Higgins, D.; Tao, H.; Hsu, R. S.; Chen, Z. Highly Active Nitrogen-Doped Carbon Nanotubes for Oxygen Reduction Reaction in Fuel Cell Applications. *The Journal of Physical Chemistry C* 2009, 113, 21008-21013.

106. Higgins, D. C.; Meza, D.; Chen, Z. W. Nitrogen-Doped Carbon Nanotubes as Platinum Catalyst Supports for Oxygen Reduction Reaction in Proton Exchange Membrane Fuel Cells. *J Phys Chem C* 2010, 114, 21982-21988.

107. Li, W.; Liang, C.; Zhou, W.; Qiu, J.; Zhou; Sun, G.; Xin, Q. Preparation and Characterization of Multiwalled Carbon Nanotube-Supported Platinum for Cathode

Catalysts of Direct Methanol Fuel Cells. *The Journal of Physical Chemistry B* 2003, 107, 6292-6299.

108. Lin, Y.; Cui, X.; Yen, C.; Wai, C. M. Platinum/Carbon Nanotube Nanocomposite Synthesized in Supercritical Fluid as Electrocatalysts for Low-Temperature Fuel Cells. *The Journal of Physical Chemistry B* 2005, 109, 14410-14415.

109. Zhang, W.; Sherrell, P.; Minett, A. I.; Razal, J. M.; Chen, J. Carbon nanotube architectures as catalyst supports for proton exchange membrane fuel cells. *Energ Environ Sci* 2010, 3, 1286-1293.

110. Guo, J.; Sun, G.; Wang, Q.; Wang, G.; Zhou, Z.; Tang, S.; Jiang, L.; Zhou, B.; Xin, Q. Carbon nanofibers supported Pt–Ru electrocatalysts for direct methanol fuel cells. *Carbon* 2006, 44, 152-157.

111. Maldonado, S.; Stevenson, K. J. Influence of nitrogen doping on oxygen reduction electrocatalysis at carbon nanofiber electrodes. *The Journal of Physical Chemistry B* 2005, 109, 4707-4716.

112. Lee, K.; Zhang, J.; Wang, H.; Wilkinson, D. P. Progress in the synthesis of carbon nanotube-and nanofiber-supported Pt electrocatalysts for PEM fuel cell catalysis. *Journal of applied electrochemistry* 2006, 36, 507-522.

113. Byambasuren, U.; Jeon, Y.; Altansukh, D.; Shul, Y.-G. Doping effect of boron and phosphorus on nitrogen-based mesoporous carbons as electrocatalysts for oxygen reduction reaction in acid media. *Journal of Solid State Electrochemistry* 2016, 20, 645-655.

114. Ferrandon, M.; Kropf, A. J.; Myers, D. J.; Artyushkova, K.; Kramm, U.; Bogdanoff, P.; Wu, G.; Johnston, C. M.; Zelenay, P. Multitechnique characterization of a polyaniline–iron–carbon oxygen reduction catalyst. *The Journal of Physical Chemistry C* 2012, 116, 16001-16013.

115. Singh, K. P.; Bae, E. J.; Yu, J.-S. Fe–P: A New Class of Electroactive Catalyst for Oxygen Reduction Reaction. *Journal of the American Chemical Society* 2015, 137, 3165-3168.

116. Razmjooei, F.; Singh, K. P.; Bae, E. J.; Yu, J.-S. A new class of electroactive Fe-and P-functionalized graphene for oxygen reduction. *Journal of Materials Chemistry A* 2015, 3, 11031-11039.

117. Tian, J.; Morozan, A.; Sougrati, M. T.; Lefèvre, M.; Chenitz, R.; Dodelet, J. P.; Jones, D.; Jaouen, F. Optimized synthesis of Fe/N/C cathode catalysts for PEM fuel cells: a matter of iron–ligand coordination strength. *Angewandte Chemie* 2013, 125, 7005-7008.

118. Rauf, M.; Zhao, Y.-D.; Wang, Y.-C.; Zheng, Y.-P.; Chen, C.; Yang, X.-D.; Zhou, Z.-Y.; Sun, S.-G. Insight into the different ORR catalytic activity of Fe/N/C between acidic and alkaline media: Protonation of pyridinic nitrogen. *Electrochemistry Communications* 2016, 73, 71-74.

119. Marković, N.; Ross, P. N. Surface science studies of model fuel cell electrocatalysts. *Surface Science Reports* 2002, 45, 117-229.

120. Shao, M.; Chang, Q.; Dodelet, J.-P.; Chenitz, R. Recent advances in electrocatalysts for oxygen reduction reaction. *Chem. Rev* 2016, 116, 3594-3657.

121. Parvez, K.; Yang, S.; Hernandez, Y.; Winter, A.; Turchanin, A.; Feng, X.; Müllen, K. Nitrogen-doped graphene and its iron-based composite as efficient electrocatalysts for oxygen reduction reaction. *ACS nano* 2012, 6, 9541-9550.

122. Noh, S. H.; Seo, M. H.; Kang, J.; Okajima, T.; Han, B.; Ohsaka, T. Towards a comprehensive understanding of FeCo coated with N-doped carbon as a stable bi-functional catalyst in acidic media. *NPG Asia Materials* 2016, 8, e312.

123. Chung, H. T.; Cullen, D. A.; Higgins, D.; Sneed, B. T.; Holby, E. F.; More, K. L.; Zelenay, P. Direct atomic-level insight into the active sites of a high-performance PGM-free ORR catalyst. *Science* 2017, 357, 479-484.

124. Wang, Y.; Yuan, H.; Li, Y.; Chen, Z. Two-dimensional iron-phthalocyanine (Fe-Pc) monolayer as a promising single-atom-catalyst for oxygen reduction reaction: a computational study. *Nanoscale* 2015, 7, 11633-11641.

125. Randin, J. P. Interpretation of the relative electrochemical activity of various metal phthalocyanines for the oxygen reduction reaction. *Electrochimica Acta* 1974, 19, 83.

126. Zagal, J.; Bindra, P.; Yeager, E. A Mechanistic Study of O[sub 2] Reduction on Water Soluble Phthalocyanines Adsorbed on Graphite Electrodes. *Journal of The Electrochemical Society* 1980, 127, 1506-1517.

127. Zhang, J. *PEM Fuel Cell Electrocatalysts and Catalyst Layers*. Springer-Verlag: London, 2008.

128. Bezerra, C. W.; Zhang, L.; Lee, K.; Liu, H.; Marques, A. L.; Marques, E. P.; Wang, H.; Zhang, J. A review of Fe–N/C and Co–N/C catalysts for the oxygen reduction reaction. *Electrochimica Acta* 2008, 53, 4937-4951.

129. Zhang, J. *PEM fuel cell electrocatalysts and catalyst layers: fundamentals and applications*. Springer: 2008.

130. Beck, F. The redox mechanism of the chelate-catalysed oxygen cathode. *J. Appl. Electrochem.* 1977, 7, 239-245.

131. Yeager, E. Electrocatalysts for O< sub> 2</sub> reduction. *Electrochimica Acta* 1984, 29, 1527-1537.

132. Zheng, Y.; Jiao, Y.; Jaroniec, M.; Jin, Y.; Qiao, S. Z. Nanostructured Metal‐Free Electrochemical Catalysts for Highly Efficient Oxygen Reduction. *Small* 2012, 8, 3550-3566.

133. Yu, D.; Zhang, Q.; Dai, L. Highly efficient metal-free growth of nitrogen-doped single-walled carbon nanotubes on plasma-etched substrates for oxygen reduction. *Journal of the American Chemical Society* 2010, 132, 15127-15129.

134. Qu, L.; Liu, Y.; Baek, J.-B.; Dai, L. Nitrogen-doped graphene as efficient metal-free electrocatalyst for oxygen reduction in fuel cells. *Acs Nano* 2010, 4, 1321-1326.

135. Yang, S.; Feng, X.; Wang, X.; Müllen, K. Graphene‐Based Carbon Nitride Nanosheets as Efficient Metal‐Free Electrocatalysts for Oxygen Reduction Reactions. *Angewandte Chemie International Edition* 2011, 50, 5339-5343.

136. Sheng, Z.-H.; Shao, L.; Chen, J.-J.; Bao, W.-J.; Wang, F.-B.; Xia, X.-H. Catalyst-free synthesis of nitrogen-doped graphene via thermal annealing graphite oxide with melamine and its excellent electrocatalysis. *Acs Nano* 2011, 5, 4350-4358.

137. Zheng, Y.; Jiao, Y.; Chen, J.; Liu, J.; Liang, J.; Du, A.; Zhang, W.; Zhu, Z.; Smith, S. C.; Jaroniec, M. Nanoporous graphitic-C3N4@ carbon metal-free electrocatalysts for highly efficient oxygen reduction. *Journal of the American Chemical Society* 2011, 133, 20116-20119.

138. Yin, J.; Qiu, Y.; Yu, J. Porous nitrogen-doped carbon nanofibers as highly efficient metal-free electrocatalyst for oxygen reduction reaction. *J. Electroanal. Chem.* 2013, 702, 56-59.

139. Yin, J.; Qiu, Y.; Yu, J.; Zhou, X.; Wu, W. Enhancement of electrocatalytic activity for oxygen reduction reaction in alkaline and acid media from electrospun nitrogen-doped carbon nanofibers by surface modification. *RSC Advances* 2013, 3, 15655-15663.

140. Silva, R.; Voiry, D.; Chhowalla, M.; Asefa, T. Efficient metal-free electrocatalysts for oxygen reduction: polyaniline-derived N-and O-doped mesoporous carbons. *Journal of the American Chemical Society* 2013, 135, 7823-7826.

141. Meng, Y.; Voiry, D.; Goswami, A.; Zou, X.; Huang, X.; Chhowalla, M.; Liu, Z.; Asefa, T. N-, O-, and S-tridoped nanoporous carbons as selective catalysts for oxygen reduction and alcohol oxidation reactions. *Journal of the American Chemical Society* 2014, 136, 13554-13557.

142. Meng, Y.; Zou, X.; Huang, X.; Goswami, A.; Liu, Z.; Asefa, T. Polypyrrole‐Derived Nitrogen and Oxygen Co‐Doped Mesoporous Carbons as Efficient Metal‐Free Electrocatalyst for Hydrazine Oxidation. *Advanced Materials* 2014, 26, 6510-6516.

143. Zhang, S.; Miran, M. S.; Ikoma, A.; Dokko, K.; Watanabe, M. Protic ionic liquids and salts as versatile carbon precursors. *Journal of the American Chemical Society* 2014, 136, 1690-1693.

144. Yang, W.; Fellinger, T.-P.; Antonietti, M. Efficient metal-free oxygen reduction in alkaline medium on high-surface-area mesoporous nitrogen-doped carbons made from ionic liquids and nucleobases. *Journal of the American Chemical Society* 2010, 133, 206-209.

145. Nagaiah, T. C.; Bordoloi, A.; Sánchez, M. D.; Muhler, M.; Schuhmann, W. Mesoporous Nitrogen‐Rich Carbon Materials as Catalysts for the Oxygen Reduction Reaction in Alkaline Solution. *ChemSusChem* 2012, 5, 637-641.

146. Liang, H.-W.; Wu, Z.-Y.; Chen, L.-F.; Li, C.; Yu, S.-H. Bacterial cellulose derived nitrogen-doped carbon nanofiber aerogel: An efficient metal-free oxygen reduction electrocatalyst for zinc-air battery. *Nano Energy* 2014.

147. Li, Y.; Samad, Y.; Polychronopoulou, K.; Alhassan, S. M.; Liao, K. Carbon Aerogel from Winter Melon for Highly Efficient and Recyclable Oils and Organic Solvents Absorption. *ACS Sustainable Chemistry & Engineering* 2014.

148. Yang, Z.; Yao, Z.; Li, G.; Fang, G.; Nie, H.; Liu, Z.; Zhou, X.; Chen, X. a.; Huang, S. Sulfur-doped graphene as an efficient metal-free cathode catalyst for oxygen reduction. *ACS nano* 2011, 6, 205-211.

149. Yang, L.; Jiang, S.; Zhao, Y.; Zhu, L.; Chen, S.; Wang, X.; Wu, Q.; Ma, J.; Ma, Y.; Hu, Z. Boron‐Doped Carbon Nanotubes as Metal‐Free Electrocatalysts for the Oxygen Reduction Reaction. *Angewandte Chemie* 2011, 123, 7270-7273.

150. Yang, D.-S.; Bhattacharjya, D.; Inamdar, S.; Park, J.; Yu, J.-S. Phosphorus-doped ordered mesoporous carbons with different lengths as efficient metal-free electrocatalysts for oxygen reduction reaction in alkaline media. *Journal of the American Chemical Society* 2012, 134, 16127-16130.

151. Yao, Z.; Nie, H.; Yang, Z.; Zhou, X.; Liu, Z.; Huang, S. Catalyst-free synthesis of iodine-doped graphene via a facile thermal annealing process and its use for electrocatalytic oxygen reduction in an alkaline medium. *Chemical Communications* 2012, 48, 1027-1029.

152. Panchakarla, L.; Subrahmanyam, K.; Saha, S.; Govindaraj, A.; Krishnamurthy, H.; Waghmare, U.; Rao, C. Synthesis, structure, and properties of boron-and nitrogen-doped graphene. *Advanced Materials* 2009, 21, 4726-4730.

153. Zhao, Y.; Yang, L.; Chen, S.; Wang, X.; Ma, Y.; Wu, Q.; Jiang, Y.; Qian, W.; Hu, Z. Can boron and nitrogen co-doping improve oxygen reduction reaction activity of carbon nanotubes? *Journal of the American Chemical Society* 2013, 135, 1201-1204.

154. Jin, Z.; Nie, H.; Yang, Z.; Zhang, J.; Liu, Z.; Xu, X.; Huang, S. Metal-free selenium doped carbon nanotube/graphene networks as a synergistically improved cathode catalyst for oxygen reduction reaction. *Nanoscale* 2012, 4, 6455-6460.

155. Kong, X.-K.; Chen, C.-L.; Chen, Q.-W. Doped graphene for metal-free catalysis. *Chemical Society Reviews* 2014, 43, 2841-2857.

156. Wang, D.-W.; Su, D. Heterogeneous nanocarbon materials for oxygen reduction reaction. *Energy & Environmental Science* 2014, 7, 576-591.

157. Choi, C. H.; Chung, M. W.; Kwon, H. C.; Park, S. H.; Woo, S. I. B, N-and P, N-doped graphene as highly active catalysts for oxygen reduction reactions in acidic media. *Journal of Materials Chemistry A* 2013, 1, 3694-3699.

158. Chen, S.; Bi, J.; Zhao, Y.; Yang, L.; Zhang, C.; Ma, Y.; Wu, Q.; Wang, X.; Hu, Z. Nitrogen‐Doped Carbon Nanocages as Efficient Metal‐Free Electrocatalysts for Oxygen Reduction Reaction. *Advanced Materials* 2012, 24, 5593-5597.

159. Yang, S.; Zhi, L.; Tang, K.; Feng, X.; Maier, J.; Müllen, K. Efficient Synthesis of Heteroatom (N or S)‐Doped Graphene Based on Ultrathin Graphene Oxide‐Porous Silica Sheets for Oxygen Reduction Reactions. *Advanced Functional Materials* 2012, 22, 3634-3640.

160. Liang, J.; Jiao, Y.; Jaroniec, M.; Qiao, S. Z. Sulfur and nitrogen dual‐doped mesoporous graphene electrocatalyst for oxygen reduction with synergistically enhanced performance. *Angewandte Chemie International Edition* 2012, 51, 11496-11500.

161. Xu, J.; Dong, G.; Jin, C.; Huang, M.; Guan, L. Sulfur and Nitrogen Co‐Doped, Few‐Layered Graphene Oxide as a Highly Efficient Electrocatalyst for the Oxygen‐Reduction Reaction. *ChemSusChem* 2013, 6, 493-499.

162. Choi, C. H.; Park, S. H.; Woo, S. I. Binary and ternary doping of nitrogen, boron, and phosphorus into carbon for enhancing electrochemical oxygen reduction activity. *Acs Nano* 2012, 6, 7084-7091.

163. Liang, J.; Du, X.; Gibson, C.; Du, X. W.; Qiao, S. Z. N‐Doped Graphene Natively Grown on Hierarchical Ordered Porous Carbon for Enhanced Oxygen Reduction. *Advanced Materials* 2013, 25, 6226-6231.

164. He, W.; Jiang, C.; Wang, J.; Lu, L. High‐Rate Oxygen Electroreduction over Graphitic‐N Species Exposed on 3D Hierarchically Porous Nitrogen‐Doped Carbons. *Angewandte Chemie International Edition* 2014, 53, 9503-9507.

165. Chen, S.; Liu, Q.; He, G.; Zhou, Y.; Hanif, M.; Peng, X.; Wang, S.; Hou, H. Reticulated carbon foam derived from a sponge-like natural product as a high-performance anode in microbial fuel cells. *J. Mater. Chem.* 2012, 22, 18609-18613.

166. Li, Z.; Zhang, L.; Amirkhiz, B. S.; Tan, X.; Xu, Z.; Wang, H.; Olsen, B. C.; Holt, C.; Mitlin, D. Carbonized Chicken Eggshell Membranes with 3D Architectures as High‐Performance Electrode Materials for Supercapacitors. *Adv. Energy Mater.* 2012, 2, 431-437.

167. Bhaumik, A.; Wu, K. C.-W. Hierarchically Porous Carbon Derived from Polymers and Biomass: Effect of Interconnected Pores on Energy Applications. *Energy & Environmental Science* 2014.

168. Shui, J.; Wang, M.; Du, F.; Dai, L. N-doped carbon nanomaterials are durable catalysts for oxygen reduction reaction in acidic fuel cells. *Science advances* 2015, 1, e1400129.

169. Kwon, K.; Sa, Y. J.; Cheon, J. Y.; Joo, S. H. Ordered mesoporous carbon nitrides with graphitic frameworks as metal-free, highly durable, methanol-tolerant oxygen reduction catalysts in an acidic medium. *Langmuir* 2011, 28, 991-996.

170. Rao, C. V.; Cabrera, C. R.; Ishikawa, Y. In search of the active site in nitrogen-doped carbon nanotube electrodes for the oxygen reduction reaction. *The journal of physical chemistry letters* 2010, 1, 2622-2627.

171. Wang, L.; Ambrosi, A.; Pumera, M. "Metal‐Free" Catalytic Oxygen Reduction Reaction on Heteroatom‐Doped Graphene is Caused by Trace Metal Impurities. *Angewandte Chemie International Edition* 2013, 52, 13818-13821.

172. Wang, L.; Wong, C. H. A.; Kherzi, B.; Webster, R. D.; Pumera, M. So‐Called "Metal‐Free" Oxygen Reduction at Graphene Nanoribbons is in fact Metal Driven. *ChemCatChem* 2015, 7, 1650-1654.

173. Masa, J.; Zhao, A.; Xia, W.; Sun, Z.; Mei, B.; Muhler, M.; Schuhmann, W. Trace metal residues promote the activity of supposedly metal-free nitrogen-modified carbon catalysts for the oxygen reduction reaction. *Electrochem. Commun.* 2013, 34, 113-116.

174. Béguin, F.; Frackowiak, E. *Carbons for electrochemical energy storage and conversion systems*. CRC Press: 2009.

175. Wu, K. H.; Wang, D. W.; Su, D. S.; Gentle, I. R. A Discussion on the Activity Origin in Metal‐Free Nitrogen‐Doped Carbons For Oxygen Reduction Reaction and their Mechanisms. *ChemSusChem* 2015, 8, 2772-2788.

176. Young, R. J.; Lovell, P. A. *Introduction to polymers*. CRC press: 2011.

177. Rezaaiyaan, R.; Hieftje, G.; Anderson, H.; Kaiser, H.; Meddings, B. Design and construction of a low-flow, low-power torch for inductively coupled plasma spectrometry. *Applied Spectroscopy* 1982, 36, 627-631.

178. Fassel, V. A. Quantitative elemental analyses by plasma emission spectroscopy. *Science* 1978, 202, 183-191.

179. Barnard, T. W.; Crockett, M. I.; Ivaldi, J. C.; Lundberg, P. L.; Yates, D. A.; Levine, P. A.; Sauer, D. J. Solid-state detector for ICP-OES. *Analytical chemistry* 1993, 65, 1231-1239.

180. Wu, G.; Johnston, C. M.; Mack, N. H.; Artyushkova, K.; Ferrandon, M.; Nelson, M.; Lezama-Pacheco, J. S.; Conradson, S. D.; More, K. L.; Myers, D. J. Synthesis–structure–performance correlation for polyaniline–Me–C non-precious metal cathode catalysts for oxygen reduction in fuel cells. *Journal of Materials Chemistry* 2011, 21, 11392-11405.

181. Fadley, C.; Davison, S. Progress in Surface Science. *Vol. 16Pergamon, New York* 1984, 275.

182. Fadley, C.; Baird, R.; Siekhaus, W.; Novakov, T.; Bergström, S. Surface analysis and angular distributions in x-ray photoelectron spectroscopy. *Journal of Electron Spectroscopy and Related Phenomena* 1974, 4, 93-137.

183. Turner, D. W.; Jobory, M. A. Determination of ionization potentials by photoelectron energy measurement. *The Journal of Chemical Physics* 1962, 37, 3007-3008.

184. Chastain, J.; King, R. C.; Moulder, J. *Handbook of X-ray photoelectron spectroscopy: a reference book of standard spectra for identification and interpretation of XPS data*. Physical Electronics Eden Prairie, MN: 1995.

185. Seiler, H. Secondary electron emission in the scanning electron microscope. *J Appl Phys* 1983, 54, R1-R18.

186. Williams, D. B.; Carter, C. B. *The Transmission Electron Microscope*. Springer: 1996.

187. Williams, D. B.; Carter, C. B. The transmission electron microscope. In *Transmission Electron Microscopy*, Springer: 2009; pp 3-22.

188. Fultz, B.; Howe, J. M. *Transmission electron microscopy and diffractometry of materials*. Springer Science & Business Media: 2012.

189. Goldstein, J.; Newbury, D. E.; Echlin, P.; Joy, D. C.; Romig Jr, A. D.; Lyman, C. E.; Fiori, C.; Lifshin, E. *Scanning electron microscopy and X-ray microanalysis: a text for biologists, materials scientists, and geologists*. Springer Science & Business Media: 2012.

190. Niu, Z.; Becknell, N.; Yu, Y.; Kim, D.; Chen, C.; Kornienko, N.; Somorjai, G. A.; Yang, P. Anisotropic phase segregation and migration of Pt in nanocrystals en route to nanoframe catalysts. *Nature materials* 2016.

191. Brunauer, S.; Emmett, P. H.; Teller, E. Adsorption of gases in multimolecular layers. *Journal of the American Chemical Society* 1938, 60, 309-319.

192. Sing, K. S. Reporting physisorption data for gas/solid systems with special reference to the determination of surface area and porosity (Recommendations 1984). *Pure and applied chemistry* 1985, 57, 603-619.

193. Landers, J.; Gor, G. Y.; Neimark, A. V. Density functional theory methods for characterization of porous materials. *Colloids and Surfaces A: Physicochemical and Engineering Aspects* 2013, 437, 3-32.

194. Warren, B. E. *X-ray Diffraction*. Courier Dover Publications: 1969.

195. Jiang, G.; Goledzinowski, M.; Comeau, F. J.; Zarrin, H.; Lui, G.; Lenos, J.; Veileux, A.; Liu, G.; Zhang, J.; Hemmati, S. Free‐Standing Functionalized Graphene Oxide Solid Electrolytes in Electrochemical Gas Sensors. *Advanced Functional Materials* 2016.

196. Hassan, F. M.; Chabot, V.; Li, J.; Kim, B. K.; Ricardez-Sandoval, L.; Yu, A. Pyrrolic-structure enriched nitrogen doped graphene for highly efficient next generation supercapacitors. *Journal of Materials Chemistry A* 2013, 1, 2904-2912.

197. Hong, W. T.; Risch, M.; Stoerzinger, K. A.; Grimaud, A.; Suntivich, J.; Shao-Horn, Y. Toward the rational design of non-precious transition metal oxides for oxygen electrocatalysis. *Energy & Environmental Science* 2015, 8, 1404-1427.

198. Xia, W.; Mahmood, A.; Liang, Z.; Zou, R.; Guo, S. Earth‐Abundant Nanomaterials for Oxygen Reduction. *Angewandte Chemie International Edition* 2016, 55, 2650-2676.

199. Yu, A.; Park, H. W.; Davies, A.; Higgins, D. C.; Chen, Z.; Xiao, X. Free-standing layer-by-layer hybrid thin film of graphene-MnO2 nanotube as anode for lithium ion batteries. *The Journal of Physical Chemistry Letters* 2011, 2, 1855-1860.

200. Zamani, P.; Higgins, D.; Hassan, F.; Jiang, G.; Wu, J.; Abureden, S.; Chen, Z. Electrospun iron–polyaniline–polyacrylonitrile derived nanofibers as non–precious oxygen reduction reaction catalysts for PEM fuel cells. *Electrochimica Acta* 2014, 139, 111-116.

201. Song, C.; Zhang, J. Electrocatalytic oxygen reduction reaction. In *PEM fuel cell electrocatalysts and catalyst layers*, Springer: 2008; pp 89-134.

202. Chiwata, M.; Kakinuma, K.; Wakisaka, M.; Uchida, M.; Deki, S.; Watanabe, M.; Uchida, H. Oxygen reduction reaction activity and durability of Pt catalysts supported on titanium carbide. *Catalysts* 2015, 5, 966-980.

203. Banham, D.; Feng, F.; Pei, K.; Ye, S.; Birss, V. Effect of carbon support nanostructure on the oxygen reduction activity of Pt/C catalysts. *Journal of Materials Chemistry A* 2013, 1, 2812-2820.

204. Paulus, U.; Schmidt, T.; Gasteiger, H.; Behm, R. Oxygen reduction on a high-surface area Pt/Vulcan carbon catalyst: a thin-film rotating ring-disk electrode study. *Journal of Electroanalytical Chemistry* 2001, 495, 134-145.

205. Chen, Z.; Yu, A. P.; Higgins, D.; Li, H.; Wang, H. J.; Chen, Z. W. Highly Active and Durable Core-Corona Structured Bifunctional Catalyst for Rechargeable Metal-Air Battery Application. *Nano Letters* 2012, 12, 1946-1952.

206. Weidner, J. W.; Sethuraman, V. A.; Van Zee, J. W. Membrane Electrode Assembly. *Electrochemical Society Interface* 2003, 41-47.

207. Schlögl, R. The role of chemistry in the energy challenge. *ChemSusChem* 2010, 3, 209-222.

208. Yang, H. B.; Miao, J.; Hung, S.-F.; Chen, J.; Tao, H. B.; Wang, X.; Zhang, L.; Chen, R.; Gao, J.; Chen, H. M. Identification of catalytic sites for oxygen reduction and oxygen evolution in N-doped graphene materials: Development of highly efficient metal-free bifunctional electrocatalyst. *Science advances* 2016, 2, e1501122.

209. Lee, D. U.; Xu, P.; Cano, Z. P.; Kashkooli, A. G.; Park, M. G.; Chen, Z. Recent progress and perspectives on bi-functional oxygen electrocatalysts for advanced rechargeable metal–air batteries. *Journal of Materials Chemistry A* 2016, 4, 7107-7134.

210. Lee, D. U.; Choi, J. Y.; Feng, K.; Park, H. W.; Chen, Z. Advanced Extremely Durable 3D Bifunctional Air Electrodes for Rechargeable Zinc‐Air Batteries. *Advanced Energy Materials* 2014, 4.

211. Park, H. W.; Lee, D. U.; Park, M. G.; Ahmed, R.; Seo, M. H.; Nazar, L. F.; Chen, Z. Perovskite–Nitrogen‐Doped Carbon Nanotube Composite as Bifunctional Catalysts for Rechargeable Lithium–Air Batteries. *ChemSusChem* 2015, 8, 1058-1065.

212. Wu, G.; Mack, N. H.; Gao, W.; Ma, S.; Zhong, R.; Han, J.; Baldwin, J. K.; Zelenay, P. Nitrogen-doped graphene-rich catalysts derived from heteroatom polymers for oxygen reduction in nonaqueous lithium–O2 battery cathodes. *ACS nano* 2012, 6, 9764-9776.

213. Lee, D. U.; Li, J.; Park, M. G.; Seo, M. H.; Ahn, W.; Stadelmann, I.; Ricardez-Sandoval, L.; Chen, Z. Self‐assembly of Spinel Nano‐crystals into Mesoporous Spheres as Bi‐functionally Active Oxygen Reduction and Evolution Electrocatalysts. *ChemSusChem* 2017.

214. Higgins, D.; Hoque, M. A.; Seo, M. H.; Wang, R.; Hassan, F.; Choi, J. Y.; Pritzker, M.; Yu, A.; Zhang, J.; Chen, Z. Development and Simulation of Sulfur‐doped Graphene Supported Platinum with Exemplary Stability and Activity Towards Oxygen Reduction. *Advanced Functional Materials* 2014, 24, 4325-4336.

215. Hoque, M. A.; Hassan, F. M.; Higgins, D.; Choi, J. Y.; Pritzker, M.; Knights, S.; Ye, S.; Chen, Z. Multigrain Platinum Nanowires Consisting of Oriented Nanoparticles Anchored on Sulfur‐Doped Graphene as a Highly Active and Durable Oxygen Reduction Electrocatalyst. *Advanced Materials* 2015, 27, 1229-1234.

216. Hoque, M. A.; Hassan, F. M.; Seo, M.-H.; Choi, J.-Y.; Pritzker, M.; Knights, S.; Ye, S.; Chen, Z. Optimization of sulfur-doped graphene as an emerging platinum nanowires support for oxygen reduction reaction. *Nano Energy* 2016, 19, 27-38.

217. Chung, H.; Wu, G.; Higgins, D.; Zamani, P.; Chen, Z.; Zelenay, P. Heat-Treated Non-precious Metal Catalysts for Oxygen Reduction. In *Electrochemistry of N4 Macrocyclic Metal Complexes*, Springer: 2016; pp 41-68.

218. Jasinski, R. Cobalt phthalocyanine as a fuel cell cathode. *Journal of The Electrochemical Society* 1965, 112, 526-528.

219. Zhang, J.; Zhao, Z.; Xia, Z.; Dai, L. A metal-free bifunctional electrocatalyst for oxygen reduction and oxygen evolution reactions. *Nature nanotechnology* 2015, 10, 444-452.

220. Wang, S.; Zhang, L.; Xia, Z.; Roy, A.; Chang, D. W.; Baek, J. B.; Dai, L. BCN graphene as efficient metal‐free electrocatalyst for the oxygen reduction reaction. *Angewandte Chemie International Edition* 2012, 51, 4209-4212.

221. Li, W.; Yu, A.; Higgins, D. C.; Llanos, B. G.; Chen, Z. Biologically inspired highly durable iron phthalocyanine catalysts for oxygen reduction reaction in polymer electrolyte membrane fuel cells. *Journal of the American Chemical Society* 2010, 132, 17056-17058.

222. Tang, J.; Berry, R. M.; Tam, K. C. Stimuli-Responsive Cellulose Nanocrystals for Surfactant-Free Oil Harvesting. *Biomacromolecules* 2016, 17, 1748-1756.

223. Song, J.; Song, H.; Kong, H.; Hong, J.-Y.; Jang, J. Fabrication of silica/polyrhodanine core/shell nanoparticles and their antibacterial properties. *Journal of Materials Chemistry* 2011, 21, 19317-19323.

224. Ozkan, S.; Unal, H. I.; Yılmaz, E.; Suludere, Z. Electrokinetic and antibacterial properties of needle like‐TiO2/polyrhodanine core/shell hybrid nanostructures. *Journal of Applied Polymer Science* 2015, 132.

225. Pang, Q.; Tang, J.; Huang, H.; Liang, X.; Hart, C.; Tam, K. C.; Nazar, L. F. A Nitrogen and Sulfur Dual‐Doped Carbon Derived from Polyrhodanine@ Cellulose for Advanced Lithium–Sulfur Batteries. *Advanced Materials* 2015, 27, 6021-6028.

226. Liu, H.; Shi, Z.; Zhang, J.; Zhang, L.; Zhang, J. Ultrasonic spray pyrolyzed iron-polypyrrole mesoporous spheres for fuel celloxygen reduction electrocatalysts. *Journal of Materials Chemistry* 2009, 19, 468-470.

227. Jaouen, F.; Dodelet, J.-P. Average turn-over frequency of O 2 electro-reduction for Fe/N/C and Co/N/C catalysts in PEFCs. *Electrochimica Acta* 2007, 52, 5975-5984.

228. Yap, C.-P.; Liu, C. The free energy, entropy and heat of formation of iron carbide (Fe 3 C). *Transactions of the Faraday Society* 1932, 28, 788-797.

229. Zhang, G.; Chenitz, R.; Lefèvre, M.; Sun, S.; Dodelet, J.-P. Is iron involved in the lack of stability of Fe/N/C electrocatalysts used to reduce oxygen at the cathode of PEM fuel cells? *Nano Energy* 2016.

230. Baranton, S.; Coutanceau, C.; Roux, C.; Hahn, F.; Léger, J.-M. Oxygen reduction reaction in acid medium at iron phthalocyanine dispersed on high surface area carbon substrate: tolerance to methanol, stability and kinetics. *Journal of Electroanalytical Chemistry* 2005, 577, 223-234.

231. Seo, M. H.; Higgins, D.; Jiang, G.; Choi, S. M.; Han, B.; Chen, Z. Theoretical insight into highly durable iron phthalocyanine derived non-precious catalysts for oxygen reduction reactions. *Journal of Materials Chemistry A* 2014, 2, 19707-19716.

232. Jasinski, R. A New Fuel Cell Cathode Catalyst. *Nature* 1964, 201, 1212.

233. Cheng, N.; Banis, M. N.; Liu, J.; Riese, A.; Li, X.; Li, R.; Ye, S.; Knights, S.; Sun, X. Extremely Stable Platinum Nanoparticles Encapsulated in a Zirconia Nanocage by Area-Selective Atomic Layer Deposition for the Oxygen Reduction Reaction. *Adv. Mater.* 2015, 27, 277.

234. Higgins, D.; Hoque, M. A.; Seo, M. H.; Wang, R.; Hassan, F.; Choi, J. Y.; Pritzker, M.; Yu, A.; Zhang, J.; Chen, Z. Development and Simulation of Sulfur-doped Graphene Supported Platinum with Exemplary Stability and Activity Towards Oxygen Reduction. *Adv. Funct. Mater.* 2014, 24, 4325.

235. Xia, B. Y.; Wu, H. B.; Li, N.; Yan, Y.; Lou, X. W.; Wang, X. One-Pot Synthesis of Pt–Co Alloy Nanowire Assemblies with Tunable Composition and Enhanced Electrocatalytic Properties. *Angew. Chem., Int. Ed.* 2015, 54, 3797.

236. Fu, X.; Jin, J.; Liu, Y.; Wei, Z.; Pan, F.; Zhang, J. Efficient Oxygen Reduction Electrocatalyst Based on Edge-Nitrogen-Rich Graphene Nanoplatelets: Toward a Large-Scale Synthesis. *ACS Appl. Mater. Interfaces* 2014, 6, 3930.

237. Li, W.; Yu, A.; Higgins, D. C.; Llanos, B. G.; Chen, Z. Biologically Inspired Highly Durable Iron Phthalocyanine Catalysts for Oxygen Reduction Reaction in Polymer Electrolyte Membrane Fuel Cells. *J. Am. Chem. Soc.* 2010, 132, 17056.

238. Serov, A.; Robson, M. H.; Halevi, B.; Artyushkova, K.; Atanassov, P. Highly Active and Durable Templated Non-PGM Cathode Catalysts Derived From Iron and Aminoantipyrine. *Electrochem. Commun.* 2012, 22, 53.

239. Su, D. S.; Sun, G. Nonprecious-Metal Catalysts for Low-Cost Fuel Cells. *Angew. Chem., Int. Ed.* 2011, 50, 11570.

240. Wu, G.; Zelenay, P. Nanostructured Nonprecious Metal Catalysts for Oxygen Reduction Reaction. *Acc. Chem. Res.* 2013, 46, 1878.

241. Lefevre, M.; Dodelet, J.; Bertrand, P. O2 reduction in PEM fuel cells: activity and active site structural information for catalysts obtained by the pyrolysis at high temperature of Fe precursors. *The Journal of Physical Chemistry B* 2000, 104, 11238-11247.

242. Wang, H.; Cote, R.; Faubert, G.; Guay, D.; Dodelet, J. Effect of the pre-treatment of carbon black supports on the activity of Fe-based electrocatalysts for the reduction of oxygen. *The Journal of Physical Chemistry B* 1999, 103, 2042-2049.

243. Zarrin, H.; Jiang, G.; Lam, G. Y.-Y.; Fowler, M.; Chen, Z. High performance porous polybenzimidazole membrane for alkaline fuel cells. *International Journal of Hydrogen Energy* 2014.

244. Zhang, W.; Sun, W.-H.; Zhang, S.; Hou, J.; Wedeking, K.; Schultz, S.; Fröhlich, R.; Song, H. Synthesis, characterization, and ethylene oligomerization and polymerization of [2, 6-bis (2-benzimidazolyl) pyridyl] chromium chlorides. *Organometallics* 2006, 25, 1961-1969.

245. Fujigaya, T.; Uchinoumi, T.; Kaneko, K.; Nakashima, N. Design and synthesis of nitrogen-containing calcined polymer/carbon nanotube hybrids that act as a platinum-free oxygen reduction fuel cell catalyst. *Chemical Communications* 2011, 47, 6843-6845.

246. Xu, P.; Chen, W.; Wang, Q.; Zhu, T.; Wu, M.; Qiao, J.; Chen, Z.; Zhang, J. Effects of transition metal precursors (Co, Fe, Cu, Mn, or Ni) on pyrolyzed carbon supported metal-aminopyrine electrocatalysts for oxygen reduction reaction. *RSC Advances* 2015, 5, 6195-6206.

247. Balan, B. K.; Manissery, A. P.; Chaudhari, H. D.; Kharul, U. K.; Kurungot, S. Polybenzimidazole mediated N-doping along the inner and outer surfaces of a carbon nanofiber and its oxygen reduction properties. *J. Mater. Chem.* 2012, 22, 23668-23679.

248. Horváth, I. T. *Encyclopedia of catalysis*. Wiley-interscience: 2003.

249. Lu, J.; Bo, X.; Wang, H.; Guo, L. Nitrogen-doped ordered mesoporous carbons synthesized from honey as metal-free catalyst for oxygen reduction reaction. *Electrochimica Acta* 2013, 108, 10-16.

250. Duan, X.; Ao, Z.; Sun, H.; Indrawirawan, S.; Wang, Y.; Kang, J.; Liang, F.; Zhu, Z. H.; Wang, S. Nitrogen-doped graphene for generation and evolution of reactive radicals by metal-free catalysis. *ACS applied materials & interfaces* 2015, 7, 4169-4178.

251. Kong, X.-k.; Sun, Z.-y.; Chen, M.; Chen, Q.-w. Metal-free catalytic reduction of 4-nitrophenol to 4-aminophenol by N-doped graphene. *Energy & Environmental Science* 2013, 6, 3260-3266.

252. Xue, Y.; Yu, D.; Dai, L.; Wang, R.; Li, D.; Roy, A.; Lu, F.; Chen, H.; Liu, Y.; Qu, J. Three-dimensional B, N-doped graphene foam as a metal-free catalyst for oxygen reduction reaction. *Physical Chemistry Chemical Physics* 2013, 15, 12220-12226.

253. Chen, P.; Wang, L.-K.; Wang, G.; Gao, M.-R.; Ge, J.; Yuan, W.-J.; Shen, Y.-H.; Xie, A.-J.; Yu, S.-H. Nitrogen-doped nanoporous carbon nanosheets derived from plant biomass: an efficient catalyst for oxygen reduction reaction. *Energy & Environmental Science* 2014, 7, 4095-4103.

254. Wong, W.; Daud, W. R. W.; Mohamad, A. B.; Kadhum, A. A. H.; Loh, K. S.; Majlan, E. Recent progress in nitrogen-doped carbon and its composites as electrocatalysts for fuel cell applications. *International Journal of Hydrogen Energy* 2013, 38, 9370-9386.

255. Paraknowitsch, J. P.; Thomas, A. Doping carbons beyond nitrogen: an overview of advanced heteroatom doped carbons with boron, sulphur and phosphorus for energy applications. *Energy & Environmental Science* 2013, 6, 2839-2855.

256. Mo, Z.; Liao, S.; Zheng, Y.; Fu, Z. Preparation of nitrogen-doped carbon nanotube arrays and their catalysis towards cathodic oxygen reduction in acidic and alkaline media. *Carbon* 2012, 50, 2620-2627.

257. Vikkisk, M.; Kruusenberg, I.; Joost, U.; Shulga, E.; Tammeveski, K. Electrocatalysis of oxygen reduction on nitrogen-containing multi-walled carbon nanotube modified glassy carbon electrodes. *Electrochimica Acta* 2013, 87, 709-716.

258. Liu, D.; Zhang, X.; Sun, Z.; You, T. Free-standing nitrogen-doped carbon nanofiber films as highly efficient electrocatalysts for oxygen reduction. *Nanoscale* 2013, 5, 9528-9531.

259. Pan, F.; Cao, Z.; Zhao, Q.; Liang, H.; Zhang, J. Nitrogen-doped porous carbon nanosheets made from biomass as highly active electrocatalyst for oxygen reduction reaction. *Journal of Power Sources* 2014, 272, 8-15.

260. Zhou, X.; Bai, Z.; Wu, M.; Qiao, J.; Chen, Z. 3-Dimensional porous N-doped graphene foam as a non-precious catalyst for the oxygen reduction reaction. *Journal of Materials Chemistry A* 2015, 3, 3343-3350.

261. Higgins, D. C.; Hoque, M. A.; Hassan, F.; Choi, J.-Y.; Kim, B.; Chen, Z. Oxygen reduction on graphene–carbon nanotube composites doped sequentially with nitrogen and sulfur. *Acs Catalysis* 2014, 4, 2734-2740.

262. Geng, D.; Chen, Y.; Chen, Y.; Li, Y.; Li, R.; Sun, X.; Ye, S.; Knights, S. High oxygen-reduction activity and durability of nitrogen-doped graphene. *Energy & Environmental Science* 2011, 4, 760-764.

263. Fuertes, A.; Ferrero, G.; Sevilla, M. One-pot synthesis of microporous carbons highly enriched in nitrogen and their electrochemical performance. *Journal of Materials Chemistry A* 2014, 2, 14439-14448.

264. Lota, G.; Lota, K.; Frackowiak, E. Nanotubes based composites rich in nitrogen for supercapacitor application. *Electrochemistry Communications* 2007, 9, 1828-1832.

265. Zhu, C.; Li, H.; Fu, S.; Du, D.; Lin, Y. Highly efficient nonprecious metal catalysts towards oxygen reduction reaction based on three-dimensional porous carbon nanostructures. *Chemical Society Reviews* 2016, 45, 517-531.

266. Peng, B. L.; Dhar, N.; Liu, H.; Tam, K. Chemistry and applications of nanocrystalline cellulose and its derivatives: a nanotechnology perspective. *The Canadian Journal of Chemical Engineering* 2011, 89, 1191-1206.

267. Liang, H.-W.; Wu, Z.-Y.; Chen, L.-F.; Li, C.; Yu, S.-H. Bacterial cellulose derived nitrogen-doped carbon nanofiber aerogel: An efficient metal-free oxygen reduction electrocatalyst for zinc-air battery. *Nano Energy* 2015, 11, 366-376.

268. Zhu, S.; Chen, Z.; Li, B.; Higgins, D.; Wang, H.; Li, H.; Chen, Z. Nitrogen-doped carbon nanotubes as air cathode catalysts in zinc-air battery. *Electrochimica Acta* 2011, 56, 5080-5084.

269. Nam, G.; Park, J.; Kim, S. T.; Shin, D.-b.; Park, N.; Kim, Y.; Lee, J.-S.; Cho, J. Metal-free Ketjenblack incorporated nitrogen-doped carbon sheets derived from gelatin as oxygen reduction catalysts. *Nano letters* 2014, 14, 1870-1876.